University of Bologna "Alma Mater Studiorum" and University of Naples "Federico II"

Ph.D Thesis in Geophysics

XXV Cycle

04/A4 - GEO/10

Year 2013

Inferences on earthquake kinematic properties from data inversion: two different approaches

Ph.D. Thesis: ***Eugenio Maria Toraldo Serra***

Coordinator

Prof. Michele Dragoni

Tutor

Dr. Antonio Emolo

Contents

Index of Figures

Index of Tables

Acknowledgments

This work would not have been possible without the help and encouragement of many people and I would like to take this opportunity to express my thanks to them.
I thank all the professors, researchers, post-docs and graduate students who work with me in our laboratory and with whose help during these three years of PhD I grew both as a researcher and more importantly as a person.
In particular, however, I want to thank my tutor Antonio Emolo, who has proved to be an excellent teacher and friend: indeed he is without doubt the person who most followed, encouraged and criticized me during this period and without whom I would not have been able to complete my PhD.
I want to say a big thank you also to professor Bertrand Delouis who followed and helped me during the time that I spent in France. I thank him in particular for the kindness and sympathy that he has always shown me, despite the difficult period due to the premature death of a family member.
My gratitude also goes to Professor Ignazio Guerra, without whom I would not be in Naples for my PhD, and so would never have known all the good people that I have met here.
Obviously I express my thanks to my family, in particular to my mother and father, for all the things they have done and that they will surely continue to do for me.
Finally I want to thank and apologize to my girlfriend Rosa not only for all the complaints that she has had to hear but also for all the patience that she has had with me.

Thanks to all.

1 Introduction and Overview

The internal dynamics of the earth results in stress accumulation in specific areas. If, during this process of accumulation, the limit of break-resistance of the material is exceeded, a crustal fracture is generated (seismic source) with consequent energy release in the form of seismic waves.

Understanding the characteristics of the seismic source plays a very important role, not only to increase scientific knowledge of the phenomenon that can cause an earthquake, but also for the study of the soil displacement generated by the earthquake and the possible consequences upon structures (buildings, infrastructures etc…) stricken by this energy (seismic risk).

Study of the seismic source is performed particularly by analysis (inversion) of recorded seismograms (seismic waves) at seismic stations. Initially, the analysis was focused on the study of long-period components of seismic waves using the point-source approximation; from this point of view the source of the earthquake is generally represented by the moment tensor, which contains information on the

fault size, magnitude, fault plane orientation and also the faulting style. Subsequently, the evolution of theoretical knowledge of the source in terms of relationships between frequencies and soil acceleration, combined with the development of more powerful computing machines, led to focus on the low period components. This step resulted in obtaining ever greater details on the dynamics of the source of an earthquake.

Another important source of information in the study of the source characteristics can be given by the analysis of the static deformation field registered with satellite techniques (e.g. InSAR, GPS etc). The inversion of the static field, instead, is very important since it allows to introduce in our source model different constraints, such as at the seismic moment or the presence or not of slip near the surface.

The breaking process can be studied either by a kinematic or dynamic type of approach. The use of this latter is closely related to knowledge of the distribution of the stress that triggers the earthquake as well as to the strength of materials subject to fracture. The kinematic approach instead, regardless of the dynamic conditions, needs a description of the characteristics of the rupture by means of a few parameters, such as, for example, dimensions of the source, distributions of final displacement, rupture velocity and rise time. It seems therefore clear that when considering the seismic source from the kinematic point of view we get a reasonable simplification in the representation of the seismic radiation emitted during the fracture process because, once set the macroscopic parameters (seismic moment, stress drop, focal mechanism, geometry of fault, ...), it will depend only on the heterogeneity of the rupture velocity, slip and rise time on the fault.

In any case, when we want to determine the source parameters from the analysis (inversion) of seismograms, also a kinematic description of the seismic source may become complicated to deal with. In fact, the presence of a heterogeneous distribution of propagation speed of the rupture makes strongly non-linear the relationship between the data and the parameters of the source, which, for all

practical purposes, will result in the need to use a search method capable of sampling the space of models widely enough in the process of inversion. Considering this, if we do not want to use an approach that linearizes the dependence of the data on the parameters, we must have a method of computing the forward problem (synthetic seismograms) at the base of the inversion process, accurate and fast as regards the calculation time. Once defined the forward problem, it is necessary to implement the method of data inversion. For this purpose we need to define a misfit function that takes into account the more or less good agreement between the observed and simulated data and determines the distribution of the model's parameters optimizing this function through an appropriate search engine.

PhD work carried out in these years has had as its subject the study of kinematic rupture property of the seismic source, through the inversion of both static and dynamic fields generated by the earthquake itself.

In this context, in the first work we investigate the fault geometry of the Christchurch earthquake (New Zealand, February 21, 2011) from the analysis of the GPS and InSAR data-sets and then we derive a kinematic source model from the joint inversion of all the available strong-motion, GPS and InSAR data-sets. To analyze the Christchurch earthquake we used the non-linear inversion method based on the simulated annealing algorithm, developed by Delouis *et al.* (2002). This method was modified during this PhD thesis to account for both the exploration of fault geometry and estimation of errors associated to retrieve parameters. Particular importance was also given to different preliminary analyzes performed on the original data-sets.

For this work we considered a complete set of data consisting of both the dynamic range of deformation (strong-motion data) and the static one (InSAR and GPS data).

The use of the kinematic model of rupture of an event during the inversion process

of the static field of deformation is very important in that, unlike the dynamic range, it not only allows to perform studies relating also to spatial position of the source, but also to introduce additional constraints on the final distribution of the source parameters on the fault plane.

During this work particular importance has been given to the study of the resolution of the final model obtained and to the analysis of the errors in the distribution of the source parameters through the study of the distribution of marginal probability, built from the final breaking model obtained during the exploration process.

In a second phase a novel inversion technique was developed, based on direct analysis of the apparent Source Time Function (aSTF) of a seismic event. The idea behind this work is to minimize all the main error sources during the process of simulation of synthetic seismograms.

In fact, several studies have been made to simulate theoretically and empirically the propagation of short-period seismic waves in a heterogeneous and therefore realistic structure of the Earth. These studies show that the excitation of high frequency seismic waves is strongly dependent not only on the complexity of the source processes associated with heterogeneity on the fault (which is what we want to study), but also on attenuation and scattering site effects along the propagation path (propagation effects). All these factors, if not duly taken into account during the simulation process of ground motion, can strongly influence the final result.

The solution of all these problems has been obtained in this work through the deconvolution of seismic radiation studied for its Empirical Green Function.

To summarize, the work carried out during my PhD assignment was mainly focused on the study and development of different techniques for the construction of the kinematic model of rupture of a seismic event.

Chapter 2: This chapter deals with the basic theoretical concepts of elasto-dynamic (strong-motion data) and elasto-statics (InSAR and GPS data) and their application to the study of the seismic source.

Chapter 3: In this chapter we describe the fundamental theory of inversion, distinguishing between the linear, linearized and non-linear inverse problem approaches. In the final part of the Chapter, we give particular emphasis to the description of the global optimization strategy (Simulated Annealing Algorithm and Genetic Algorithm) used for the methods developed in this PhD work.

Chapter 4: The space-time distribution of the coseismic slip of the 21 February 2011, Mw 6.2, Christchurch earthquake, New Zealand, is explored through a joint inversion of geodetic and strong-motion data. The geodetic data consist of both Global Position System (GPS), from campaign and continuous stations, and synthetic aperture radar (SAR) interferograms from two ascending satellite tracks. The strong motion data consist of 10 stations located in the Canterbury Plain, these stations offering a good azimuthal coverage of the event.

The kinematic rupture model for the analyzed event was obtained using the parameterization and nonlinear inversion scheme proposed by Delouis *et al.* (2002) In particular, for any subfault we explore for the local source time function (local slip history), slip direction, and rupture onset time. The geometry of the fault plane used for the kinematic inversion is inferred from the analysis of the geodetic data. To validate our results we perform a resolution study for both the single and complete data sets, and an error analysis of our final kinematic rupture model.

Chapter 5: We present an approach to infer the slip and rupture velocity distributions on the fault plane from the non-linear inversion of the apparent Source Time Functions (aSTFs), obtained from the Empirical Green Function deconvolution method. The main advantage of this technique is that it allows overcoming, in the forward modeling, the limitations related to the computation of the Green function, as the choice of a correct and reliable earth propagation model. We perform a parameter resolution and uncertainty study, which is based on the analysis of the misfit function in the neighbourhood of the best-fit model. In this chapter we present the results obtained by applying the technique to synthetic and

real records from an Mw 4 event occurred during the 2009 L'Aquila (Central Italy) aftershock sequence.

Chapter 6: We report here the final considerations of my PhD work.

2 The Seismic Source

2.1 Introduction

An earthquake is a direct result of a fracturing process that occurs in the earth's crust. The rupture is a consequence of the variation from the state of equilibrium. A given volume of matter is subject to several sources of stress, for example: the weight of the overlying materials (lithostatic load), the pressure forces associated with the tectonic movements, movement of fluids etc.

The equilibrium state is broken when the strains accumulated reach the material's mechanical strength limits; when this happens there occurs a seismic fracture. Once the stress is released the region returns to a state of equilibrium; if the tectonic movements persist, the stress will accumulate again. An earthquake is therefore interpreted as a rock displacement along a surface (fault plane) inside a volume. Generally the fault size ranges from millimetres (rock samples in laboratory experiments) to thousands of kilometres (North Anatolian fault, San Andreas

Fault).

The chance that an area could produce a seismic rupture process and then an earthquake is closely influenced by the thermal regime in the area. Most of the earthquakes indeed occur in the most superficial portions of the earth's crust, in which the relatively low temperature ensures elastic behaviours of materials. In the deeper crust portions instead the high temperature leads to a ductile behaviour of the materials.

The most important consequences of a rupture process are the generation of dynamic events (elastic waves) and a static deformation field in the surrounding areas. In this chapter we want to provide the main basic mathematics required to compute both these fields.

2.2 Elastic waves in homogeneous media

The motion of each point of a generic volume V is completely determined when we know the forces acting inside and the stress agents on its surface S. In this case, according to Euler's formulation, Newton's second law for continuous media is

2.1

$$\int_V F_i dV + \int_S T_i dS = \frac{d}{dt}\int_V \rho v_I dV$$

where F_i are the forces acting on the volume element dV, T_i are stresses acting on the surface dS, ρ is the density and v_I is the velocity of each point of the volume.

In terms of the stress tensor τ ($T_i = \tau_{ij}\eta_j$) and applying the Gauss theorem to the surface integral, we get

2.2

$$\int_V \left(F_i + \frac{\partial \tau_{ij}}{\partial x_j}\right) dV = \frac{d}{dt}\int_V \rho v_I dV$$

If the density is independent from time, the equation can be written as follows

2.3

$$\frac{\partial \tau_{ij}}{\partial x_j} + F_i = \rho \frac{dv_i}{dt}$$

On the other hand, the total derivative of the velocity with respect to time can be written as

2.4

$$\frac{dv_i}{dt} = \frac{\partial v_i}{\partial t} + v_j \frac{\partial \tau v_i}{\partial x_j}$$

but considering infinitesimal deformation and very small speed variations with the distance, the second order terms can be neglected and thus the total derivative can be approximated by the partial derivatives

2.5

$$\frac{\partial}{\partial x_j}(C_{ijkl}\varepsilon_{kl}) + F_i = \rho \frac{\partial^2 u_i}{\partial t^2}$$

where the stress and the velocity (v_i) are expressed in terms of deformation ($\tau_{ij} = C_{ijkl}\varepsilon_{kl}$, where C_{ijkl} is the elastic tensor) and displacement for an elastic medium respectively, $\varepsilon_{ij} = \frac{1}{2}\left(\frac{\partial u_i}{\partial x_j} + \frac{\partial u_j}{\partial x_i}\right)$ and considering elastic constant coefficients, we have

2.6

$$C_{ijkl}\frac{\partial^2 u_k}{\partial x_l \partial x_j} + F_i = \rho \frac{\partial^2 u_i}{\partial t^2}$$

For homogeneous and isotropic media C_{ijkl} can be written in terms of Lame's

coefficient so that the equation 2.6 becomes

2.7

$$(\lambda + \mu)\nabla(\nabla \cdot \boldsymbol{u}) + \mu\nabla^2\boldsymbol{u} + \boldsymbol{F} = \rho\ddot{\boldsymbol{u}}$$

Given the mass forces **F**, the solution of 2.7 provides the displacement field for elastic continuous, homogeneous, isotropic and infinity media.

A common alternative form of this equation employs the vector identity

2.8

$$\nabla^2\boldsymbol{u} = \nabla(\nabla \cdot \mathbf{u}) - (\mu\nabla\times\nabla\times\boldsymbol{u})$$

Allowing (2.7) to be written as

2.9

$$(\lambda + 2\mu)\nabla(\nabla \cdot \boldsymbol{u}) - (\mu\nabla\times\nabla\times\mathbf{u}) + \boldsymbol{F} = \rho\ddot{\boldsymbol{u}}$$

Equations 2.7 and 2.9 are complicated, 3D, partial differential equations for displacements in a continuum, initiated by non-specified source.

The processes behind an earthquake can be described using a system of mass forces acting in the focal region. Outside this region the mass forces agents are only gravitational (F = mg) and except for the very large period (T> 600 s) seismic waves, the influence of gravity is very small and therefore neglected. So, considering the Earth as an unbounded medium, we can use the equation 2.21 to determine the elastic displacement outside the focal region.

2.3 The Green Function

Neglecting the gravitational forces, the mass forces that appear in the equation of motion (equation 2.7) can be used to describe the processes that generate earthquakes. Generally speaking, these forces **F** (**x**, t) which can be thought of as

being functions of spatial coordinates and time, may be different from one earthquake event to another and are defined only within a certain volume (focal region).

An example of time dependence is the harmonic function

2.10

$$F(\boldsymbol{x}; t) = F(\boldsymbol{x})e^{iwt}$$

In seismology this form of time dependence simplifies the solution of several problems. Indeed, harmonic functions, although not realistic, can be used to find more complex solutions for time dependent functions using the Fourier transform operator.

One important kind of mass force for many solutions of elasto-dynamic problems is provided by a time and space unit impulse with arbitrary direction. This force can be mathematically represented using the Dirac's Delta function:

2.11

$$F_i(x_s; t) = \delta(x_s - \hat{\imath}_s)\delta(t - \tau)\delta_{in}$$

The force is applied to the coordinates $\hat{\imath}_s$ at the time τ and is zero outside these space-time coordinates. The orientation of this force is identified by the associated components with the index n. If we replace this force in the equation 2.1, the solutions that are obtained represent the elastic displacement as a function of time at each point of coordinates **x** in a certain volume V surrounded by a surface S.

Each component of the displacement (n index) depends on the orientation of the force (i index) and then the displacement is a second order tensor of components $G_{ni}(x_s, \hat{\imath}_s; t, \tau)$, which is a function of the space-time coordinates (x_s, t) at every point V and of the coordinates and time of the application point of the force ($\hat{\imath}_s$, τ).

Replacing in the equation of motion and taking into account the stress function of the displacement we get

2.12

$$\int_V \rho \ddot{G}_{ni} dV - \int_S C_{ijkl} \frac{\partial G_{nk}}{\partial x_l} dS = \int_V \delta(x_s - \hat{\imath}_s)\delta(t-\tau)\delta_{in} dV$$

Applying the Gauss theorem for an elastic, homogeneous and infinite medium we can write the previous equation as follows:

2.13

$$\rho \ddot{G}_{ni} - C_{ijkl} \frac{\partial G_{nk}}{\partial x_l} = \delta(x_s - \hat{\imath}_s)\delta(t-\tau)\delta_{in}$$

The solutions of the equations 2.12 and 2.13 are the elastic displacements generated by an impulsive force in space and time, which is why the tensor **G** is called the elasto-dynamic Green function. The Green function depends on the space characteristics, the elastic coefficients and density. What is more, in a finite space it also depends on the shape of the volume V and the boundary conditions on the surface S. For any propagation space there is a different Green function that defines how the medium mechanically responds to an impulsive excitation and is therefore a space characteristic.

2.4 The reciprocity and representation theorems

Let us consider an elastic space of volume V surrounded by a surface S. For a forces mass system f acting on each volume element dV and stress $\mathbf{T}_u$, let "u" be the resulting displacement. In the same volume we have a second forces system **g** and stress $\mathbf{T}_w$, which provide a displacement **w**. It can be shown (Aki and Richards, 1980) that Betti's reciprocity theorem applies so that:

2.14

$$\int_V (f_i - \rho \ddot{u}_i) w_i dV + \int_S T_i^u w_i dS = \int_V (g_i - \rho \ddot{w}_i) u_i dV + \int_S T_i^w u_i dS$$

Betti's theorem relates the corresponding displacements of two forces and stress systems that act in the same volume. Reorganizing and time-integrating the terms of equation 2.12 we get

2.15

$$\int_{-\infty}^{+\infty} dt \int_V \rho(u_i \ddot{w}_i - w_i \ddot{u}_i) dV$$

$$= \int_{-\infty}^{+\infty} dt \int_V (u_i g_i - w_i f_i) dV + \int_{-\infty}^{+\infty} dt \int_S (u_i T_i^w - w_i T_i^u) dS$$

This equation is a generalized form of Betti's theorem, known as Green-Volterra formula.

An interesting case is when the displacements and velocities are zero before a specific time. This implies the causality principle because the space is not energized until the motion begins. Under this condition we find the following (Aki and Richards, 1980)

2.16

$$\int_{-\infty}^{+\infty} dt \int_V (u_i g_i - w_i f_i) dV = + \int_{-\infty}^{+\infty} dt \int_S (w_i T_i^u - u_i T_i^w) dS$$

In seismology this is an important result because it allows a representation of the displacement of given forces and stress system (complex) as a function of one produced by a different system that might be known and simpler.

The simplest system of forces that could be used is represented by a force impulse unitary in space and time. Under these conditions, as seen above, the corresponding displacement is given by the Green function.

Replacing **g** with the equation 2.11 in 2.16, "w" in the same equation with the Green tensor **G** and after some mathematical manipulations (Aki and Richards,

1980) we find the following:

2.17

$$u_n(u_s;t) = \int_{-\infty}^{+\infty} dt \int_V f_i G_{ni} dV + \int_{-\infty}^{+\infty} dt \int_S \left(G_{ni} T_i - C_{ijkl} u_i \frac{\partial G_{nk}}{\partial \xi_l} \nu_j \right) dV$$

This result is known as the "Representation Theorem". The equation is used to determine the displacements produced by a system of elastic forces defined in a volume and by a stress and displacement system defined on a surface, using the Green function. In this equation the Green function is a "propagator"; in fact it allows propagating forces, stress or displacement effects, defined at (**î**; t) to determine the elastic displacements at (**x**, t).

Generally the determination of the Green function is complex and the difficulties increase with the complexity of the considered propagation space. The advantage of using the Representation Theorem, however, is related to the possibility for a specific space to solve the equation of motion only once to determine the Green function and then use the results obtained results to propagate different forces and strain systems in the same space.

2.5 Kinematic models of Seismic Source

In seismology, understanding the mechanics of the seismic source requires correlation of the seismic waves observed to the parameters that describe the source: in the forward problem, seismic waves are obtained starting from the theoretical models for the source, while in the inverse problem the parameters of the model for the source are derived from the seismic waves observed. In both approaches, the first step will be the definition of the seismic source in terms of a mechanical model physically representing the fracture. These models, or representations of the seismic source, are defined by a number of parameters that influence the complexity of the models themselves: simple models are associated

with few parameters while more complex models will require a higher number of them (Madariaga, 1983; Koyama, 1997).

The seismic fracture problem can be approached using a kinematic or dynamic point of view.

The kinematic models are a simplification of a real fracture process involving *a priori* assumptions in the definition of the shape of the Source Time Function (STF) and stopping conditions of the rupture at the fault borders. In these models the rupture processes are studied independently from the stress that caused them. This type of models, however, is very important for the interpretation of seismograms and estimating the source parameters: seismic moment, orientation of the fracture etc.

The second approach connects instead the fracture process, the mechanical properties of the material in the focal zone and the agents' stress. The dynamic models are very complex and in most cases their solution can be obtained only by using numerical methods.

2.6 Fractures and Dislocations

A mechanical representation of the earthquake source can be obtained in terms of fractures or dislocations that occur in an elastic medium. Volterra developed the elastic theory of dislocations first in 1907 (Love, 1945).

A dislocation is a displacement or deformation discontinuity through an internal surface of an elastic medium. For this discussion we consider only displacement dislocations, and so the stress is always continuing along the internal surface and the problem will be solved using the Representation Theorem in terms of the Green function (equation 2.17). The focal region is a surface Σ with two sides, a positive and a negative one. This surface can be considered as derived from the focal volume V_0 that is flattened to form a surface with the two sides stuck together. We

denote with ξ_i the surface local coordinates and with $n_i(\xi_k)$ the normal vector to its points. If there is a displacement discontinuity (*slip*) from side to side of this surface, it shall be given by the equation

2.18

$$u_i^+(\xi_k;t) - u_i^-(\xi_k;t) = \Delta u_i(\xi_k;t)$$

where the superscripts + and - are the displacements measured on the positive and negative sides of the surface Σ. In absence of mass forces (F = 0), the stresses are continuous through Σ and the conditions on the external surface Σ are continuous too. We can write the equation 2.17 as follows

2.19

$$u_n(x_s;t) = \int_{-\infty}^{+\infty} d\tau \int_{\Sigma} \Delta u_i(\hat{\boldsymbol{\imath}}_s;\tau) C_{ijkl} n_j(\hat{\boldsymbol{\imath}}_s) \frac{\partial G_{nk}(x_s,\hat{\boldsymbol{\imath}}_s;t,\tau)}{\partial \xi_l} dS$$

In this formulation the seismic source is represented by a dislocation (or displacement discontinuity) defined by the slip vector Δu on the surface Σ, which corresponds to the relative displacement of the two fault sides. This discontinuity is non-elastic, thus even if the stress became zero, they would remain. In the general case, $\Delta u(\xi_i,\tau)$ may have a different direction for each ξ_i point of the surface Σ and, for each of these points, it may change in time from a zero value at t = 0 up to a maximum value for a particular instant. The normal to the surface Σ, denoted by the unit vector n(Σ), can have different direction for each surface point but, in general, it is considered constant since it is assumed that Σ is a plane. Green's function **G** includes the effects of the medium on the propagation from the point ξ_i, on the surface Σ, to the point x_i where we want to evaluate elastic displacements. To solve the problem according to the equation 2.19 we need to know the Green function or better its derivatives.

The equation 2.19 corresponds to a kinematic source model, so a model for which the elastic displacements **u** are derived from the slip vector Δu that we must know *a priori*, rather than being derived from stress conditions in the focal region as is done for dynamic models. After some mathematical steps in equation 2.19 we can replace the vector Δu with the function $\Delta \dot{u}$, which represents the velocity dislocation function (slip rate). As a consequence, the elastic displacement does not depend on the slip by but on the slip rate. This means that the source radiates elastic energy only when it moves.

As a special case, we consider an isotropic medium, whose Lamé coefficients are λ and μ. Using this notation for the elastic constant we can write the equation 2.19 as follows:

1.20

$$u_n(x_s;t) = \int_{-\infty}^{+\infty} d\tau \int_{\Sigma} \Delta u(t)\left[\lambda l_k n_k \delta_{ij} + \mu\left(l_i n_j + l_j n_i\right)\right] \frac{\partial G_{ni}}{\partial \xi_l} dS$$

2.7 The Green function for a homogeneous elastic whole space

As said above, the Green function represents the solution of the wave equation for an impulsive force in space and time.

For an elastic, homogeneous, isotropic and infinite space, if the force is applied in the origin of the reference system at time t = 0 the Green function is the solution of the equation

2.21

$$\rho \ddot{\boldsymbol{u}} = \rho \boldsymbol{f} + (\lambda + \mu)\nabla(\nabla \cdot \boldsymbol{u}) - \mu \nabla \times \nabla \times \boldsymbol{u}$$

In this equation the body force per unit volume ($\rho \boldsymbol{f}$) is written in the time-dependent form $\rho f(t) = F(t)\delta(\boldsymbol{r})\boldsymbol{a}$ (where a is a unit vector in the direction of the force). The function F(t) is the time history of the applied body-force.

Different time histories can be used: delta functions $\delta(t)$, step function, H(t) etc. To find our solutions we use the vector identity

2.22

$$\rho \boldsymbol{f} = F(t)\delta(\boldsymbol{r})\boldsymbol{a} = -F(t)\nabla^2\left(\frac{\boldsymbol{a}}{4\pi r}\right) = -F(t)\left\{\nabla\left[\nabla\cdot\left(\frac{\boldsymbol{a}}{4\pi r}\right)\right] - \nabla\times\nabla\times\left(\frac{\boldsymbol{a}}{4\pi r}\right)\right\}$$

We search for a solution of the form

2.23

$$u(t) = \nabla(\nabla\cdot\boldsymbol{A}_P) - \nabla\times\nabla\times\boldsymbol{A}_S \quad \text{where} \quad \begin{cases}\nabla\times\boldsymbol{A}_P = 0\\ \nabla\cdot\boldsymbol{A}_S = 0\end{cases}$$

We can now split the elastodynamic equation into two different terms

2.24

$$(\lambda+2\mu)\nabla^2\boldsymbol{A}_P = \frac{F(t)}{4\pi r}\boldsymbol{a} + \frac{\partial^2\boldsymbol{A}_P}{\partial t^2}$$

$$\mu\nabla^2\boldsymbol{A}_S = \frac{F(t)}{4\pi r}\boldsymbol{a} + \frac{\partial^2\boldsymbol{A}_S}{\partial t^2}$$

With $\mathbf{A}_p = A_p\mathbf{a}$ and $\mathbf{A}_s = A_s\mathbf{a}$ we get the following scalar equations:

1.25

$$\nabla^2 A_P = \frac{F(t)}{4\pi(\lambda+2\mu)r} + \frac{1}{\alpha^2}\frac{\partial^2 A_P}{\partial t^2}$$

$$\nabla^2 A_S = \frac{F(t)}{4\pi\mu r} + \frac{1}{\beta^2}\frac{\partial^2 A_S}{\partial t^2}$$

where $\alpha = \sqrt{\frac{\lambda+2\mu}{\rho}}$ and $\beta = \sqrt{\frac{\mu}{\rho}}$ are the P and velocity, respectively. Before solving these complex equations we find the solution of the inhomogeneous wave equation

2.26

$$\nabla^2\phi(x_1,x_2,x_3,t) - \frac{1}{c^2}\frac{\partial^2\phi}{\partial t^2}(x_1,x_2,x_3,t) = g(x_1,x_2,x_3,t)$$

A form that is often used for g is

2.27

$$g(\boldsymbol{x},t) = -\delta(\boldsymbol{x})\delta(t) = -\delta(\boldsymbol{r})\delta(t)$$

The solution of the equation 2.26 is

2.28

$$\phi(\boldsymbol{x},t) = \frac{1}{4\pi}\frac{\delta(t-r/c)}{r}$$

This solution is important because it shows that the solution for a symmetric point-source impulse is an outward-propagating wave that decays in amplitude as 1/r. We know that the form of spherically symmetric waves that solves the homogeneous equation is

2.29

$$\nabla^2\phi - \frac{1}{c^2}\ddot{\phi} = 0$$

$$\phi = \frac{1}{r}f\left(t-\frac{r}{c}\right) + \frac{1}{r}g\left(t+\frac{r}{c}\right)$$

which is a standard D'Alembert-type solution. The 1/r factor is required to keep the total energy of the spreading wave front constant. Given 2.28, we can find additional solutions:

2.30

$$\nabla^2\phi - \frac{1}{c^2}\frac{\partial^2\phi}{\partial t^2} = -\delta(\boldsymbol{x}-\boldsymbol{\xi})\delta(t-\tau)$$

$$\phi(r,t) = \frac{1}{4\pi}\frac{\delta(t-\tau-|\boldsymbol{x}-\boldsymbol{\xi}|/c)}{|\boldsymbol{x}-\boldsymbol{\xi}|}$$

This solution is for a point force at time $t = \tau$ at position $x = (\xi_1, \xi_2, \xi_3)$. Another simple solution is given by

2.31

$$\nabla^2\phi - \frac{1}{c^2}\frac{\partial^2\phi}{\partial t^2} = -\delta(\boldsymbol{x} - \boldsymbol{\xi})f(t)$$

$$\phi(r,t) = \frac{1}{4\pi}\frac{f(t - \tau - |\boldsymbol{x} - \boldsymbol{\xi}|/c)}{|\boldsymbol{x} - \boldsymbol{\xi}|}$$

If the source extends in a Volume V as well as in time, we have

2.32

$$\nabla^2\phi - \frac{1}{c^2}\frac{\partial^2\phi}{\partial t^2} = -\boldsymbol{\phi}(\boldsymbol{x},t)$$

$$\boldsymbol{\phi}(\boldsymbol{x},t) = \frac{1}{4\pi}\iiint_V \frac{\boldsymbol{\phi}(\boldsymbol{\xi}, t - |\boldsymbol{x} - \boldsymbol{\xi}|/c)}{|\boldsymbol{x} - \boldsymbol{\xi}|}dV$$

which says that the field at (**x**,t) is sensitive to source activity in the element dV only at the delayed time $t - (|\boldsymbol{x} - \boldsymbol{\xi}|)$. Thus we can write solutions to eq. 2.25 as follows

2.33

$$A_P = \frac{1}{4\pi}\iiint_V \frac{-F(t - |\boldsymbol{x} - \boldsymbol{\xi}|/\alpha)}{4\pi(\lambda + 2\mu)r|\boldsymbol{x} - \boldsymbol{\xi}|}dV$$

$$A_S = \frac{1}{4\pi}\iiint_V \frac{-F(t - |\boldsymbol{x} - \boldsymbol{\xi}|/\beta)}{4\pi\mu r|\boldsymbol{x} - \boldsymbol{\xi}|}dV$$

where $\boldsymbol{\xi} = 0$ for a point source at the origin. Now we must integrate over the volume around **x**. Given the distance $|\boldsymbol{x} - \boldsymbol{\xi}| = \alpha\tau$ (where τ is the transit time), it can be shown that

2.34

$$A_P = \frac{1}{4r\pi\rho}\left(\int_0^\infty F\left(t-\left(\frac{r}{\alpha}\right)-\tau\right)\tau d\tau - \int_0^\infty F(t-\tau)\tau d\tau\right)$$

$$A_S = \frac{1}{4r\pi\rho}\left(\int_0^\infty F\left(t-\left(\frac{r}{\beta}\right)-\tau\right)\tau d\tau - \int_0^\infty F(t-\tau)\tau d\tau\right)$$

This displacement field is obtained by computing the equation

2.35

$$\boldsymbol{u} = \nabla(\nabla\cdot\boldsymbol{A}_P) - \nabla\times\nabla\times\boldsymbol{A}_S$$

Given a single body force F(t) applied at the origin in the x1 direction, the equation 2.34 becomes

2.36

$$u_i(\boldsymbol{x},t)$$
$$= \frac{1}{4r\pi\rho}\left(\frac{\partial^2}{\partial x_i\partial x_1}\frac{1}{r}\right)\int_{r/\alpha}^{r/\beta}\tau F(t-\tau)\tau d\tau + \frac{1}{4r\pi\rho\alpha^2}\left(\frac{\partial^2 r}{\partial x_i\partial x_1}\right)F\left(t-\frac{r}{\alpha}\right)$$
$$+\frac{1}{4r\pi\rho\beta^2}\left(\delta_{ij}\frac{-\partial^2 r}{\partial x_i\partial x_1}\right)F\left(t-\frac{r}{\beta}\right)$$

In the general case of a point force in the x_j direction, we have the classic Stokes solutions:

2.36

$$u_i(\boldsymbol{x},t)$$
$$= \frac{1}{4\pi\rho}\left(3\gamma_i\gamma_j-\delta_{ij}\right)\frac{1}{r^3}\int_{r/\alpha}^{r/\beta}\tau F(t-\tau)\tau d\tau + \frac{1}{4\pi\rho\alpha^2}\gamma_i\gamma_j\frac{1}{r}\left(\frac{\partial^2 r}{\partial x_i\partial x_1}\right)F\left(t-\frac{r}{\alpha}\right)$$
$$-\frac{1}{4\pi\rho\beta^2}\left(\gamma_i\gamma_j-\delta_{ij}\right)\frac{1}{r}F\left(t-\frac{r}{\beta}\right)$$

where the parameters γ_i is the cosine direction ($\gamma_i = x_i/r = \partial r/\partial x_i$). In the equation 2.36 the first term behaves like $1/r^2$ (*near-field* term) while the other behaves like $1/r$ (*far-field* terms).

2.8 Finite dimensions fault: Kinematic models

A realistic representation of the seismic source must include the fault dimensions and their effects on the seismic radiation. The models developed of extended source were first kinematic, describing dislocations that propagate on a finite surface area.

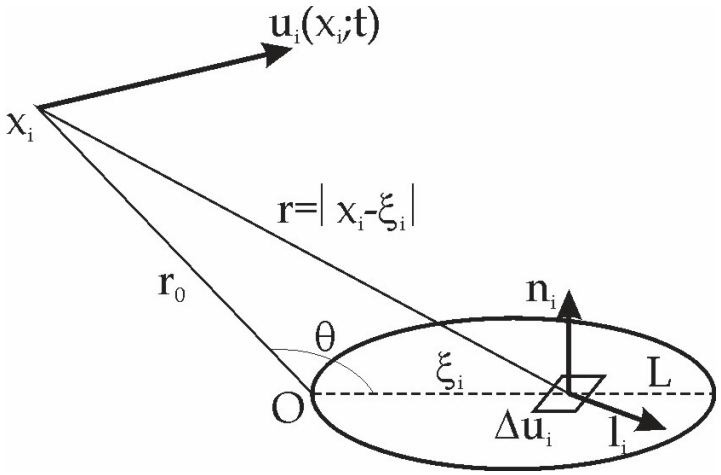

Figura 2.1: An extended source of size L, slip Δu at the point x_i, which produces an elastic displacement u in x_i

The general characteristics of the kinematic models of an extended source are: a surface Σ on which a dislocation $\Delta u(\xi_i)$ propagates in a given direction with a constant velocity, from the origin ($\xi_i = 0$) to a final distance L (Figure 2.1); the rupture velocity assumed constant and less than the wave propagation velocity in the considered earth model ($v < \beta < \alpha$).

It can be shown that the dislocation for the P waves, in the far-filed approximation, is given by the equation

2.37

$$u_i^P = \frac{\mu}{4\pi\alpha^3}\int_\Sigma \frac{\Re(n_k, l_k, \gamma_k)}{r}\Delta\dot{u}\left(\xi_i; t - \frac{r}{\alpha}\right) dS$$

where $r = |x_i - \xi_i|$ is the distance between the observation point **x** and a generic source point (ξ), $\Re(n_k, l_k, \gamma_k)$ is the radiation pattern, which depends on the orientation of the source (**l**,**n**) and the location of the observation point (γ_i).

If we are interested only in the time function of the waveform at a point at a distance r_0 from the origin (Figure 2.2), we can simply compute the integral

2.38

$$u(t) = \int_\Sigma \Delta\dot{u}\left(\xi_i; t - \frac{r}{\alpha}\right) dS$$

Expanding r in the Taylor series around r_0 and neglecting the ξ_i terms following the first, we find

2.39

$$r \cong r_0 - \xi_i\gamma_i$$

Being ξ_i^2/r_0 the second order term and L the maximum value of ξ_i, the approximation 2.39 is correct for displacement characterized by wavelength λ for which $\lambda r_0 \gg L^2$. Under these conditions the elastic displacements for the P wave is

2.40

$$u(t) = \int_\Sigma \Delta\dot{u}\left(\xi_i; t - \frac{r_0 - \xi_i\gamma_i}{\alpha}\right) dS$$

The Fourier transform of the previous equation is

2.41

$$U(\omega) = \int_{\Sigma} dS \int_{-\infty}^{\infty} \dot{\Delta u}(t) e^{-i\omega(t-\frac{r_0-\xi_i\gamma_i}{\alpha})}\, dt$$

Indicating the Fourier transform of $\Delta u(t)$ with $\Delta U(\omega)$, $U(\omega)$ is given by the following

2.42

$$U(\omega) = e^{i\omega r_0/\alpha} \int_{\Sigma} i\omega \Delta u(\xi_i;\omega)\, e^{-i\omega\gamma_i\xi_i/\alpha} dS$$

The Fourier transform of the elastic displacement $U(\omega)$ takes the form of a spatial Fourier transform on the fault plane of the Fourier transform of the slip $\Delta U(\omega)$. The exponential $\omega\gamma_i/\alpha = k\gamma_i$ that appears in equation 2.41 represents the projection of the wave number *k* on the fault plane Σ.

If the time history of the slip function is expressed by a Heaviside function ($\Delta u(\xi_i, t) = \Delta u(\xi_i)H(t)$), its Fourier transform is $\Delta u(\xi_i)/(i\omega)$, and replacing in equation 2.41 we have

2.43

$$U(\omega) = e^{i\omega r_0/\alpha} \int_{\Sigma} i\omega \Delta u(\xi_i)\, e^{-i\omega\gamma_i\xi_i/\alpha} dS$$

For low frequencies we find

2.44

$$U(\omega \longrightarrow 0) \approx \mu \int_{\Sigma} \Delta u(\xi_i)\, dS \approx \mu < \Delta u > S = M_0$$

The spectral amplitude is proportional to the seismic moment. The constant proportionality depends on factors shown in equation 2.37. If the slip does not change its sign, the spectral width at high frequencies will tend to zero.

The general shape of the amplitude spectrum $U(\omega)$, corresponding to a finite size source is constant at low frequencies and, as we shall discuss below, starts to decrease from a frequency which is proportional to the inverse of the source size. The behaviour of the spectrum at high frequencies is $1/\omega^{\varepsilon}$, where ε takes values between 0 and 3 and generally equals 2 (Aki, 1967).

2.9 The Haskell model

The kinematic finite dimensions source model, known as a Haskell model (1964), is characterized by a rectangular fault of length L and width W. The Haskell model is also characterized by fractures that propagate only along the direction L with a constant velocity v (Figure 2.2). The rupture process occurs in a homogeneous, elastic, isotropic and unlimited space; we make this choice in order to minimize the propagation effects and to focus our attention only on the related source phenomena.

Skipping the mathematical steps, shown by Aki and Richards (1980), and assuming that the receiver is sufficiently far from all points of the fault, only the far-field terms produce significant contribution for the Green function computation; in this case it can be shown that P waves displacement spectrum to the receiver located in **r** is given by the following equation

2.45

$$U(\boldsymbol{r},\omega) = \frac{\mu \Re}{4\pi\rho r\alpha^3} WL\omega\Delta u(\omega)\frac{\sin X}{X} e^{\left[-i\left(\frac{\omega r}{\alpha}+X-\frac{\pi}{2}\right)\right]}$$

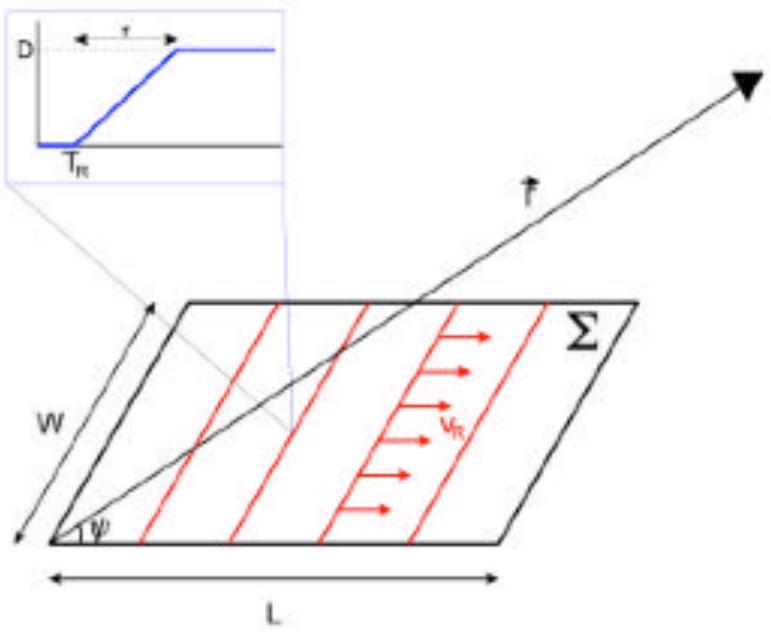

Figure 2.2: Haskell Source Model

being $\Re$ the *radiation pattern* and

2.46

$$X = \frac{\omega L}{2}\left(\frac{1}{v} - \frac{\cos\psi}{\alpha}\right)$$

with the ψ angle shown in figure 2.2.

The shape of the amplitude spectrum is defined by the $\frac{\sin X}{X}$ factor. For given values of ψ and L, X depends only upon ω and therefore the $\frac{\sin X}{X}$ at low frequencies tends to 1 while at high frequencies decreases at $1/\omega$ rate.

The spectrum shape 2.44 also depends on the shape of $\Delta u(\omega)$. If the STF (Source Time Function) has a linear ramp shape (Figure 1.2):

2.47

$$\Delta u(t) = \begin{cases} 0 & per\ t < 0 \\ \dfrac{D}{\tau} t & per\ 0 < t < \tau \\ D & per\ t > \tau \end{cases}$$

Calculating the Fourier transform of 2.47 and substituting in 2.45 we have that

2.48

$$U(\boldsymbol{r}, \omega) = \frac{\mu \Re}{4\pi \rho r \alpha^3} WLD \frac{\sin X}{X} \frac{e^{-i\omega t} - 1}{\omega \tau} e^{\left[-i\left(\frac{\omega r}{\alpha} + X - \frac{\pi}{2}\right)\right]}$$

This last equation provides the analytical solution for calculation of the displacement spectrum associated to the Haskell source. Of course, displacement time function could be obtained calculating the anti-Fourier transform of 2.48. At high frequencies the spectrum highlights in equation 2.48 decreases as $1/\omega^2$. Figure 2.3 represents the spectrum as a function of frequency logarithm. Its shape is constant at low frequencies but starting from a particular frequency (ω_c), generally called corner frequency, its envelope is a straight line of slope -2 (Figure 2.3). This particular form of the spectrum is the combined result of finite size source effects and rise time.

The real seismic waves spectra show these characteristics also showing the finite size of the source and confirming the rise time (τ) (Aki, 1967).

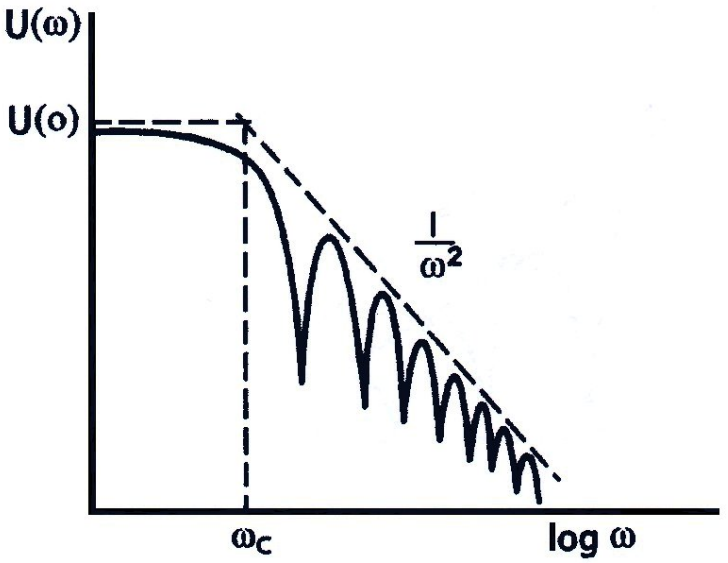

Figure 2.3: Amplitude spectrum of seismic waves corresponding to an Haskell source model

The influence of the finite size of the source can be isolated introducing the directivity function $D(\omega)$, defined by Ben-Menahem (1961) as the ratio of the spectral amplitudes of the waves that leave the source in the opposite direction (y and y + p). According to 2.45 and 2.46 this ratio is given by

2.49

$$D(\omega) = \frac{\sin\{[\omega L/2c](c/v - \cos\psi)\}(c/v + \cos\psi)}{\sin\{[\omega L/2c](c/v + \cos\psi)\}(c/v - \cos\psi)}$$

where c is the seismic phase velocity propagation considered. This function is characterized by a series of maximum and minimum depending on L and v and it can be used to determine the source and the velocity rupture.

The spectrum associated with a Haskell model where the rupture propagates in a bilateral way presents two corner frequencies (figure 2.4), ω_1 and ω_2, instead of only one (Savage, 1972). For P and S waves, $v = 0.9\beta$; ω_1, ω_2 and ω_3 are given by

2.50

$$P:\begin{cases}\omega_1 = \frac{\alpha}{2L}\\ \omega_2 = \frac{2.4\alpha}{W}\\ \omega_3 = \frac{2.9\alpha^2}{LW}\end{cases} \qquad S:\begin{cases}\omega_1 = \frac{3.6\beta}{L}\\ \omega_2 = \frac{4.1\beta}{W}\\ \omega_3 = \frac{14.8\beta^2}{LW}\end{cases}$$

The corner frequencies associated with P waves are always smaller than those associated to the S waves. Generally, the corner frequencies observed correspond to ω_3 from which we can evaluate the source size:

2.51

$$(LW)^{1/2} = \frac{1.7\alpha}{\omega_c^P} = \frac{3.8\beta}{\omega_c^S}$$

Differences between ω_1, ω_2 and ω_3 depend on the relative dimension of L and W: if W << L, when the fault is long and narrow, the difference between the frequencies is large; on the opposite, if $L \approx W$, then the three frequencies are very close.

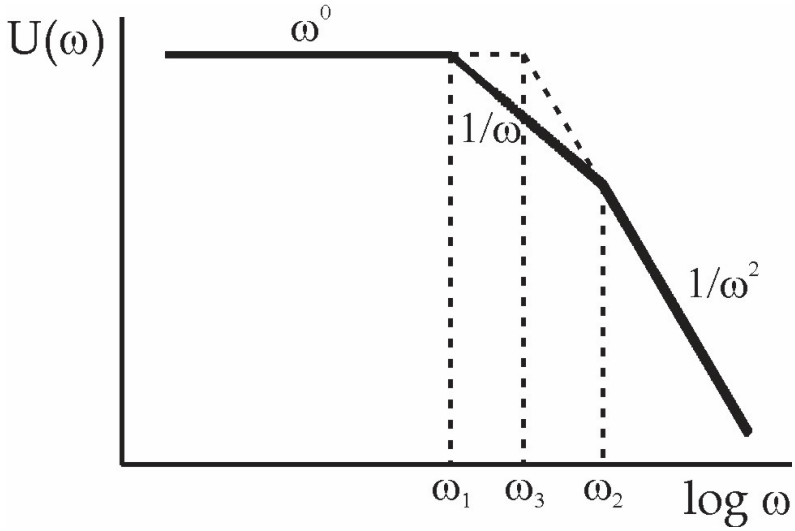

Figure 2.4: Amplitude spectrum corresponding to a Savage (1972) source model.

2.10 The Source Time Function

The Source Time function (STF) gives the time dependence of the slip function on the fault. Functions commonly used to represent the STF are (Figure 2.5):

2.52

$$\Delta u(t) = \Delta u H(t)$$

$$\Delta u(t) = \begin{cases} \dfrac{\Delta u}{\tau}; & 0 \le t \le \tau \\ \Delta u; & t > \tau \end{cases}$$

$$\Delta u(t) = \Delta u\left(1 - e^{-t/\tau}\right)$$

In all previous cases the displacements begin at time t = 0 and reach a maximum *slip* value Δu.

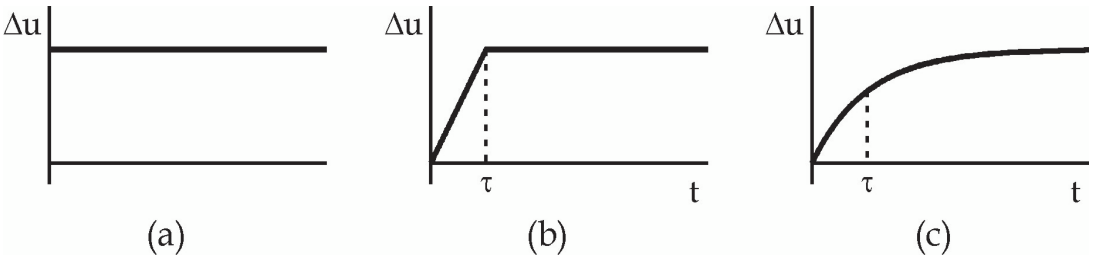

Figure 2.5: Source function examples: (a) step function; (b) a ramp function with rise time τ; and (c) an exponential function with rise time τ.

In the first equation 2.52, $\Delta u(t)$ has the shape of a Heaviside function and reaches its maximum value instantaneously at time t = 0. In the second case 2.52, $\Delta u(t)$ increases linearly between t = 0 and $t = \tau$ and at this time reaches its maximum value. STF introduces the source parameter τ, which shows the time necessary to reach its maximum displacement value (rise time). In the third case 2.52, $\Delta u(t)$ is a continuous function for t> 0 and the dislocation reaches its maximum value asymptotically. The elastic displacements sometimes depend directly on slip rate

$\Delta\dot{u}$. For the first two models we have

2.53

$$\Delta\dot{u}(t) = \Delta V \delta(t)$$
$$\Delta\dot{u}(t) = \Delta V [H(t) - H(t-\tau)]$$

In both cases, for t = 0, the slip rate instantly leaps from 0 to its maximum value ΔV (Figures 2.6a and 2.6b). In the first case, the slip rate is an impulse, while in the second case it is characterized by duration τ. More realistic STF present a velocity slip that increases from zero to its maximum value and then decreases to zero after a certain time.
A model that satisfies these conditions is a triangular function (Figure 2.6c):

2.54

$$\Delta\dot{u}(t) = \begin{cases} 0, & t < 0 \\ \Delta V \dfrac{2t}{\tau}, & 0 \le t \le \dfrac{\tau}{2} \\ \Delta V \dfrac{2(\tau - t)}{\tau}, & \dfrac{\tau}{2} \le t \le \tau \\ 0, & t > \tau \end{cases}$$

The slip rate increases linearly from zero at t = 0 reaching the maximum value (ΔV) at time $t = \tau/2$ and then decreases linearly to zero at time $t = \tau$. During the first part of the process, the slip acceleration ($\Delta\ddot{u}$) is positive, while in the second part it is negative. If we increase the duration of the source, we can use a trapezoidal STF (Figure 1.6d). In this case the slip rate keeps its maximum value for a certain time interval before decreasing to zero at $t = \tau$.

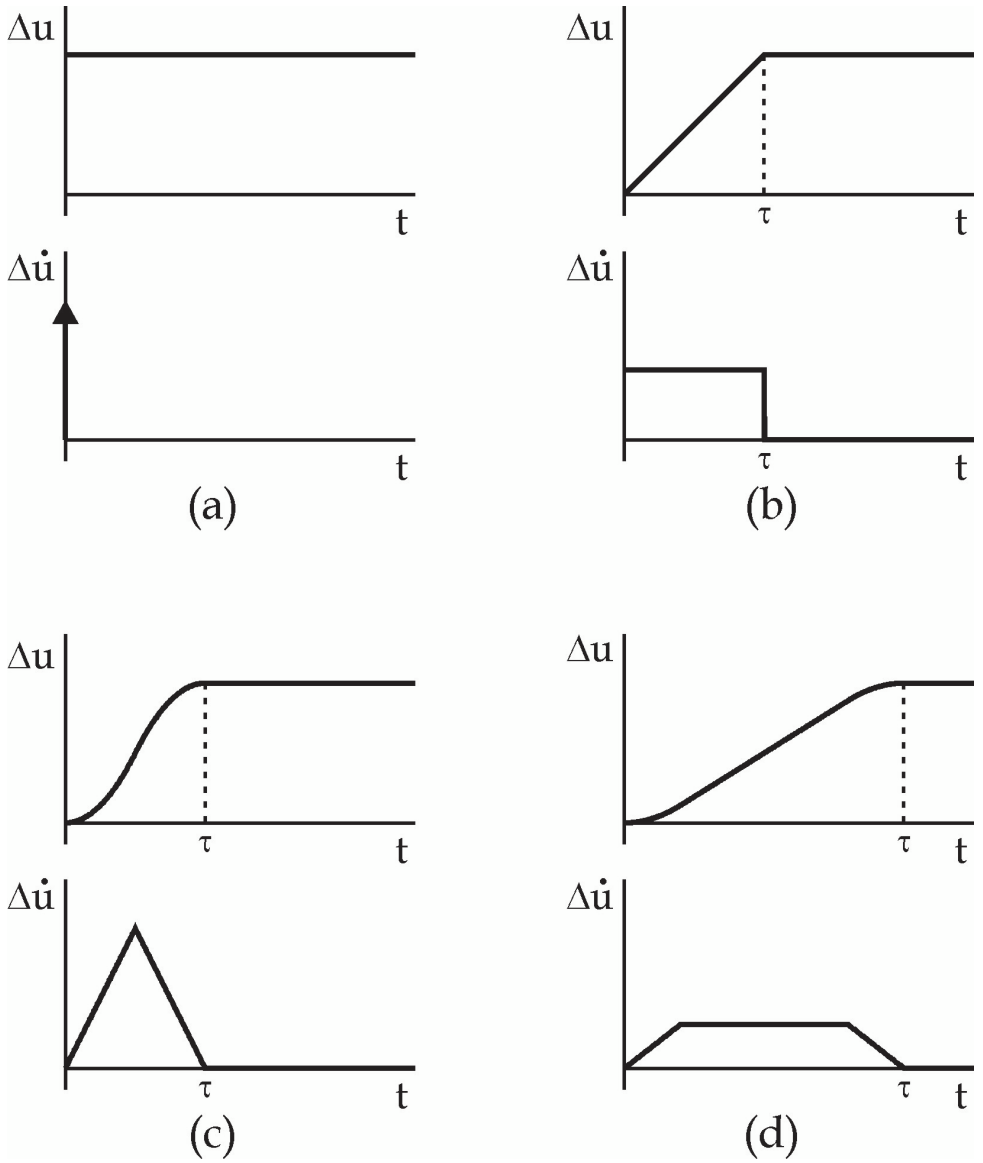

Figure 2.6: Relation between $\Delta\dot{u}$ (Source Time Function) and Δu. (a) a impulse function; (b) a rectangular function of duration τ; (c) triangular function of duration τ; and (d) a trapezoidal function of duration τ.

The STF models mentioned are simple single event sources. A complex source can be represented by an STF with several triangles (Nabelek *et al.* 1984) or trapezoids of different heights (Figure 2.7). In this way it is possible to represent STF characterized by accelerations ($\Delta\ddot{u} > 0$), deceleration ($\Delta\ddot{u} < 0$) and stops ($\Delta\ddot{u} = 0$).

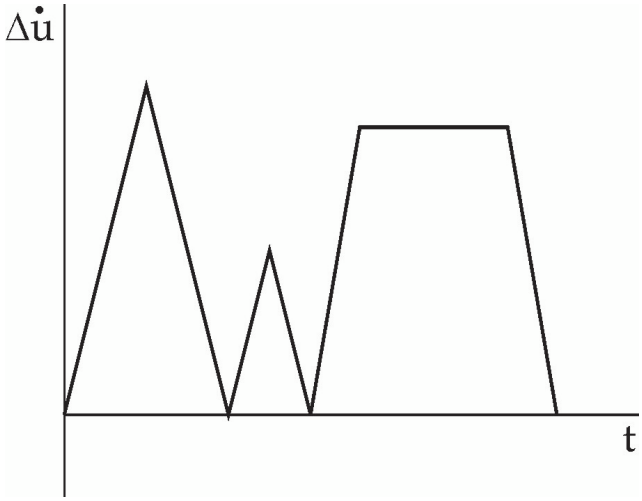

Figura 2.7: The Source Time Function ($\Delta\dot{u}$) for a complex source composed by different events.

2.11 Elastostatics

In the previous sections we studied the seismic source problems in elasto-dynamic and consequently how to define the displacement field at a given site, associated with the seismic wave propagation. In these sections instead we want to study the earthquake effect in terms of static displacement field generated in the surrounding areas, and which can be acquired through different techniques. The main methods of recording these fields are by satellites, like the SAR (Synthetic Aperture Radar) and GPS (Global Position System).

Now we want to find the static displacement **u** at point P in an isotropic, infinite, homogeneous elastic medium, due to a force at point *O*. Our medium is characterized by density ρ and elastic constants λ and μ.

We define the point force **F** by

2.55

$$\boldsymbol{F} = \lim_{\delta V \to 0} \rho \boldsymbol{f} \delta V$$

where f is the force per unit mass, $\rho \boldsymbol{f}$ is the body force per unit volume, and δV is a small volume element being acted on. We introduce the 3-dimensional delta function $\delta(r)$

2.56

$$\delta(r) = \begin{cases} 0 & r \neq 0 \\ \int_V \delta(r) dV = 1 \end{cases}$$

Using the Gauss theorem we can find that

1.57

$$\delta(r) = \frac{-1}{4\pi} \nabla^2 \frac{1}{r}$$

which allows us to represent the delta function by spatial derivatives of the radial coordinate r^{-1}.

2.12 The Green function for a single force

As for the dynamic case will now define the static displacement associated with a point source. We now apply the mathematical representation of a point force as defined in the equation 2.56-2.57 to our elastic equations for equilibrium (1.9), with $\ddot{\boldsymbol{u}} = 0$

2.58

$$(\lambda + 2\mu)\nabla(\nabla \cdot \boldsymbol{u}) - (\mu \nabla \times \nabla \times \mathbf{u}) + \boldsymbol{F} = \rho \ddot{\boldsymbol{u}}$$

Let us have a point force **F** at the origin

2.59

$$F = \rho \boldsymbol{f} = F \boldsymbol{a} \delta(r) = -F \nabla^2 \left(\frac{\boldsymbol{a}}{4\pi r} \right)$$

$$= -F \left[\nabla \left(\nabla \cdot \frac{\boldsymbol{a}}{4\pi r} \right) - \nabla \times \nabla \times \left(\frac{\boldsymbol{a}}{4\pi r} \right) \right]$$

where **a** is a unit vector in the direction of the force. To define the previous equation we used the vector identity (2.8). The equation of equilibrium becomes

2.60

$$-F\nabla^2\left(\frac{\boldsymbol{a}}{4\pi r}\right) = -F\left[\nabla\left(\nabla\cdot\frac{\boldsymbol{a}}{4\pi r}\right) - \nabla\times\nabla\times\left(\frac{\boldsymbol{a}}{4\pi r}\right)\right]$$
$$= (\lambda+2\mu)\nabla(\nabla\cdot\boldsymbol{u}) - (\mu\nabla\times\nabla\times\mathbf{u}) +$$

We are searching for a solution of the following form

2.61

$$\boldsymbol{u} = \nabla(\nabla\cdot\boldsymbol{A_P}) - \nabla\times\nabla\times\boldsymbol{A_S} \qquad \text{where}$$
$$\begin{cases}\nabla\cdot\boldsymbol{A_P} = \mathbf{0} & \therefore \boldsymbol{\nabla^2 A_P} = \nabla(\nabla\cdot\boldsymbol{A_P})\\ \nabla\cdot\boldsymbol{A_S} = \mathbf{0} & \therefore \boldsymbol{\nabla^2 A_S} = -\nabla\times\nabla\times\boldsymbol{A_S}\end{cases}$$

based on the idea that any displacement field can be represented by a sum of solenoidal and irrotational fields. Substitution of this solution leads to

2.62

$$\nabla\left\{\nabla\cdot\left[\frac{-F\boldsymbol{a}}{4\pi r} + (\lambda+2\mu)\nabla^2\boldsymbol{A}_P\right]\right\} + \nabla\times\nabla\times\left(\frac{F\boldsymbol{a}}{4\pi r} - \mu\nabla^2\boldsymbol{A}_S\right) = 0$$

which can be satisfied by having

2.63

$$(\lambda+2\mu)\nabla^2\boldsymbol{A}_P = \frac{F\boldsymbol{a}}{4\pi r}$$
$$\mu\nabla^2\boldsymbol{A}_S = \frac{F\boldsymbol{a}}{4\pi r}$$

If we now represent $\boldsymbol{A}_P = A_P\boldsymbol{a}$ and $\boldsymbol{A}_S = A_S\boldsymbol{a}$, we get the Poisson equations

2.64

$$\nabla^2 \boldsymbol{A}_P = \frac{F}{4\pi(\lambda + 2\mu)r}$$

$$\nabla^2 \boldsymbol{A}_S = \frac{F\boldsymbol{a}}{4\pi r\mu}$$

Since $\nabla^2 r = {}^2/_r$, we can integrate these to have

2.65

$$\boldsymbol{A}_P = \frac{Fr}{8\pi(\lambda + 2\mu)}$$

$$\boldsymbol{A}_S = \frac{Fr}{8\pi\mu}$$

These solutions could be used to solve the inhomogeneous equations 2.63. We evaluate the displacements by inserting then into 2.61.

Plugging in our potentials Ap and As and expressing the vector operations with indicial notation, 2.61 and 2.65 yield the i_{th} component of displacement for a unit force (F=1) in the j_{th} direction, u_i^j:

2.66

$$u_i^j = \frac{1}{8\pi(\lambda + 2\mu)} \frac{\partial}{\partial x_i} \frac{\partial r}{\partial x_j} - \frac{1}{8\pi\mu} \frac{\partial}{\partial x_i} \frac{\partial r}{\partial x_j} + \delta_{ij} \frac{1}{8\pi\mu} \nabla^2 r$$

$$= \frac{1}{8\pi\mu} \left(\delta_{ij} \nabla^2 r - \frac{\lambda + \mu}{\lambda + 2\mu} \frac{\partial^2 r}{\partial x_i \partial x_j} \right)$$

or

2.67

$$u_i^j = \frac{1}{8\pi\mu} \left(\delta_{ij} r_{,kk} - \Gamma r_{,ij} \right)$$

where

2.68

$$\Gamma = \frac{\lambda + \mu}{\lambda + 2\mu}$$

For a Poisson solid ($\lambda \approx \mu$) we find $\Gamma \approx {}^{2}/_{3}$. We have oriented our reference system in the reference frame of the source and we compute displacements relative to this local source reference frame.

Equations 2.66 and 2.67 represent the *Somigliana tensor*. The previous tensor is symmetric, $u_i^j = u_j^i$. For a force, **F**, applied in the x_1 direction, the six independent permutations are

2.69

$$u_1^1 = \frac{F}{8\pi\mu}\left[\frac{2}{r} - \Gamma\left(\frac{1}{r} - \frac{x_1^2}{r^3}\right)\right]$$

$$u_1^2 = \frac{F}{8\pi\mu}\left(\Gamma\frac{x_1 x_2}{r^3}\right)$$

$$u_1^3 = \frac{F}{8\pi\mu}\left(\Gamma\frac{x_1 x_3}{r^3}\right)$$

$$u_2^2 = \frac{F}{8\pi\mu}\left[\frac{2}{r} - \Gamma\left(\frac{1}{r} - \frac{x_2^2}{r^3}\right)\right]$$

$$u_2^3 = \frac{F}{8\pi\mu}\left(\Gamma\frac{x_2 x_3}{r^3}\right)$$

$$u_3^3 = \frac{F}{8\pi\mu}\left[\frac{2}{r} - \Gamma\left(\frac{1}{r} - \frac{x_3^2}{r^3}\right)\right]$$

2.13 Three-dimensional models of faulting, the Mansinha and Smylie solutions

The displacement field for the slip on a fault in an infinite elastic medium can be derived from the Betti reciprocal theorem as seen for the elasto-dynamics case.

That theorem relates two elastic fields in a singularity free region bounded by the surface A:

2.70

$$\iint u_i P dA_j = \iint U_i p_{ij} dA_j$$

Compared to the previous formulation (equation 1.14), for the static formulation we neglected the time-dependent terms. In the applications of this theorem to the deformation produced by slip on a fault, the elastic field (u_i,p_{ij}) is produced by the slip and the other field is taken as produced by a delta-function stress applied at Q in the direction of the x_k axis. This stress produces the elastic fields at M given by the equation 1.66 and by

2.71

$$P_{ij}^k = \lambda \delta_{ij} \frac{\partial U_m^k}{\partial x_m} + \mu \left(\frac{\partial U_i^k}{\partial x_j} + \frac{\partial U_j^k}{\partial x_i} \right)$$

In the previous formulation the superscript k index, added to U_i and P_{ij}, identifies the direction of the force. To avoid singularities within the surface A in equation 2.70, small volumes surrounding both Q and the fault surface must be excluded. This introduces two new internal surfaces, a sphere A_1 about Q and the flat surface Σ about the fault area.

Thus, the surface A is now broken into three closed surfaces A_0, A_1 and Σ, which are shown schematically in figure 2.8.

In the limit as the radius of $A_1 \longrightarrow 0$, the integration over A1 in equation 2.70 contributes $u_i(Q)$ on the left-hand side and nothing on the right-hand side. As the surface Σ is shrunk down so that it fits the fault surface quite closely, the contribution from the right-hand side of eq. 2.70 will vanish and that from the left-hand side will be $\iint \Delta u_i P_{ij} d\Sigma_j^+$. Here the surface Σ has been divided into two

surfaces Σ^+ and Σ^- representing the two sides of the fault. Then Δu_i $(= u_i^+ - u_i^-)$ is the discontinuity in displacement (i.e. slip) in crossing the fault surface.

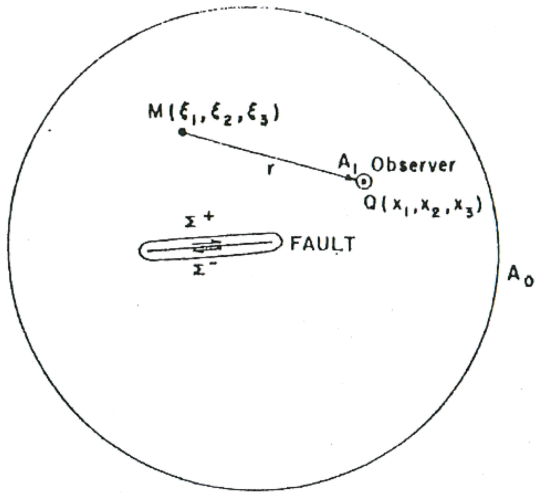

Figura 2.8: The surface involved in the application of the reciprocal theorem.

Note that the integration is over only Σ^+ not Σ. Finally, if the outer surface A_0 is allowed to recede to infinity, it can be shown for a finite slipped area that integration over A_0 does not contribute to eq 2.70. Thus, we arrive at the Volterra formula

1.72

$$u_k(Q) = \iint \Delta u_i(M) P_{ij}^k(M, Q) d\Sigma_j^+(M)$$

where the positive direction of Σ^+ is taken along the outward normal from Σ. For the particular case where the fault may be modelled as a simple dislocation loop,

Δu_i can be replaced by the Burgers vector and removed from the integral.
The displacement field generated by slip on a small element of a fault can be shown to be the same that is generated by the application of a double-couple force system at the fault element. This equivalence is shown in figure 2.9.

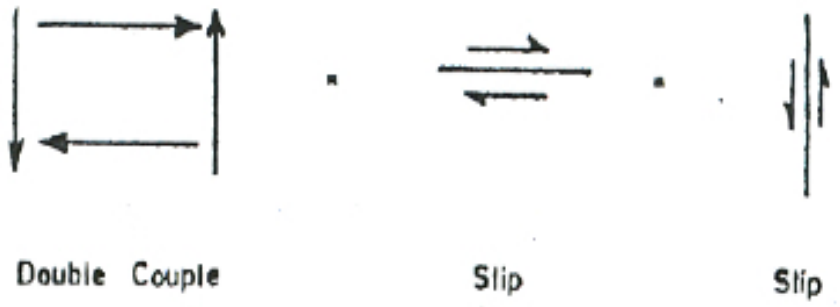

Figure 2.9: Equivalence of a double-couple force system to slip either of two orthogonal surface elements.

Mansinha and Smylie have given closed analytical expression for the displacement fields for a rectangular loop, two sides of which are parallel to the free surface (fig. 2.10). They have assumed that the elastic constants μ and λ are equal. The dip θ for the fault model is arbitrary.
The Burges vector b must lie in the plane of the dislocation loop but may be either parallel to (strike slip) or perpendicular (dip slip) to the strike of the fault plane, obviously a combination (oblique slip) of strike and dip may be generated by superposition.

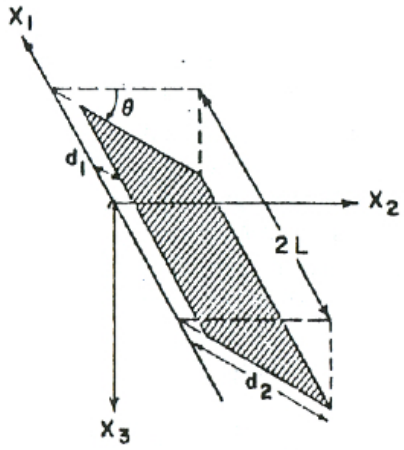

Figure 2.10: Coordinate system used to describe a three-dimensional fault model in a half space. The plane x_3=0 is a free surface, and the shaded rectangle represents the fault surface.

Figure 2.4 shows the coordinates system used by Mansinha and Smylie for their solutions. The length of the fault is 2L and down-dip width d_2 - d_1. The point at which the displacement is studied is x_1, x_2, x_3 and the integration variables on the fault are ξ_1, ξ_2, ξ_3. In our results we used some abbreviations ss done by Mansinha and Smylie:

2.73

$$\xi = \xi_2 \cos\theta + \xi_3 \sin\theta$$

$$R^2 = (x_1 - \xi_1)^2 + (x_2 - \xi_2)^2 + (x_3 - \xi_3)^2$$

$$Q^2 = (x_1 - \xi_1)^2 + (x_2 - \xi_2)^2 + (x_3 + \xi_3)^2$$

$$r_2 = x_2 \sin\theta - x_3 \cos\theta, \quad r_3 = x_2 \cos\theta + x_3 \sin\theta,$$

$$q_2 = x_2 \sin\theta + x_3 \cos\theta, \quad q_3 = -x_2 \cos\theta + x_3 \sin\theta,$$

$$h^2 = Q^2 - (x_1 - \xi_1)^2, \quad k^2 = (x_1 - \xi_1)^2 + q_2^2,$$

The integrals to be evaluated are of the form

2.74

$$u_i = \int_{d_1}^{d_2} \int_{-L}^{L} [\quad] d\xi_1 \, d\xi$$

The results of the integration are given in indefinite form and must be evaluated at the limits of integration indicated above. For $0 < \theta < 90^o$, the direction of the Burges vector *b* is specified by the movement and the normal dip-slip movements are associated with positive *b*.

For strike-slip displacement (*b* parallel to x_1):

2.75

$$12\pi \frac{u_1}{b}$$

$$= (x_1 - \xi_1)\left[\frac{2r_2}{R(R + r_3 - \xi)} - \frac{4q_2 - 2x_3 \cos\theta}{Q(Q + q_3 + \xi)} - \frac{3\tan\theta}{Q + q_3 + \xi_3} + \frac{4q_2 x_3 \sin\theta}{Q^3}\right.$$

$$\left. - 4q_2 q_3 x_3 \sin\theta \frac{(2Q + q_3 + \xi)}{Q^3 (Q + q_3 + \xi)^3}\right]$$

$$- 6\tan^2\theta \tan^{-1}\left[\frac{(k - q_2\cos\theta)(Q - k) + (q_3 + \xi)k\sin\theta}{(x_1 - \xi_1)(q_3 + \xi)\cos\theta}\right]$$

$$+ 3\tan^{-1}\frac{(x_1 - \xi_1)(r_3 - \xi)}{r_2 R} - 3\tan^{-1}\frac{(x_1 - \xi_1)(q_3 - \xi)}{q_2 Q};$$

$$12\pi\frac{u_2}{b}$$
$$= \sin\theta\,[3\tan\theta\sec\theta\ln(Q+q_3+\xi_3) - \ln(R+r_3-\xi)$$
$$-(1+3\tan^2\theta)\ln(Q+q_3+\xi)] + \frac{2r_2\cos\theta}{R}$$
$$-2\sin\theta\frac{2x_3(q_2\cos\theta - q_3\sin\theta) + q_2(q_2+x_2\sin\theta)}{Q(Q+q_3+\xi)} - 3\tan\theta\frac{(x_2-\xi_2)}{Q+q_3+\xi_3}$$
$$+2\frac{(q_2\cos\theta - q_3\sin\theta - x_3\sin^2\theta)}{Q} + 4q_2x_3\sin\theta\frac{(x_2-\xi_2)+q_3\cos\theta}{Q^3}$$
$$-4q_2^2q_3x_3\sin^2\theta\frac{2Q+q_3+\xi}{Q^3(Q+q_3+\xi)^2};$$

$$12\pi\frac{u_3}{b}$$
$$= \cos\theta\,[\ln(R+r_3-\xi) + (1+3\tan^2\theta)\ln(Q+q_3+\xi)$$
$$-3\tan\theta\sec\theta\ln(Q+x_3+\xi_3)] + \frac{2r_2\sin\theta}{R} + 2\sin\theta\frac{(q_2+x_2\sin\theta)}{Q}$$
$$-\frac{2r_2^2\cos\theta}{R(R+r_3-\xi)} + \frac{4q_2x_3\sin^2\theta - 2(q_2+x_2\sin\theta)(x_3+q_3\sin\theta)}{Q(Q+q_3+\xi)}$$
$$+4q_2x_3\sin\theta\frac{(x_3-\xi_3)+q_3\sin\theta}{Q^3} - 4q_2^2q_3x_3\cos\theta\sin\theta\frac{2Q+q_3+\xi}{Q^3(Q+q_3+\xi)^2};$$

For dip-slip displacement (b down dip)

2.76

$$12\pi\frac{u_1}{b}$$

$$= (x_2-\xi_2)\sin\theta\left[\frac{2}{R}+\frac{4}{Q}-4\frac{\xi_3 x_3}{Q^3}-\frac{3}{Q+q_3+\xi_3}\right]$$

$$-\cos\theta\left[3\ln(Q+q_3+\xi_3)+2\frac{(x_3-\xi_3)}{R}+4\frac{(x_3-\xi_3)}{Q}+4\frac{\xi_3 x_3(x_3+\xi_3)}{Q^3}\right]$$

$$+\frac{3}{\cos\theta}[\ln(Q+x_3+\xi_3)-\sin\theta\ln(Q+q_3+\xi)]$$

$$+6x_3\left[\frac{\cos\theta}{Q}-\frac{q_2\sin\theta}{Q(Q+x_3+\xi_3)}\right];$$

$$12\pi\frac{u_2}{b}$$

$$= \sin\theta\left[-\ln(R+x_1-\xi_1)\right.$$

$$+\ln(Q+x_1-\xi_1)+\frac{4\xi_3 x_3}{Q(Q+x_1-\xi_1)}+\frac{3(x_1-\xi_1)}{Q+x_3+\xi_3}$$

$$\left.+(x_2-\xi_2)^2\left\{\frac{2}{R(R+x_1-\xi_1)}+\frac{4}{Q(Q+x_1-\xi_1)}-4\xi_3 x_3\left(\frac{(2Q+x_1-\xi_1)}{Q^3(Q+x_1-\xi_1)^2}\right)\right\}\right]$$

$$-\cos\theta\left[(x_2-\xi_2)\left\{\frac{2(x_3-\xi_3)}{R(R+x_1-\xi_1)}+\frac{4(x_3-\xi_3)}{Q(Q+x_1-\xi_1)}\right.\right.$$

$$\left.+4\xi_3 x_3(x_3+\xi_3)\left(\frac{(2Q+x_1-\xi_1)}{Q^3(Q+x_1-\xi_1)^2}\right)\right\}$$

$$+6\tan^{-1}\left\{\frac{(x_1-\xi_1)(x_2-\xi_2)}{(h+x_3+\xi_3)(Q+h)}\right\}$$

$$\left.-3\tan^{-1}\left\{\frac{(x_1-\xi_1)(r_3-\xi)}{r_2 R}\right\}+6\tan^{-1}\left\{\frac{(x_1-\xi_1)(q_3-\xi)}{q_2 Q}\right\}\right]$$

$$+6\left[\frac{1}{\cos\theta}\tan^{-1}\left\{\frac{(k-q_2\cos\theta)(Q-k)+(q_3+\xi)k\sin\theta}{(x_1-\xi_1)(q_3+\xi)\cos\theta}\right\}\right.$$

$$\left.+x_3\left\{\frac{(\sin^2\theta-\cos^2\theta)(q_3+\xi)+2q_2\cos\theta\sin\theta}{Q(Q+x_1-\xi_1)}+\frac{(x_1-\xi_1)\sin^2\theta}{Q(Q+q_3+\xi)}\right\}\right];$$

$$12\pi\frac{u_3}{b}$$

$$= \sin\theta\left[(x_2-\xi_2)\left\{\frac{2(x_3-\xi_3)}{R(R+x_1-\xi_1)}+\frac{4(x_3-\xi_3)}{Q(Q+x_1-\xi_1)}\right.\right.$$

$$\left.-4\xi_3x_3(x_3+\xi_3)\left(\frac{(2Q+x_1-\xi_1)}{Q^3(Q+x_1-\xi_1)^2}\right)\right\}-6\tan^{-1}\left\{\frac{(x_1-\xi_1)(x_2-\xi_2)}{(h+x_3+\xi_3)(Q+h)}\right\}$$

$$+3\tan^{-1}\left\{\frac{(x_1-\xi_1)(r_3-\xi)}{r_2R}\right\}-6\tan^{-1}\left\{\frac{(x_1-\xi_1)(q_3-\xi)}{q_2Q}\right\}\Bigg]$$

$$+\cos\theta\left[\ln(R+x_1-\xi_1)\right.$$

$$-\ln(Q+x_1-\xi_1)-2\frac{(x_3-\xi_3)^2}{R(R+x_1-\xi_1)}-4\frac{(x_3-\xi_3)^2-\xi_3x_3}{Q(Q+x_1-\xi_1)}$$

$$\left.-4\xi_3x_3(x_3-\xi_3)^2\left(\frac{(2Q+x_1-\xi_1)}{Q^3(Q+x_1-\xi_1)^2}\right)\right]$$

$$+6x_3\left[\cos\theta\sin\theta\left\{\frac{2(q_3+\xi)}{Q(Q+x_1-\xi_1)}+\frac{x_1-\xi_1}{Q(Q+q_3+\xi)}\right\}-q_2\frac{(\sin^2\theta-\cos^2\theta)}{Q(Q+x_1-\xi_1)}\right].$$

Because 0/0 forms occur in the limit $\theta \longrightarrow 90^o$, some care must be taken in evaluating the foregoing equations for vertical faults. For this special case the following expressions given by Mansinha and Smylie are convenient:

For strike-slip faults ($\theta = 90^o$)

2.77

$$12\pi\frac{u_1}{b}$$

$$= x_2(x_1-\xi_1)\left[\frac{2}{R(R+x_3-\xi_3)}-\frac{5Q+8\xi_3}{2Q(Q+x_3+\xi_3)^2}+\frac{4\xi_3x_3(2Q+x_3+\xi_3)}{Q^3(Q+x_3-\xi_3)^2}\right]$$

$$+3\tan^{-1}\left[\frac{(x_1-\xi_1)(x_3-\xi_3)}{Rx_2}\right]-3\tan^{-1}\left[\frac{(x_1-\xi_1)(x_3+\xi_3)}{Qx_2}\right];$$

$$12\pi\frac{u_2}{b}$$

$$= -\ln(R + x_3 - \xi_3)$$

$$+\frac{1}{2}\ln(Q + x_3 + \xi_3) - \frac{4\xi_3 x_3}{Q(Q + x_3 + \xi_3)} + \frac{5x_3 - 3\xi_3}{2(Q + x_3 + \xi_3)}$$

$$+ x_2^2\left[\frac{2}{R(R + x_3 - \xi_3)} - \frac{5Q + 8\xi_3}{2Q(Q + x_3 + \xi_3)^2} + 4\xi_3 x_3\left(\frac{(2Q + x_3 + \xi_3)}{Q^3(Q + x_3 + \xi_3)^2}\right)\right];$$

$$12\pi\frac{u_3}{b} = x_2\left[\frac{2}{R} - \frac{2}{Q} + 4\frac{\xi_3 x_3}{Q^3} + \frac{3}{Q + x_3 + \xi_3} + \frac{2(x_3 + 3\xi_3)}{Q(Q + x_3 + \xi_3)}\right];$$

and dip-slip faults ($\theta = 90^o$)

1.78

$$12\pi\frac{u_1}{b} = x_2\left[\frac{2}{R} + \frac{4}{Q} - 4\frac{\xi_3 x_3}{Q^3} - \frac{6x_3}{Q(Q + x_3 + \xi_3)}\right];$$

$$12\pi\frac{u_2}{b}$$

$$= -\ln(R + x_1 - \xi_1)$$

$$+\ln(Q + x_1 - \xi_1) - \frac{6x_3^2 + 10\xi_3 x_3}{Q(Q + x_3 + \xi_3)} + \frac{6x_3(x_1 - \xi_1)}{Q(Q + x_3 + \xi_3)}$$

$$+ x_2^2\left[\frac{2}{R(R + x_1 - \xi_1)} - \frac{4}{Q(Q + x_1 - \xi_1)} + 4\xi_3 x_3\left(\frac{(2Q + x_1 - \xi_1)}{Q^3(Q + x_1 - \xi_1)^2}\right)\right];$$

$$12\pi\frac{u_3}{b}$$

$$= x_2\left[\frac{2(x_3 - \xi_3)}{R(R + x_1 - \xi_1)} - \frac{2(x_3 + 2\xi_3)}{Q(Q + x_1 - \xi_1)} - 4\xi_3 x_3(x_3 + \xi_3)\left(\frac{(2Q + x_1 - \xi_1)}{Q^3(Q + x_1 - \xi_1)^2}\right)\right]$$

$$+ 3\tan^{-1}\left[\frac{(x_1 - \xi_1)(x_3 - \xi_3)}{x_2 R}\right] - 3\tan^{-1}\left\{\frac{(x_1 - \xi_1)(x_3 + \xi_3)}{x_2 Q}\right\}$$

Figure 2.11 shows the displacement field on the free surface for the two different models of strike-slip on a vertical fault. In both models slip is assumed to extend to the free surface ($d_1 = 0$).

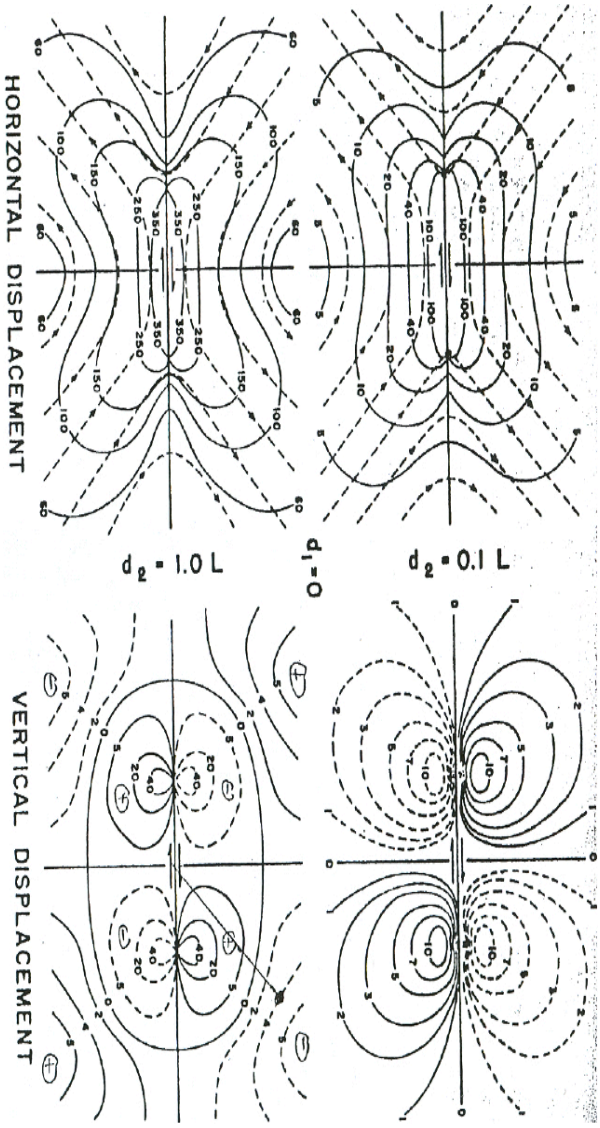

Figure 2.11: Surface deformation for two models of strike slip on a vertical fault. Horizontal displacement is on the left and vertical displacement on the right.

3 Introduction to inverse theory

3.1 Introduction

The inverse theory is a set of mathematical techniques that allows to obtain information, about property of a physical system not directly measurable from observations made on it. These observations are measures series (*data*) made on the system itself. The numerical (or statistical) knowledge of specific physical properties of a system, which in general are not directly measurable, are the objective of inverse problems. These properties are also called model parameters. We must also admit the possibility that there is some specific mathematics theory (*model*) that is able to link model parameters and data.

The inversion theory therefore, starting from data and a specific model, provides information of characterizing model parameters (figure 2.1). In contrast, the forward theory is defined as the process to predict measurement results (*data*) through a model and a set of specific conditions that relate to the problem studied

(*model parameters*).

The scientific procedure to follow for studying a physics system could be summarized as (Tarantola 1967):

- Physical system parameterization, which is to find a parameters set, able to fully characterize the system;
- Forward problem formulation, which is to define a mathematics model for the physical system, which allows to predict measurements results, once assigned model parameters;
- Inverse problem formulation, which is the model parameters determination through the data.

The first and second points of this formulation were described in the previous chapter; in this chapter instead we are going to describe the last point.

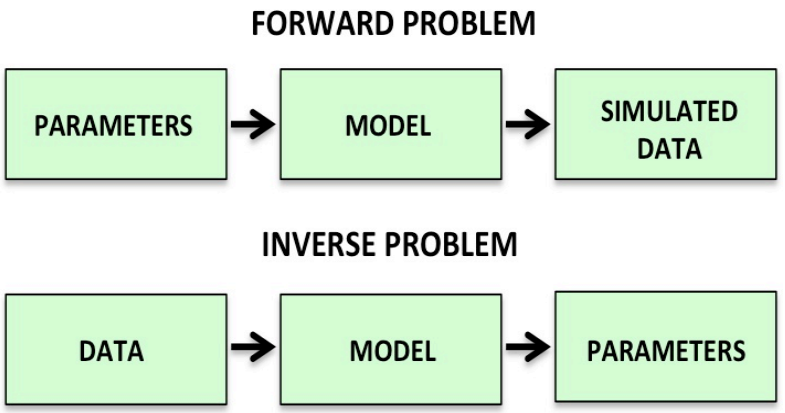

Figure 3.1: Formulation of forward and inverse problems

3.2 Inverse problems formulation

Imagine performing N measurements for a particular physical system. Results of these measures could be represented as elements of vector (**d**) with size N:

3.1

$$\boldsymbol{d^T} = (d_1, d_2 \dots \dots d_N,)$$

Similarly, the parameters of the model that characterizes the physical system could be represented as elements of a vector **m** with size M:

3.2

$$\boldsymbol{m^T} = (m_1, m \dots \dots m_M,)$$

For the inverse problems formulation, parameters, model and data have to be linked with mathematical relationships (*model*). In real situations the model could be represented by one or more implicit equations.

3.3

$$f_1(\boldsymbol{d}, \boldsymbol{m}) = 0$$
$$f_2(\boldsymbol{d}, \boldsymbol{m}) = 0$$
$$\dots.$$
$$f_L(\boldsymbol{d}, \boldsymbol{m}) = 0$$

In many cases it is possible to separate data and model parameters and so obtain, with respect to the data, L = N linear equations (in this configuration, the data could be non-linearly dependent on model parameters through a vector function **g**):

3.4

$$f(\boldsymbol{d}, \boldsymbol{m}) = 0 = \boldsymbol{d} - g(\boldsymbol{m})$$

In the simplest case, the function **g** is linear with respect to model parameters and so we have the matrix equation

3.5

$$f(\boldsymbol{d}, \boldsymbol{m}) = 0 = \boldsymbol{d} - \boldsymbol{G}\boldsymbol{m}$$

Equation 3.5 is the basis of the linear discrete inversion theory: many inverse

problems that arise from physical experience use exactly this formulation. In other cases, there are problems involving more complicated equations that could be solved by linear approximations. The matrix **G** (with N x M size) is called *kernel*. Equation 3.5, in the inversion discrete theory could be written as:

3.6

$$d_i = \sum_{j=1}^{M} G_{ij}\, m_j$$

3.3 The inverse problems solution

Generally we would expect the numerical values of the model parameters as the result of an inverse problem. Unfortunately, only in few and simple cases, an inverse problem is able to provide this type of information.

Typically we make compromises between the type of information that we want and those that actually can be obtained from a given data set. These compromises lead to inverse problems solutions that are somehow more abstract than the simple estimation of the model parameters. In other words, it is necessary to identify the most important features of a solution and do what is possible to accentuate them.

The most immediate solution of an inverse problem is the $\mathbf{m}^{est}$ estimation of the model parameters. Often, however, the simple estimation of the model parameters is not able to give information on how the solution is affected by errors present on the data, and so it is not possible to quantify the quality solution. One solution for this problem is to introduce constraints that can be both absolute and probabilistic.

3.4 The linear invers problems solution

The easiest way to solve the linear inverse problem (equation 3.5) is based on the measure of "distance" between observed and predicted (on the basis of a given model $\mathbf{m}^{est}$) data

3.7

$$\boldsymbol{d}^{pre} = \boldsymbol{G}\boldsymbol{m}^{est}$$

choosing the model for which the predicted data are very similar to those observed. For any observation we define a "prediction error" (*misfit*)

3.8

$$e_{i=}d_i^{obs} - d_i^{pre}$$

and the best fit model is that defined by the parameters that provide the total error E, as small as possible. We could define E, for example, as

3.9

$$E = \sum_{i=1}^{N} e_i^2$$

We explicitly note that the total error E is the square Euclidean length of the vector $\boldsymbol{e^T} = (e_1, e_2 \ldots . e_N)$. If we minimize the expression 3.9, the method is also called *least squares method*.

The Euclidean length however is only one of the possibilities to quantify this vector dimension (*norm*). The norm definitions commonly used are based on the sum of some degree of the vector elements (L_1 norm, L_2 norm ecc.).

Generally norm with high degree give higher weight to the larger elements of **e**: indeed if we consider the limit case $n \to \infty$ we give only to the large element of **e**, a weight different from zero. The least squares method makes use of L_2 norm.

We derive now the least-squares linear inverse problem solution. Starting from the definition of E (equation 3.9), we have

3.10

$$E = \boldsymbol{e}^T\boldsymbol{e} = (\boldsymbol{d} - \boldsymbol{G}\boldsymbol{m}^{\boldsymbol{est}})^T(\boldsymbol{d} - \boldsymbol{G}\boldsymbol{m}^{\boldsymbol{est}}) =$$

$$=\sum_{i=1}^{N}\left[d_i-\sum_{j=1}^{M}G_{ij}m_j^{est}\right]\left[d_i-\sum_{k=1}^{M}G_{ik}m_k^{est}\right]=$$

$$=\sum_{j=1}^{M}\sum_{k=1}^{M}m_j^{est}\,m_k^{est}\sum_{i=1}^{N}G_{ij}\,G_{ik}-2\sum_{j=1}^{M}m_j^{est}\sum_{i=1}^{N}G_{ij}d_i+\sum_{i=1}^{N}d_id_i$$

To find the minimum E, we derive its expression for $\mathbf{m}_q$ and after we equalize the result to zero, obtaining

3.11

$$\frac{\partial E}{\partial m_q}=2\sum_{k=1}^{M}m_k^{est}\sum_{i=1}^{N}G_{iq}G_{ik}-2\sum_{i=1}^{N}G_{iq}d_i=0$$

which in matrix notation can be written as

3.12

$$\boldsymbol{G^T G m^{est}-G^T d=0}$$

Assuming that the $\mathbf{G}^T\mathbf{G}$ inverse matrix exists, the solution of the equation 3.12 is given by

3.13

$$\boldsymbol{m^{est}=[G^T G]^{-1}G^T d}$$

which is the solution to the least-squares linear inverse problem.

3.5 Generalized inverse and resolution matrix

Most solutions of linear inverse problems present a linear dependence on the data that can be expressed as

3.14

$$\boldsymbol{m^{est}=Md+v}$$

being **M** and **v** a matrix and vector, independent from the data from the data (**d**), respectively. For example, referring to 3.13, $\boldsymbol{M} = [\boldsymbol{G^T G}]^{-1}\boldsymbol{G^T}$ and **v** is the null vector. We now move the attention from $\boldsymbol{m}^{est}$ to the operator matrix **M**. Since the matrix **M** resolves the inverse problem $\boldsymbol{Gm} = \boldsymbol{d}$, it is often called generalized inverse and denoted by $\boldsymbol{G}^{-g}$ so that the solution to the inverse problem, given by equation 3.5, is expressed as

3.15

$$\boldsymbol{m}^{est} = \boldsymbol{G}^{-g}\boldsymbol{d}$$

We explicitly note that $\mathbf{G}^{-g}$ is not the **G** inverse matrix in the usual sense, that it is not necessarily square and that neither $\mathbf{G}^{-g}\mathbf{G}$ nor $\mathbf{G}\mathbf{G}^{-g}$ are equal to the identity matrix ($\Im$).

Suppose now we have found a generalized inverse $\mathbf{G}^{-g}$ that solves the inverse problem 3.5. It is possible to know "a posteriori" how the estimated model parameters is able to reproduce the data. We have

3.16

$$\boldsymbol{d}^{pre} = \boldsymbol{G}\boldsymbol{m}^{est} = \boldsymbol{G}[\boldsymbol{G}^{-g}\boldsymbol{d}^{obs}] = [\boldsymbol{G}\boldsymbol{G}^{-g}]\boldsymbol{d}^{obs} = \boldsymbol{R}\boldsymbol{d}^{obs}$$

The square matrix of N x N size denoted by **R**, is also called resolution data matrix (Menke, 1989) and describes in some way the quality data prediction. If $\mathbf{R} = \Im$, then $\mathbf{d}^{pre} = \mathbf{d}^{obs}$ and the prediction error is zero. Consider the i_{th} row of **R**, if all the row elements are equal to zero except the i_{th} (that is equal to one), then the data is accurately predicted. On the other hand, suppose that the i_{th} row of **R** contains more elements different from zero:

3.17

$$[\ldots 0\ 0\ N_{i-1}\ N_i\ N_{i+1}\ \ 0\ 0\ \ldots]$$

In this case, d_i^{pre}, is equal to

3.18

$$d_i^{pre} = \sum_{j=1}^{N} N_{ij} d_j^{obs} = A d_{i-2} + B d_{i-1} + C d_i + D d_{i+1}$$

and then the predicted value is a weighted mean of the near four values. If the true datum little depends on the auxiliaries' coefficients, then a weighted average produces an estimate reasonably near to observed value. Finally, the **R** matrix describes how well the data can be independently predicted or, in other words, solved.

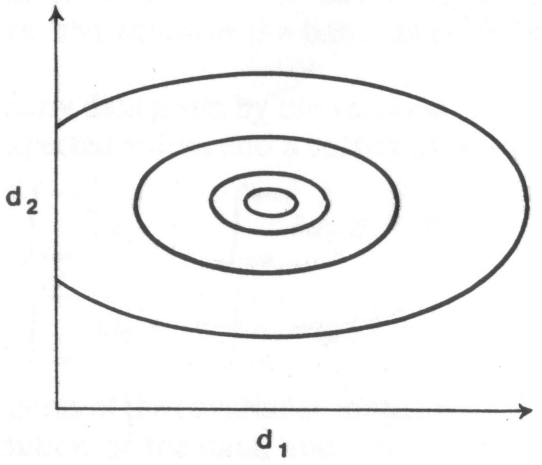

Figure 3.2: The probability distribution $P(d_1,d_2)$ is represented with isoline of equal value as function f d_1 and d_2. These data, therefore, are not related, indeed large values of d_2 could correspond to small or big values of d_1.

Of course the same reasoning could be applied to the model parameters. To analyze this case, we suppose that a set of $\mathbf{m}^{true}$ parameters exists that identifies the true model (unknown) and so $\mathbf{G}\mathbf{m}^{true} = \mathbf{d}^{obs}$. Then

3.19

$$\boldsymbol{m}^{est} = \boldsymbol{G}^{-g}\boldsymbol{d}^{obs} = \boldsymbol{G}^{-g}[\boldsymbol{G}\boldsymbol{m}^{true}] = [\boldsymbol{G}^{-g}\boldsymbol{G}]\boldsymbol{m}^{true} = \boldsymbol{R}_{\boldsymbol{m}}\boldsymbol{m}^{true}$$

The square matrix of size M x M that we have denoted by $\mathbf{R_m}$ is the said model resolution matrix (Menke, 1989). If $\mathbf{R_m} = \Im$, then each model parameter is exactly determined.

3.6 Correlation and covariance

During experiments the collected data number could be high, so it is necessary to quantify the probability that a set of random variables assume the corresponding values of the measured results.

The joint probability distribution $\mathbf{P(d)}$ provides the probability that the first collected data is in a neighborhood of d_1, the second is in a neighborhood of d_2, and so on. If the data are independent, this joint probability distribution is the single individual probability distributions product (Figure 2.2):

3.20

$$\boldsymbol{P(d)} = P(d_1)xP(d_2)x \dots P(d_N)$$

However, in same case, measurement results are themselves correlated: high d_1 values corresponding to high or small (or anyway particular) d_2 value (Figure 3.3). It is necessary in this case that the probability joint distribution accounts for this correlation.

For a given joint probability distribution, we can check the goodness, with respect to the studied problem, choosing a suitable function that divides the plane (d1, d2) into four quadrants, with alternating sign, with centre on the centre distribution (Figure 3.4).

If we multiply this function for the probability distribution and then integrate the entire plane, the result will be zero for not related distribution (since they occupy in the same way the four quadrants); differently, related distributions will provide positive or negative results, since they tend to be concentrated in two opposite

quadrants (Figure 3.5).

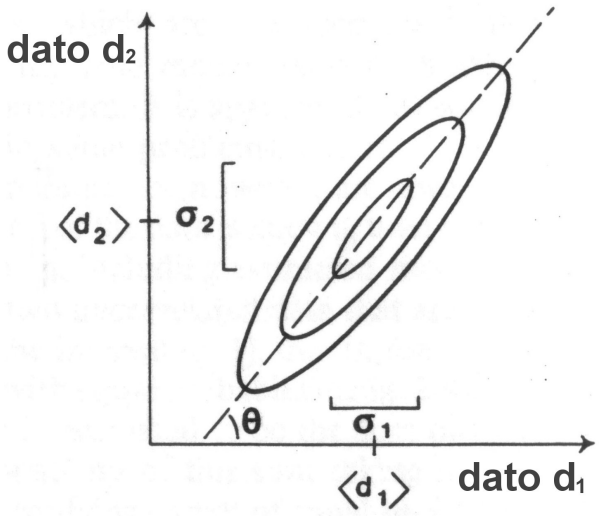

Figure 3.3: The probability distribution $P(d_1,d_2)$ is represented with isoline of equal value as function f d_1 and d_2. These data are correlated, indeed large values of d2 correspond to large values of d1. The probability distribution is characterized by mean values <d1> and <d2> and amplitude given by s1 and s2. The angle θ is a measure of the correlation and is linked to the covariance.

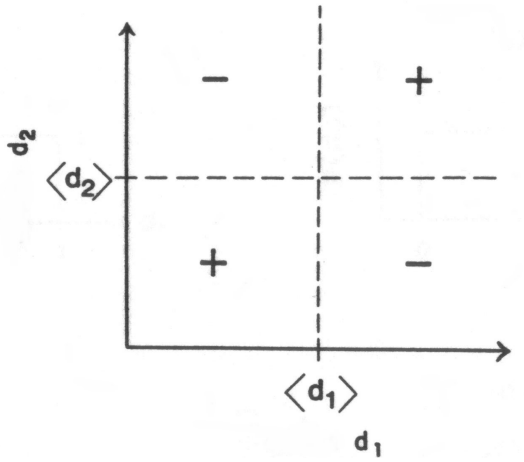

Figure 3.4: The function $(d_1-<d_1>)(d_2-<d_2>)$ separate the plane (d_1,d_2) in four quadrants with alternating signs.

If the function that we use to test the quality distribution for the joint probability is that of figure 3.4 $((d_1-< d_1 >)(d_2-< d_2 >))$, being <d> the expected value for

d, the resulting correlation measure is call covariance:

3.21

$$cov(d_1, d_2) = \int_{-\infty}^{+\infty} \partial d_1 \int_{-\infty}^{+\infty} \partial d_2 \dots \int_{-\infty}^{+\infty} \partial d_N \, (d_1 - < d_1 >)(d_2 - < d_2 >) P(d)$$

we can explicitly note that the covariance of a datum with itself is the variance. When we have a lot of data, it is convenient to define the covariance matrix

3.22

$$[cov\, \boldsymbol{d}]_{ij} = \int_{-\infty}^{+\infty} \partial d_1 \int_{-\infty}^{+\infty} \partial d_2 \dots \int_{-\infty}^{+\infty} \partial d_N \, (d_i - < d_i >)\big(d_j - < d_j >\big) P(d)$$

The diagonal elements of the covariance matrix provide a measure of the width of the data distribution while the diagonal outside elements indicate correlation degree of each data pair.

Of course the bases of the inversion theory is that data and model parameters are in relation to each other. Any method that provides a solution for an inverse problem will tend, therefore, to report data errors on the estimation of model parameters. As a result, the estimate of model parameters are themselves random variables that are described by a probability distribution $\boldsymbol{P}(\boldsymbol{m}^{est})$. Whether the real parameters are or are not random variables, depends on the examined problem. The estimate parameters are in any case random variables. If we consider a case in which model parameters have a linear dependence with data (equation 3.14), it is possible to derive some properties of the parameters probability distribution without calculatig it. In particular, the mean and covariance of such distribution are given respectively by (Menke, 1989)

3.23

$$< \boldsymbol{m} > = \boldsymbol{M} < \boldsymbol{d} > + v$$

$$[cov\ \boldsymbol{m}] = \boldsymbol{M}[cov(\boldsymbol{d})]\boldsymbol{M}^T$$

Therefore the covariance of the estimates model parameters depends on the data covariance and the way in which the error is reported by the data in the model. It is then useful to define a unitary covariance matrix that characterizes the errors amplification degree when reported in the model. If we assume that all data is uncorrelated and presents the same variance σ^2, the unitary covariance matrix unitary is given by (Menke, 1989)

3.24

$$[cov_u\ \boldsymbol{m}] = \frac{1}{\sigma^2}\boldsymbol{G}^{-g}[cov\ \boldsymbol{d}]G^{-g^T} = \boldsymbol{G}^{-g}G^{-g^T}$$

Even if the data is correlated, it is often possible to obtain some normalization of the data covariance matrix in order to define the matrix covariance as unitary (Menke, 1989)

3.25

$$[cov_u\ \boldsymbol{m}] = \boldsymbol{G}^{-g}[cov\ \boldsymbol{d}]G^{-g^T}$$

3.7 Linearized inverse method

Inverse problems are non-linear if the relationship that describes then (equation 3.5) is not linear. One of the possible ways of solving non linear inverse problems is to make them locally (i.e., in the neighborhood of a point) linear. In practice, we rewrite the equation 3.5 in the form

3.26

$$\boldsymbol{d} = \boldsymbol{G}(m_0) + \frac{\partial \boldsymbol{G}}{\partial \boldsymbol{m}}\delta \boldsymbol{m}$$

we make linear the inverse problem 2.5 in a neighborhood of $\mathbf{m}_0$ since the 3.26 can

be written as

3.27

$$\boldsymbol{d} - \boldsymbol{G}(\boldsymbol{m}_0) = \boldsymbol{A}\delta\boldsymbol{m}$$

where $A_{ij} = \frac{\partial G_i}{\partial m_j}$.

If the function **G** is analytically defined, then the matrix **A** is known exactly, otherwise it must be obtained numerically differentiating **G**. Starting from an initial model $\mathbf{m}_0$, it is therefore possible to obtain the solution $\mathbf{m}_1$ of the linearized inverse problem. Probably, the solution $\mathbf{m}_1$ will not be the exact one. It is however, possible to obtain, using $\mathbf{m}_1$ as the initial model, a new solution to the problem 3.27 that will be better than the previous one. Such a procedure is repeated iteratively until the obtained solution is sufficiently accurate.

Finally, using a linearized approach, the non-linear inverse problem is returned to a series of linear problems solved in succession.

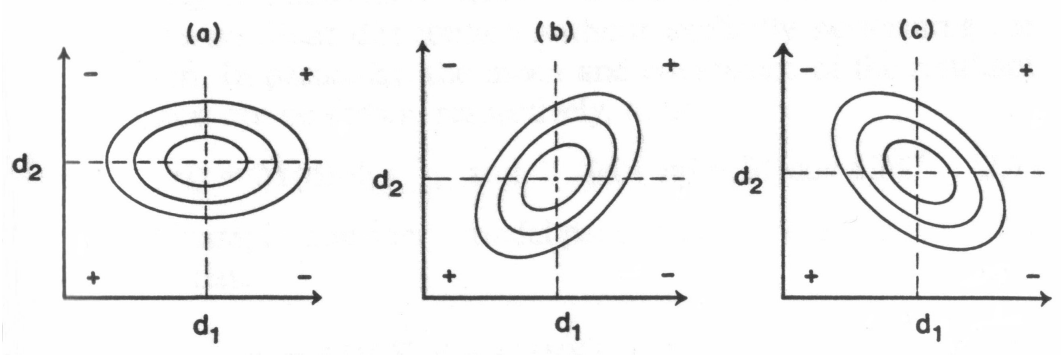

Figure 3.5: The probability distribution P(d1,d2) is represented with isolines of equal value as a function of d1 and d2 when the data are (a) unrelated, (b) positively correlated, and (c) negatively correlated.

3.8 Non-linear inverse method

If the equation 3.5 is strongly non-linear then the inverse problem solution with a linearized approach is unusable. Indeed, a strongly non-linear function is often

multimodal and, if the initial model is chosen in a neighborhood of a relative minimum, for example, the linearized solution will tend to converge towards it.
From a conceptual point of view, the non-linear inverse methods are simpler than those linearized: indeed, they are proposed to find the model that better justifies the observed data minimizing the distance between these and the theoretical ones predicted.
The cost function (*misfit*) E, defined in equation 3.9, is a measure of this gap. At the base of non-linear inverse methods we have, therefore, the optimization methods of the cost function.

3.9 Optimization method

The optimization problem in the simplest form, consists of, given a function f that depends on one or more independent variables, finding the values of the variables at which f assumes a maximum or minimum value. An extreme (i.e. a maximum or minimum point) of a given function could be global if it corresponds to the absolute maximum or minimum of the function, or local, if it is a relative maximum or minimum (figure 3.6).
The search of a global extreme of a function is often a complicated problem. Typical methods for the detection of one extreme function point are those known as *hill climbing scheme* category.
A generic example of this *hill climbing* method is illustrated in figure 3.7. We chose a starting point in the parameter space (panels A and B of Figure 3.7), then it determines the local maximum variation direction and we move for a given distance in this direction (panel C in Figure 3.7), here we estimate the new local maximum variation direction and so on until it reaches a position at which all near directions are descendent and so we finally identify the function extreme point (panel D of figure 3.7).

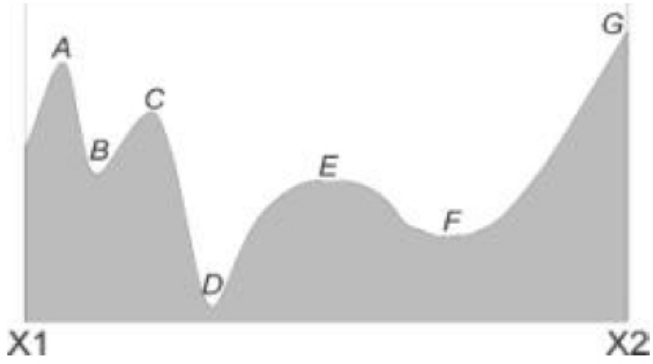

Figure 3.6: Extreme value of a function defined on an interval. The points A, C and E are local maxima, while point G is the global maximum. Points B and F are local minima while the global minimum is point D.

The *hill climbing* methods work very well if we are analyzing unimodal functions. However if we consider the case in figure 3.8, where we have an absolute maximum surrounded by different relative maxima, it is clear how the *hill climbing* methods could provide good results only if the starting point is near the absolute maximum.

Therefore it is clear that the starting point (or, generally the initial model parameters) for this kind of method can strongly influence the final result.

The *hill climbing* optimization techniques represent therefore a class of local search methods since they allow finding the extreme point function only close to the initial model. The function of Figure 3.8 instead presents typical problems for which global optimization techniques work better.

In the example of Figure 3.8 the central peak covers about 1% of the space parameters. Under these conditions, it seems clear that there is only 1% probability that a random throwing provide a good starting point, sufficiently close to the central peak in order to enable to achieve the absolute function maximum.

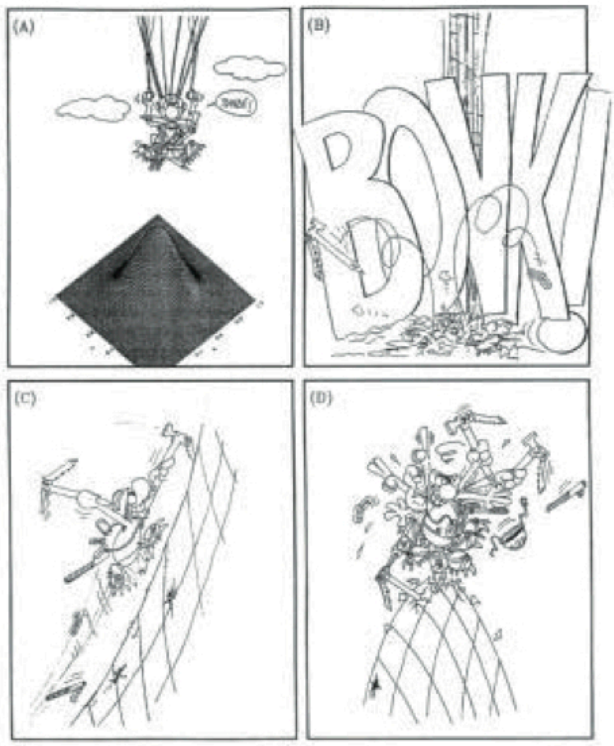

Figure 3.7: Allegory that shows the operating way of a hill climbing scheme. From a starting random point (panels A and B) is followed the maximum slope direction (panel C). We stop the exploration when the maximum is reached.

This problem introduces the *iterated hill climbing* technique: we have to restart the selected optimization method, each time with a different initial model, randomly chosen.

At the same time, it is sufficient to note the values of the model parameters corresponding to the different maximum and when we are sure that we have sampled all the space parameters, we choose the model corresponding to the maximum.

Returning to the figure 3.8 example, as mentioned above, since the central maximum covers a region of the order of 1% in the space parameters, we could

expect to locate it with a number of iterations for the optimization process that is of 10^2. If we have an optimization problem involving a high dimension of the parameter space and/or situations in which the absolute extreme covers only a small fraction of the parameter space, a local search method could need a lot of computational time.

These considerations allow us to identify what are the performances required for a global optimization method:

- Absolute performance: how accurate is the solution we get with the optimization method chosen?
- Global performance: how can you be sure that you have found the true extreme global parameter space?
- Relative performance: is the "job number" required by the method used to provide a solution?

Many optimization methods are designed to match the best possible way to the first and to the third point simultaneously. At the same time however, we may give an answer to the second point only if we have specific initial work assumptions.

In the next paragraph we are going to describe, specifically, the methods used for our work, although other methods may be encountered in the relevant literature (e.g. Downhill Simplex Neighborhood algorithm etc.).

3.10 Simulated Annealing

The simulated annealing method exploits a statistical mechanical analogy to search for the global minimum of an objective function ϕ possessing a large number of secondary minima. The algorithm simulates the process of chemical annealing in which a melted crystalline material is cooled slowly through its freezing point, thereby approximately settling into its energy ground state.

By identifying the objective function with the energy of the crystalline material and

by appropriate definition of a temperature parameter for the simulations, it is possible to simulate a "cooling" of the system to be optimized. A sufficiently slow cooling of this system will, by analogy to the chemical annealing, result in convergence to a near-optimal configuration, characterized by a near-minimal value of the objective function.Simulated annealing is based on the Metropolis-Hasting algorithm or the Gibbs sampler, and we shall therefore take a closer look at this algorithm here.

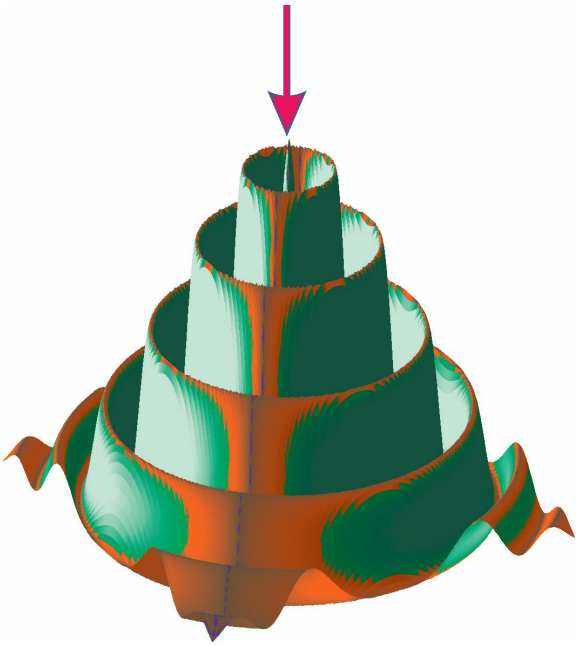

Figure 3.8: The represented function is an example of a complex optimization problem. The arrow indicates the absolute maximum.

3.10.1 The Metropolis Hasting Algorithm

The idea behind the Metropolis-Hastings algorithm is to generate samples of a probability distribution p over a high-dimensional space $\mathcal{M}$ under the special difficulty that no explicit mathematical expression exists for p.

Only an algorithm that allows us to calculate the values of **p** at a given point in the space is available. This is a typical situation in geophysics where **p** is a probability density derived from a misfit function ϕ through, for example

3.28

$$p(\boldsymbol{m}_k) = Ae^{-(-B\phi(\boldsymbol{m}_k))}$$

Where $\mathbf{m}_k$ is a model and A and B are constants. Very often $p(\mathbf{m}_k)$ can be evaluated for a particular Earth model through a very computer-intensive calculation.

A detailed description of Metropolis-Hastings algorithm is not the subject of this paper, so in this section I only describe assumptions that are at the base of this technique (for any detail we refer to Sambridge & Mosegaard 2002). For simplicity, we consider a situation where we wish to sample a probability distribution p in a discretized model space $\mathcal{M}$. Sampling from the distribution p means that the probability of visiting model **m** is proportional to $p(\mathbf{m})$. To generate a simple algorithm that samples p, we can make the following assumptions:

1. The probability of visiting a point $\mathbf{m}_i$ in model space, given that the algorithm currently is at point $\mathbf{m}_j$, depends only on $\mathbf{m}_j$ and not on previously visited points. This is the so-called *Markov* property. This property means the algorithm is completely described by a transition probability matrix $\mathbf{P}_{ij}$ whose ij_{th} component is the conditional probability of going to point $\mathbf{m}_i$, given the algorithm currently visits $\mathbf{m}_j$.
2. For all points $\mathbf{m}_j$ in $\mathcal{M}$, there is exactly N points $\mathbf{m}_i$, including $\mathbf{m}_j$ itself, for which $\mathbf{P}_{ij}$ is nonzero. If this property holds, we say that the algorithm is regular, and the set of N accessible points constitutes what we call the neighborhood $\aleph_j$ of $\mathbf{m}_j$.
3. It is possible for the algorithm to go from any point $\mathbf{m}_j$ to any other point $\mathbf{m}_i$, given enough steps. An algorithm satisfying this property is called irreducible.

The problem now is which transition probability matrix ($\mathbf{P}_{ij}$) to use. Generally there exists infinitely many such transition matrices, and so we can choose one that is simple (for more details see Sambridge and Mosegaard 2002).

3.10.2 Simulated annealing algorithm

It is an empirical fact that the process of chemical annealing, where a crystalline material is slowly cooled through its melting point, results in formation of highly ordered, low-energy crystals.

The slower the cooling, the more perfect is the crystal growth, and the lower is the lattice energy. This process can be viewed as a "physical optimization method" in which the objective function is the lattice energy E. In each step of the algorithm, thermal fluctuations in the system are simulated by randomly perturbing model parameters, and the fluctuations are controlled by a temperature parameter T.

The simulated annealing algorithm (Kirkpatrick *et al*., 1983) runs as follows: in each step random perturbations of the model parameters $\mathbf{m}_j$ of the numerical system are attempted. The new set of model parameters $\mathbf{m}_i$ is accepted if the value of the objective function E decreases.

However, if E increases, the new parameter may be accepted with probability

3.29

$$P_{accept} = e^{(-\frac{\Delta E}{T})}$$

where ΔE is the change in the objective function and T is the temperature parameter. If the new model is rejected, a new perturbation is attempted in the next move, and the above process of decision is repeated.

A close inspection of the above algorithm reveals that for constant temperature parameter T it is actually a Metropolis-Hasting algorithm designed to sample the probability distribution (Metropolis et al., 1953),

3.30

$$P_B(\boldsymbol{m}) = \frac{e^{(-\frac{E(\boldsymbol{m})}{T})}}{Z(T)}$$

which is known in statistical physics as the Gibbs-Boltzmann distribution. Here $1/Z(T)$ is normalization constant. In simulated annealing, however, the temperature parameter is gradually decreased from a high value, allowing large "thermal" fluctuations, down to zero, where only decreasing values of the objective function are allowed. For decreasing temperature T the Gibbs-Boltzmann distribution converges toward a distribution having all its probability mass in the global minimum for E.

3.11 The Genetic Algorithm

The natural selection principle states that individuals who better adapt to their environment, on average, leave behind more offspring than their less suitable colleagues.

For natural selection to lead to evolution, two more essential ingredients are required: *inheritance* (offspring must retain at least some of the features that made their parents fitter than average, otherwise evolution is effectively reset at every generation) and *variability* (at any given time individuals of varying fitness must coexist in the population, otherwise natural selection has nothing to operate on).

In nature, the information determining the growth and development of individuals is encoded as linear sequences of genes that can each assume a finite set of "values". In sexual species, when two individuals breed, complementary portions of their genetic material are passed on to their offspring and combined to define that offspring's full genetic makeup. That is the inheritance part. In the course of "preprocessing" the genetic material to be later passed on to offspring, copy

mistakes and truly random alternation of some gene values also occur occasionally. These mutations, coupled to the fact that an offspring receives complementary genes from two parents, provide the necessary source variability.

The individual that moves, feeds and mates in real space can be looked at as the outer manifestation of its defining genes. Think then of an individual- do its genes assume fitness as a function of the values? What evolution does, is to drive a gradual increase in average fitness value over several generations. It should however be clarified that the evolutionary process does not optimize, at least not in the mathematical sense.

What evolution does, is produce individuals of above-average fitness. Fundamentally, genetic algorithms are a class of search techniques that use simplified forms of the biological process of natural selection: inheritance and variability. Strictly speaking they are not optimization methods *per se*, but can be used to form the core of a class of robust and flexible methods known as *genetic algorithm-based optimizers*.

Let us consider a generic optimization problem. One is given a "model" that depends on a set of parameters **u**, and a functional relation f(**u**), which returns a measure of quality (or better, fitness) associated with the corresponding model. The optimization task usually consists in finding the vector **u*** in parameter space corresponding to the model that maximizes the fitness function f(**u**). Define now a population as a set of N_P realizations of the parameters **u**. The schematic description of the operation mode of a genetic algorithm in an optimization problem is:

1. Randomly initialize population and evaluate fitness of its members;
2. Breed selected members of current population to produce offspring population (selection based on fitness);
3. Replace current population by offspring population;
4. Evaluate fitness of new population members;

5. Repeat steps 2 to 4 until the fittest member of the current population is deemed fit enough, more "suitable" the current population.

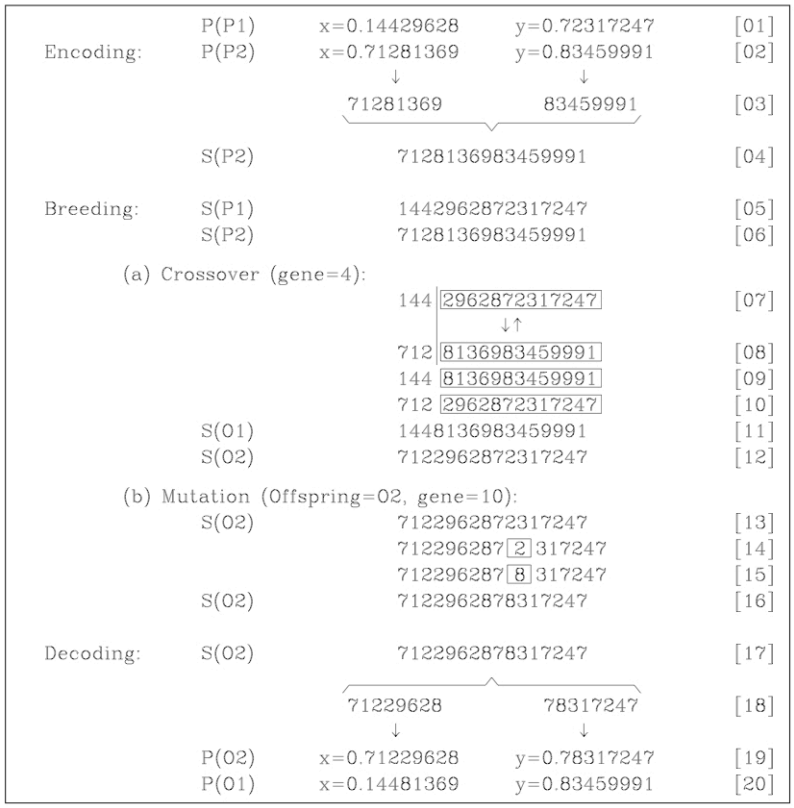

Figure 3.9: Breeding in genetic algorithms. Here the process is illustrated in the context of a 2-D maximization problem. An individual is an (x, y) point, and two such parent individuals are needed for breeding (denoted $P(P_1)$ and $P(P_2)$). The one-point crossover and one-point mutation operators act on string representations of the parents to produce offspring strings $S(O_1)$ and $S(O_2)$, which are finally decoded into two offspring (x, y) points $P(O_1)$ and $P(O_2)$.

However, the important novelty of genetic algorithms lies with step 2: breeding between the elements of the population. It is in the course of breeding that information is passed and exchanged across population members. How this information transfers, needs a more detailed discussion.

Suppose we want to determine the maximum of a function of two variables, for

example, that of figure 3.8. In this case, since the parameter space is two-dimensional, each population member is identified by a pair of coordinates (x, y) and so is "defined" by two floating point numbers. The first step is to *encode* the two floating-point numbers defining each individual selected for breeding. Here this is done simply removing the decimal point and concatenating the resulting set of simple decimal integers into a "chromosome", like the string in lines 01-06 in figure 3.9.

Breeding proper is a two-step process. The first step is *crossover*. The two strings generated by the encoding process are laid side by side, and a cutting point is randomly selected along the length of the defining strings. The string fragments located right of the cutting point are then interchanged, and spiced onto the fragments originally located left of the cutting point (lines 07-12 of figure 3.9, for a cutting point located between the third and fourth decimal digit). The second breeding step is the *mutation*. For each string produced by the crossover process, a few randomly selected digits (or better, genes), are replaced by new, randomly selected digit value (lines 13-16 of figure 3.9, for a mutation hitting the tenth digit of the second offspring string). The resulting fragments are finally decoded in two (x, y) pairs, for which the fitness is evaluated. Note that the offspring incorporates intact "chunks" of the genetic material from both parents, that is, the needed inheritance as well as the promised exchange of information between trial solutions. In any case, both the *crossover* and *mutation* operations also involve purely stochastic components, such as the choice of cutting point, site of mutation, and new value of mutated digit. This is where we get variability needed to sustain the evolutionary process. It should also be noted that the crossover and mutation operators, operating in conjunction with the encoding/decoding process (figure 3.9), preserve the total range in parameter space. This means, for example, that if the floating-point parameters defining parent solutions are restricted to the range [0.0,1.0], then the offspring solution are restricted in the same range. This is a very

important property, through which one can introduce hardwire constraints such as positivity that allows to set the constraints to, for example, non- negative solutions.
Indeed having the mutation operator act on the encoded form of the parent solution has the interesting result that offspring can differ very much or very little from their parents, depending on whether the digits affected by mutation decode into one of the leading or trailing digits of the corresponding floating-point number.
From the point of view of parameters space exploration, this implies that a genetic algorithm can carry out both wide exploration and fine-tuning in parallel.
Figure 3.10 shows the population evolution, during the search for maximum of the function of figure 3.8, on which the genetic algorithm acts.
Finally, it must be possible to calculate the function f (u) for all possible values of **u** but this feature should not be necessarily differentiable since the differentiability of the fitness function is not required by the algorithm and this, from a practical point of view, is a great advantage.
In conclusion, genetic algorithms differ from other optimization methods for the following reasons (Goldberg, 1989):

- They work on sets of coded parameters and not on the same parameters;
- They carry out research on a population of points and not on individual points;
- They use information from a fitness function without resorting its derivatives;
- They use probabilistic and non-deterministic transition rules.

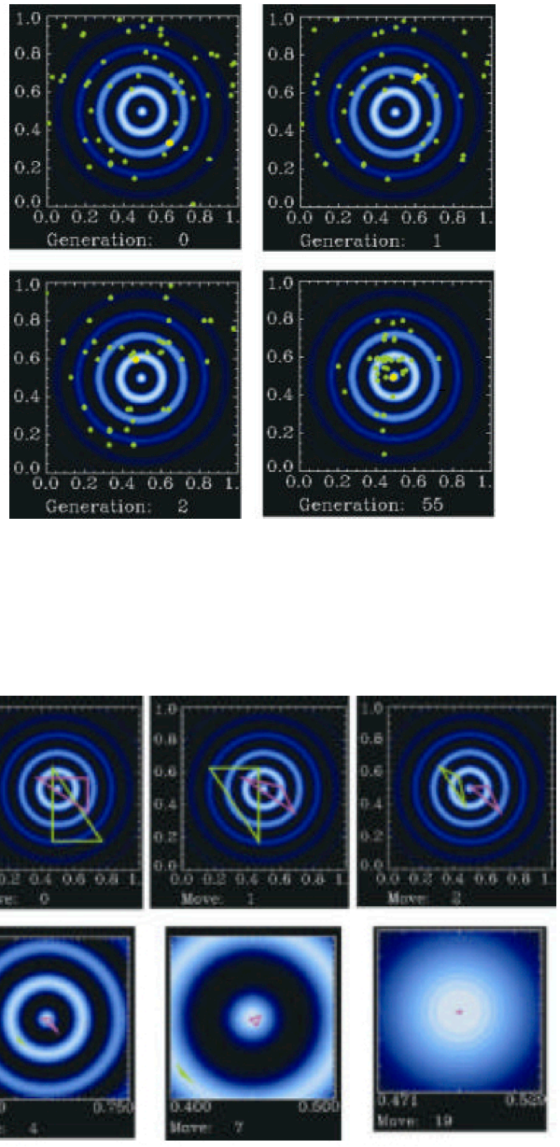

Figure 3.10: Comparison, during the research of minimum, between Genetic Algorithm (top) and down hill simplex method (bottom). The concentric circles in both figures indicate the rings of secondary maxima, and the larger, solid dot in the top figure is the fittest solution of the current generation while in the bottom figure the two triangles represent the used simplex .

4 Combining strong-motion, InSAR and GPS data to refine the fault geometry and source kinematics of the 2011, Mw 6.2, Christchurch earthquake (New Zealand)

4.1 Introduction

On 21 February 2011 at 23:51 (UTC time), the Mw 6.2 Christchurch earthquake occurred near (just 7 km southeast) the center of the Christchurch city, the second largest city in New Zealand, on the south island. State that the best-double couple focal mechanism for the event initially indicates oblique slip (59/59/147, strike/dip/rake GCMT), although the large degree of non-double couple motion points to source complexity. Extremely high accelerations (as 2.2 g, being g the gravity acceleration) were recorded near the epicenter area (Kaiser *et al.* 2011). Additionally, this event caused soil liquefaction, landslides, large rockfalls and a widespread damage to buildings of Christchurch (the damage was valued at about US$ 12-16 billion), and, tragically, 185 confirmed fatalities. The Christchurch

earthquake occurred just six months after the 4 September 2010, Mw 7.1 Darfield earthquake, which broke the previously unknown Greendale fault in the west area of the Canterbury plain (figure 4.1).

For the Christchurch earthquake different fault geometries and source models for the slip and rupture velocity distributions are available in literature (Beavan *et al*. 2011; Barnhart *et al*. 2011; Holden *et al*. 2011 Elliott *et al.* 2012, Beavan *et al*. 2012, Atzori *et al*. 2012). In particular, in these works authors proposed both simple (one fault plane) (Beavan *et al*. 2011, Barnhart *et al*. 2011, Holden *et al*. 2011) and complex (two o more fault planes) (Elliott *et al*. 2012, Beavan *et al.* 2012, Atzori *et al*. 2012) fault geometry solutions. These geometries were inferred analyzing GPS data and aftershocks distribution (Beavan et al. 2011, Barnhart *et al*. 2011) and different InSAR data-sets (Elliott *et al*. 2012, Beavan *et al*. 2012, Atzori *et al*. 2012). On the other hand, the large complexity of the coseismic surface displacement close to the epicentral area (around Christchurch city), deriving from both GPS and InSAR data, indeed seems to suggest that a complex fault geometry with 2 or more fault planes is more realistic than a model with a single plane.

The aim of this study is to investigate the fault geometry of the Christchurch earthquake from the analysis of the GPS and InSAR data-sets and then to derive a kinematic source model from the joint inversion of all the available strong-motion, GPS and InSAR data-sets, through the non-linear inversion method based on the simulated annealing algorithm developed by Delouis *et al.* (2002). This method was modified during this Phd thesis to account both the exploration of fault geometry and estimation of errors associated to retrieve parameters. Particular importance was also given different preliminary analyzes performed on the original data-sets. This analyzes was performed through different procedure and method developed during this work. Preliminarily, as explained in the following, we performed a selection of the available deformation data combining GPS and SAR observations in order to find a model able to explain the complex geometry of the coseismic

displacement data. No kinematic rupture models for the 21 February 2011

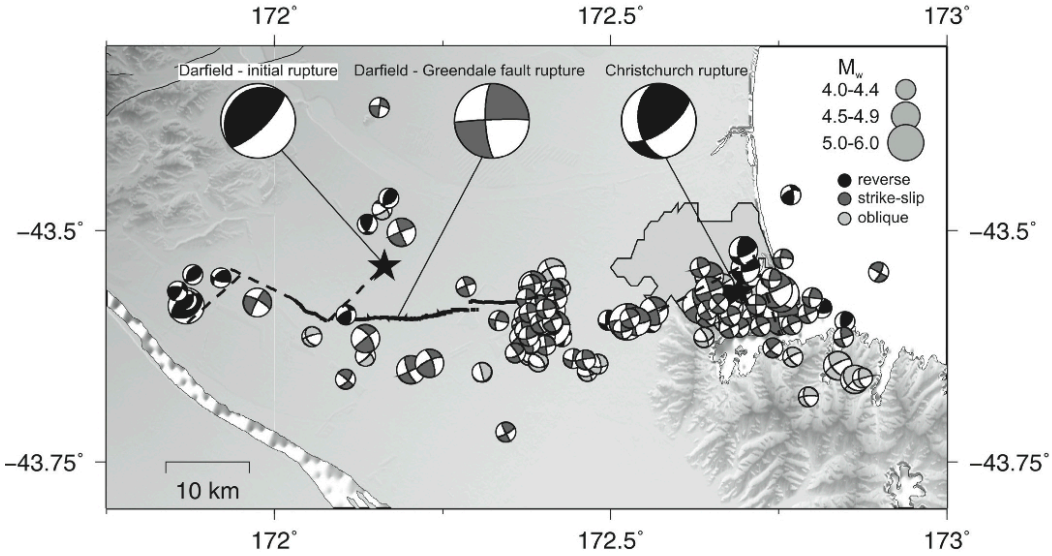

Figure 4.1: Regional CMT focal mechanism for Mw > 4.0 shocks within the 2012-2011 Canterbury sequence. The black line represents the superficial trace of the Greendale fault, responsible for the Darfield earthquake.

Christchurch earthquake have been proposed in the previous studies (Beavan *et al*. 2011; Holden, 2011; Barnhart *et al*. 2011; Beavan *et al*. 2012; Atzori *et al*. 2012; Elliott *et al.* 2012) combining strong-motion, InSAR and GPS data in a joint inversion.

4.2 Tectonic and geological setting of the Canterbury plains

Seismicity in New Zealand is associated with the movements related to the boundary of the Pacific and Australian plates (40 mm/yr). The regional tectonics is dominated by three major structure: the oblique subduction of the Pacific plate beneath the Australian plate along the Hikurangi Trough; oblique right-lateral

striking structures such as the 650 km-long Alpine fault (according to DeMets *et al.* (1994) and Sutherland *et al.* (2006) this fault accommodates 70-75 % of the 40 mm/yr plate motion) and the Marlborough fault zone; the oblique subduction of the Australian plate beneath the Pacific plate on the Puysegur Trench (figure 4.2).

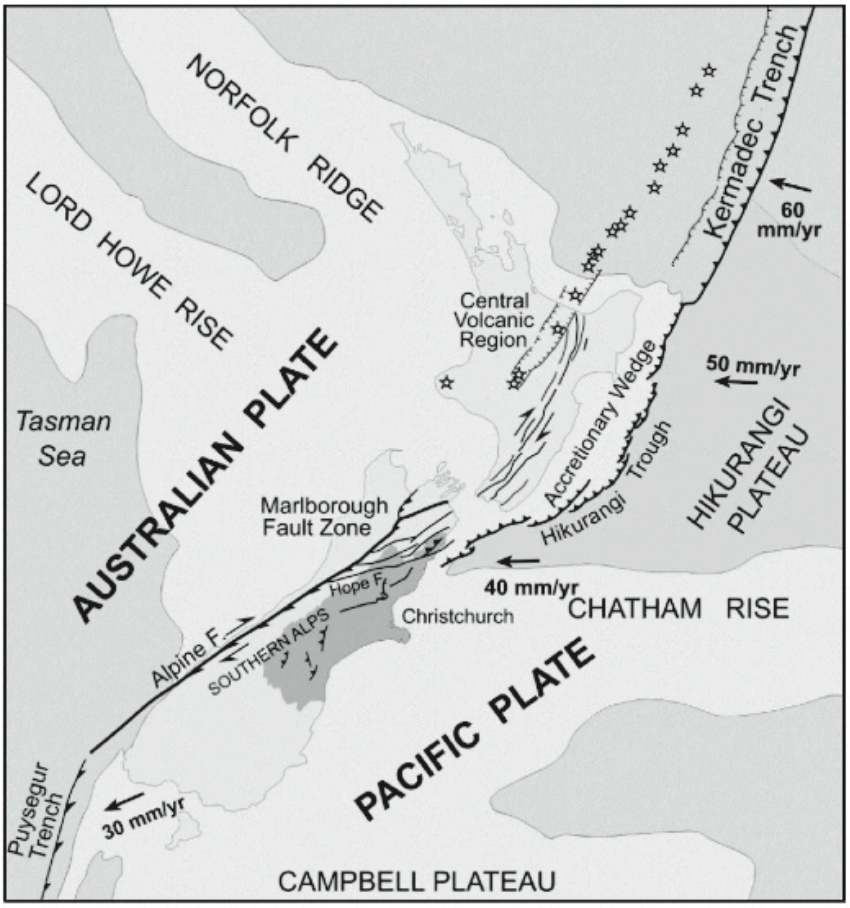

Figura 4.2: Tectonic setting of New Zealand (after Bradley & Cubrinovski 2011)

The Christchurch earthquakes is one of the main aftershocks of the Canterbury sequence, which began in September 4, 2010 with the Mw 7.1 Darfield earthquake that occurred in the western part of the Canterbury plains (figure 4.1). The

magnitude of the Christchurch

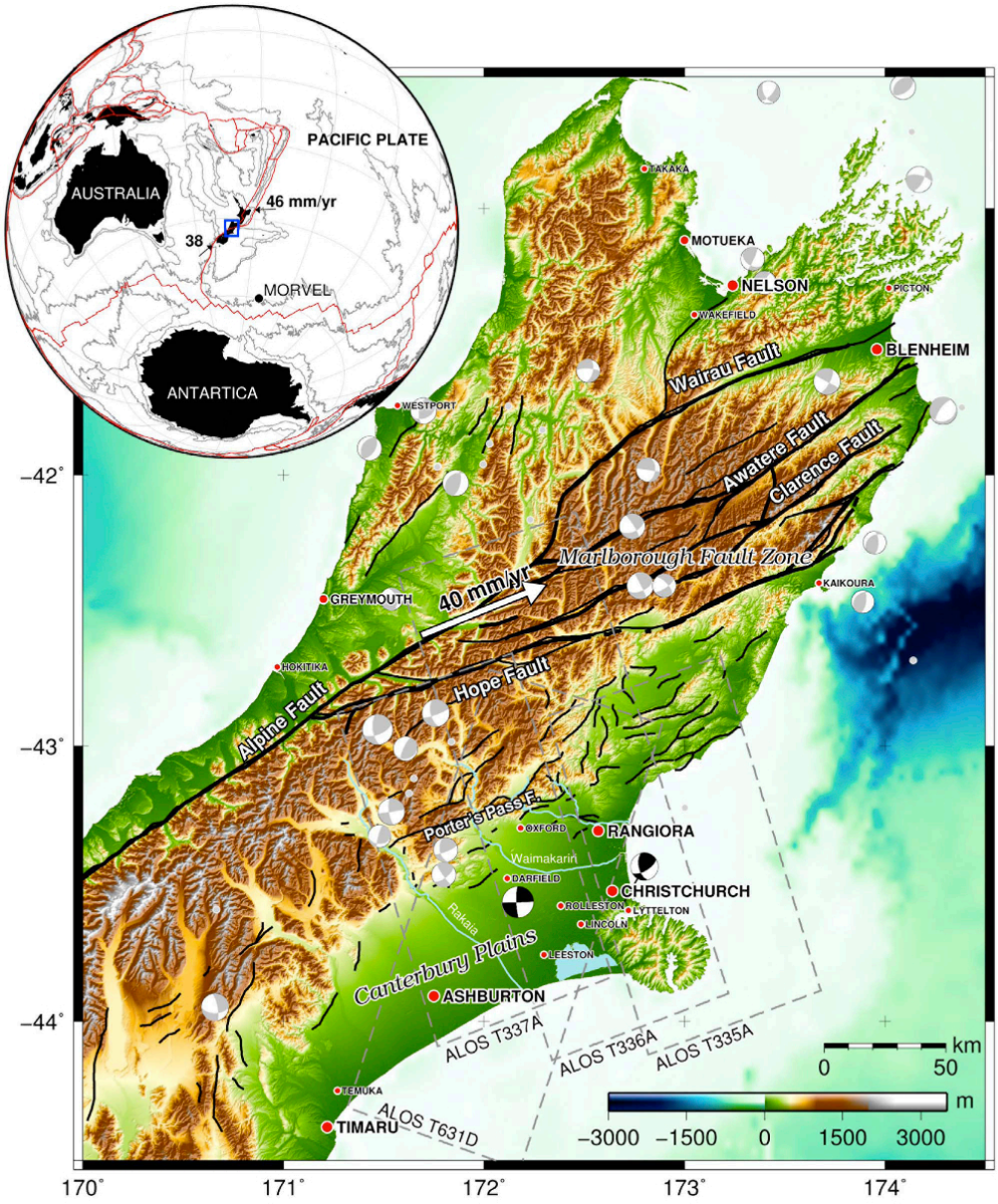

Figura 4.3: Active fault map, earthquakes, topography and place names of the northern half of the South Island of New Zealand, covering the recent earthquake epicentral regions of Darfield and Christchurch at the north end of the Canterbury Plains. Focal mechanisms are from the GCMT catalogue for the 2010 and 2011 events studied here (black) and earthquakes Mw 5.5+ (grey) covering the period 1976–2009 [Ekström et al., 2005]. Earthquake epicenters

from the Engdahl catalogue [Engdahl and Villaseñor, 2002] are shown by grey circles. The active faults (black lines) are from the Institute of Geological and Nuclear Science (GNS) Active Faults Database. The main Alpine Fault and faults of the Marlborough Fault Zone (Hope, Clarence, Awatere and Wairau Faults) are marked to the north of Christchurch. Grey dashed outlines indicate the footprints of InSAR coverage for the three ascending and one descending ALOS tracks. The white arrow indicates the 40 mm/yr of relative motion of the Australian Plate relative to the Pacific Plate based upon the MORVEL motion [DeMets et al., 2010]. The inset map indicates the region of study (blue rectangle), plate boundaries (red) from Bird [2003], relative plate velocities (mm/yr) at the tips of New Zealand and the MUVEL pole of rotation [DeMets et al., 2010] (after Elliott et al., 2012).

earthquake (Mw 6.2) was larger than the magnitude of the two previously largest aftershocks, which occurred just some days after the Darfield event, characterized by Mw 4.8 and 4.9, respectively. The Darfield earthquake occurred on the previously unknown 40 km long Greendale fault (Gledhill *et al.* 2011) located about 30 km west of Christchurch. As with the Darfield earthquake, the Christchurch event also occurred on a previously unknown fault under the city of Christchurch. Before the beginning of the Canterbury sequence, the area was in fact characterized by a very low seismicity rate at least in the last 5 decades (Engdahl & Villaseor, 2002). Moreover, before the sequence, the principal seismic hazard for this region was presumed to arise from the major fault, present and mapped on the Marlborough Fault Zone (figure 4.3). Indeed, before the Canterbury sequence, the area was characterized by a very low seismicity rate (Bannister *et al.* 2011). Nevertheless, the geodetic data acquired before 2010 indicated that strain was slowly accumulating within the region (Wallace *et al.* 2007; Beavan *et al.* 2002), leading to suspect the presence of active faults in the subsurface of the Canterbury area.

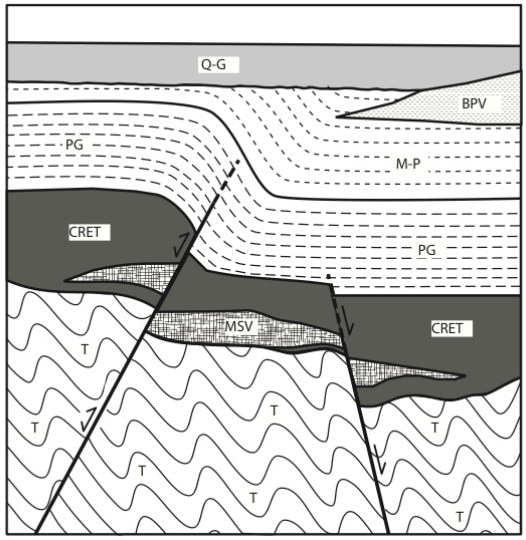

Figure 4.4: Synoptic tectonostratigraphic column for the Canterbury Plains (not to scale). T=Torlesse basement assemblage; CRET = Late Cretaceous terrestrial sequence; MSV=Mt. Somers volcanics; PG= Paleogene marine sequence; M-P = Miocene-Pliocene marine-terrestrial sequence; BPV = Miocene Banks Peninsula volcanics; Q-G = Quaternary gravels (after Sibson *et al.* 2011).

On the other hand, the late Quaternary alluvial fan deposits that generally cover the Canterbury plains make it very difficult to recognize such faults (Forsyth *et al.* 2008) (a detailed description of the local geology (figure 4.4) of this area is: a basement of highly deformed Mesozioc Torlesse metagraywackes; a Late Cretaceous-Neogene cover sequence; a cover sequence of Late Cretaceous-Paleogene terrestrial-marine sedimentary units; a regressive Miocene-Pliocene clastic sequence containing the basaltic Bank Peninsula volcanism; Quaternary alluvial fan deposits.). Thus, the occurrence of the sequence was in part a surprise. The Christchurch earthquake was followed by two major aftershocks of Mw 5.8 and 5.9, that occurred within two hours of the mainshock and located SSW of the main event (Bannister *et al.* 2011). These two events were characterized by a strike-slip focal mechanism. Furthermore, the aftershocks distribution, inferred the locations performed by GeoNet, seems to highlight a prevalent east-west trending

(Bannister *et al.* 2011). A further Mw 6.0 aftershock occurred on 13 June 2011, with an epicenter some 5 km further to ENE.

Evidence on the contemporary regional stress field in the central South island (Sibson *et al*. 2011, Sibson *et al*. 2012), were derived mainly from: stress inversion from earthquake focal mechanism, breakout determination from Galleon-1 borehole (Wilson *et al*. 1985) and strain-rate derived from GPS studies. Results of these analyzes suggests a uniform regional stress field on the Canterbury region with maximum compressive stress σ_1 horizontal and orientated WNW-ESE ($\sim 115^o$)(see figure 4.5). Similarly, Wallace *et al*. 2007 employed a rotational elastic block model to describe present deformation in the South Island, founding a maximum contraction strain rate oriented 100 ± 8^o within the Canterbury/Otago block.

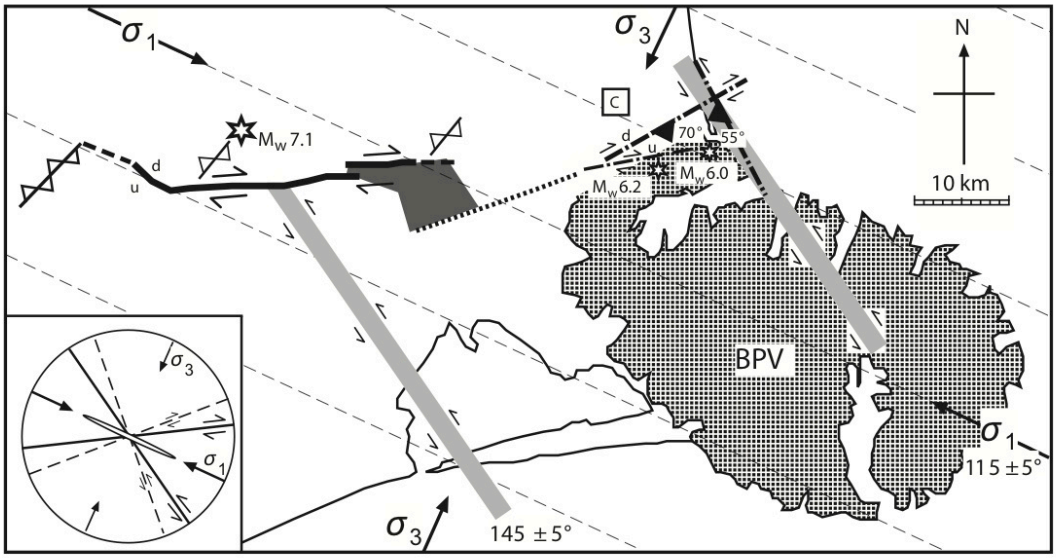

Figure 4.5: Seismotectonic carton of the 2010-2011 Canterbury sequence in relation to the surface outcrop of Banks peninsula volcanism (BPV), central Christchurch city (C), and the inferred regional stress field. Epicenter of major aftershocks are represented by stars; thick bold line= Greendale fault surface rupture. The left box represents the expected orientations of newly formed structures (ellipse=extension fracture; solid lines= Coulomb shears; dashed lines= ductile shears)(after Sibson *et al.* 2011)

4.3 Inversion technique

To invert strong-motion and coseismic displacement data we adopt the approach proposed by Delouis *et al.* (2002).

The forward problem for the strong-motion data is solved through the representation theorem (Aki & Richards, 1980 and 2002) written in terms of moment-rate (starting from equation 2.17 to obtain the representation theorem in terms of moment rate we have use the similarity $\dot{M} = \mu A \dot{\Delta u}$, where $\dot{M}$ is the moment-rate, μ is the rigidity, A is the Fault area and $\dot{\Delta u}$ is the slip-rate) assuming that each single subfault, in which the fault plane is discretized, can break only once when it is reached by the propagating rupture front. The Green functions associated with a simple shear dislocation point-source located at the center of each subfault, are computed, at any station, by the discrete wavenumber method of Bouchon (1981) in a 1D velocity model. In this way we are able to compute full-wavefield synthetic seismograms. For the application to the Christchurch earthquake presented in this paper we used the 1-D velocity model provided for the area under investigation by Reyners & Cowan (1993).

The Source Time Function (STF) for each subfault is parameterized according to Nabelek (1984) and it is represented by a set of isosceles triangular time windows of variable height, and mutually overlapping (figure 4.6).

The number and duration of triangles has to be mainly chosen according to the dominant period of real data. Following this representation of the source, the parameters that are searched through the inversion of strong-motion records, or joint seismological – geodetic data, are the rupture onset time, the rake direction, and the amplitude for any of the triangular moment rate functions used (figure 4.6).

As for the strong-motion data, even for the GPS and InSAR data the synthetic displacements are obtained through the resolution of the representation theorem.

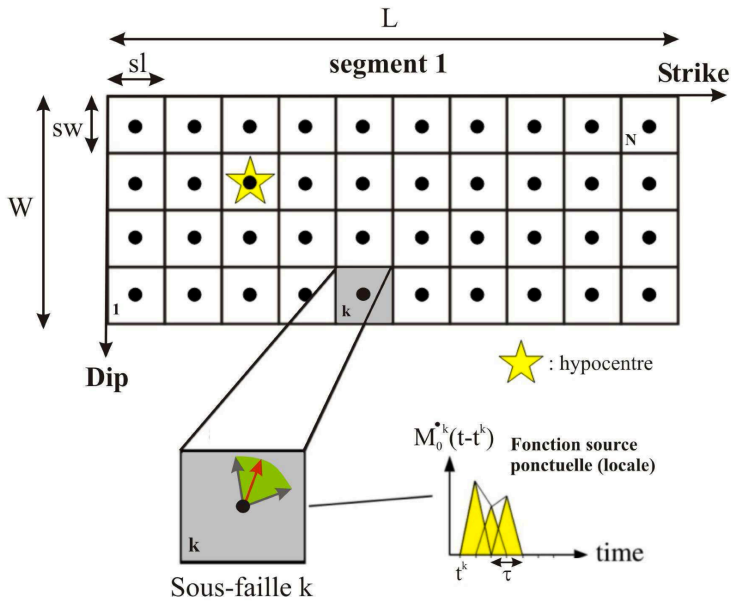

Figure 4.6: Parameterization used for any fault segment. Each fault segment is rectangular, but the total rupture model can include various fault segments. Any segment is represented by a regular grid of source points (black dots), located at the centre of any cell, of sizes sl and sw, called sub-faults (SF). The hypocentre coincides with one of the source points of the main segment. The strike, dip, L and W of each fault segment are fixed *a priori*, as well as the size for each SF (sl and sw). The rake angle, represented by the red vector, can vary on the different SF, within an interval defined a priori. The $\dot{M}_0^k(t)$ function is the punctual Source Time Function (STF) which can vary from the different SF. The STF is represented by a series of triangular functions (NT) of width (τ). The initialization time for any SF is free to vary depending on the velocity rupture interval defined *a priori*.

The Green functions for the static displacement are generated using the formulation of Savage (1980) (see paragraph 2.13) that considers each subfault as a slipping surface embedded in an elastic half-space. However, the coseismic static displacements are sensitive only to the rake and to the local slip value, not the time history of the rupture. The local slip value can be obtained from the local STF, since the area under the STF is equal to the local seismic moment that is in turn related to the local rupture area (known) and to the slip amplitude. Furthermore, since the InSAR data represent a relative measurement of displacement, the static offset for the InSAR data became another parameter that we explore trough the

inversion.

The total cost function (F_{cost}) in the inversion procedure is defined as the sum of two terms. The first one is the weighted (w_j) sum of the root mean-square misfit function i.e., the L_2 norm of observed minus synthetic data, normalized by the observed data (rms_j), for the N_D available data sets. In this case-study, we have N_D=3 different data-sets corresponding to strong-motion, InSAR, and GPS data. An additional term in the cost function is introduced in order to minimize the total seismic moment of the model moment (M_{omod}) taking into account an a priori value of seismic moment ($M_{oapriori}$). In conclusion, the misfit function is given by:

4.1

$$Fcost = \frac{\sum_{j=1}^{N_D}(w_j(\sqrt{\sum_{i=1}^{n}(O_i - C_i)^2 / \sum_{i=1}^{n} {O_i}^2})_j)}{\sum_{j=1}^{N_D}(w_j)} + C_{M_0} e^{((\frac{Mmod}{Moapriori})-1)}$$

where O_i and C_i represent the real (observed) and synthetic (computed) data, n is the number of data for any data sets and the coefficients C_{Mo} is the weight for the moment constraint.

For searching the minimum of the cost function, the model space is explored in a quasi-global manner by using the simulated annealing algorithm (Aarts & Korst 1989). However, before performing the inversion, we have to set the investigation ranges for any of the model parameters (i.e., rupture time, rake direction, and moment-rate).

Moreover, we first invert only the coseismic static displacements associated with InSAR and GPS data to search for the optimal fault orientation and position. We will call this step the “fault inversion”. In the case of Christchurch event, we started fixing the position in space of the fault center by-eye on the basis of the shape of the SAR’s fringes near to the epicentral location area.

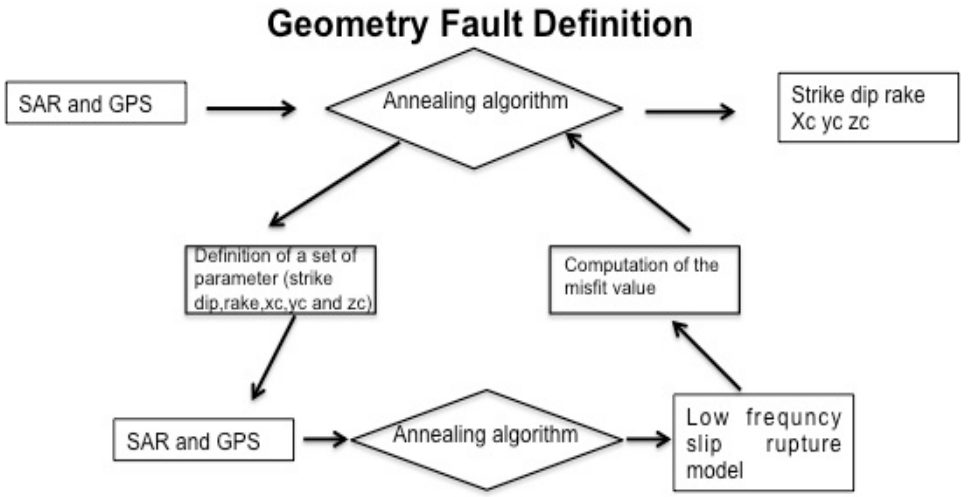

Figure 4.7: Block diagram for the method used to determine the geometry and mechanism for the Christchurch earthquake.

Then, we searched for the better position (x_c, y_c, z_c) of the fault center, and strike and dip angles, through the inversion of InSAR and GPS data. In other words, the "fault inversion" scheme is based on the use of two nested cycles. The external cycle allows for exploring the position and orientation of the fault plane; by using the internal cycle we search for the slip distribution on the fault plane retrieved in the external cycle (see figure 4.2). This "fault inversion" scheme is of course expensive from the computational point of view mainly because for any given fault plane we need to compute the Green function. However this approach there is no trade-off between the fault depth and slip amplitude (Beavan *et al.* 2011).

4.4 Data

For the Christchurch earthquake a large amount of data of different nature, such as strong-motion, GPS and SAR data, are available due to the great expansion of the accelerometric and GPS networks that followed the occurrence of the Darfield earthquake.

TABLE 1
Strong Motion Stations and Near-source Recordings of the 22 February 2011 Christchurch Earthquake

Station Name	Code	Site class *	R_{jb} † (km)	R_{rup} ‡ (km)	PGA § (g)	PGV || (cm/s)	D_{s5-95} # (s)	PGA_v ** (g)
Canterbury Aero Club	CACS	D	12.7	12.8	0.21	20.0	11.8	0.19
Christchurch Botanic Gardens	CBGS	D	4.6	4.7	0.50	46.3	10.7	0.35
Christchurch Cathedral College	CCCC	D	2.6	2.8	0.43	56.3	9.8	0.79
Christchurch Hospital	CHHC	D	3.7	3.8	0.37	50.9	10.3	0.62
Cashmere High School	CMHS	D	1.0	1.4	0.37	44.4	5.1	0.85
Hulverstone Dr Pumping Station	HPSC	E	3.8	3.9	0.22	36.7	10.0	1.03
Heathcote Valley School	HVSC	C	1.4	4.0	1.41	81.4	5.7	2.21
Kaiapoi North School	KPOC	E	17.3	17.4	0.20	18.9	11.3	0.06
Lincoln School	LINC	D	13.5	13.6	0.12	12.7	12.1	0.09
Lyttelton Port	LPCC	B	4.8	7.1	0.92	45.6	4.0	0.51
Lyttelton Port Naval Point	LPOC	C	4.2	6.6	0.34	69.1	7.7	0.39
North New Brighton School	NNBS	E	3.7	3.8	0.67	35.1	2.4	0.80
Papanui High School	PPHS	D	8.6	8.6	0.21	36.7	12.8	0.21
Pages Rd Pumping Station	PRPC	E	2.3	2.5	0.63	72.8	3.8	1.88
Christchurch Resthaven	REHS	D	4.6	4.7	0.52	65.4	10.2	0.51
Riccarton High School	RHSC	D	6.5	6.5	0.28	29.8	9.9	0.19
Rolleston School	ROLC	D	19.6	19.6	0.18	8.4	10.3	0.08
Shirley Library	SHLC	D	5.0	5.1	0.33	67.8	7.0	0.49
Styx Mill Transfer Station	SMTC	D	10.7	10.8	0.16	27.6	13.6	0.17
Templeton School	TPLC	D	12.5	12.5	0.11	11.3	15.3	0.16

* As defined by the New Zealand Loadings Standard, NZS1170.5 (2004)
† Joyner-Boore distance from surface projection of fault plane to site
‡ Closest distance from fault plane to site
§ Peak ground acceleration
|| Peak ground velocity
Significant duration (5–95%)
** Peak vertical ground acceleration. Note that with the exception of PGA_v, ground motion parameters are geometric mean horizontal definition

Table 4-1: Main characteristics of recording stations of the Christchurch earthquake (after Bradley *et al.* 2011).

4.4.1 Strong motion data

After the 2010, September 4 Darfield earthquake the New Zealand accelerometric network in the Canterbury plains was supplemented by 13 additional strong-motion stations with CUSP-3 data-logger and triaxial MEMs sensors, by the GeoNet network (New Zealand National Hazard Monitoring Network) and its regional component, the CanNet network (Canterbury Network).

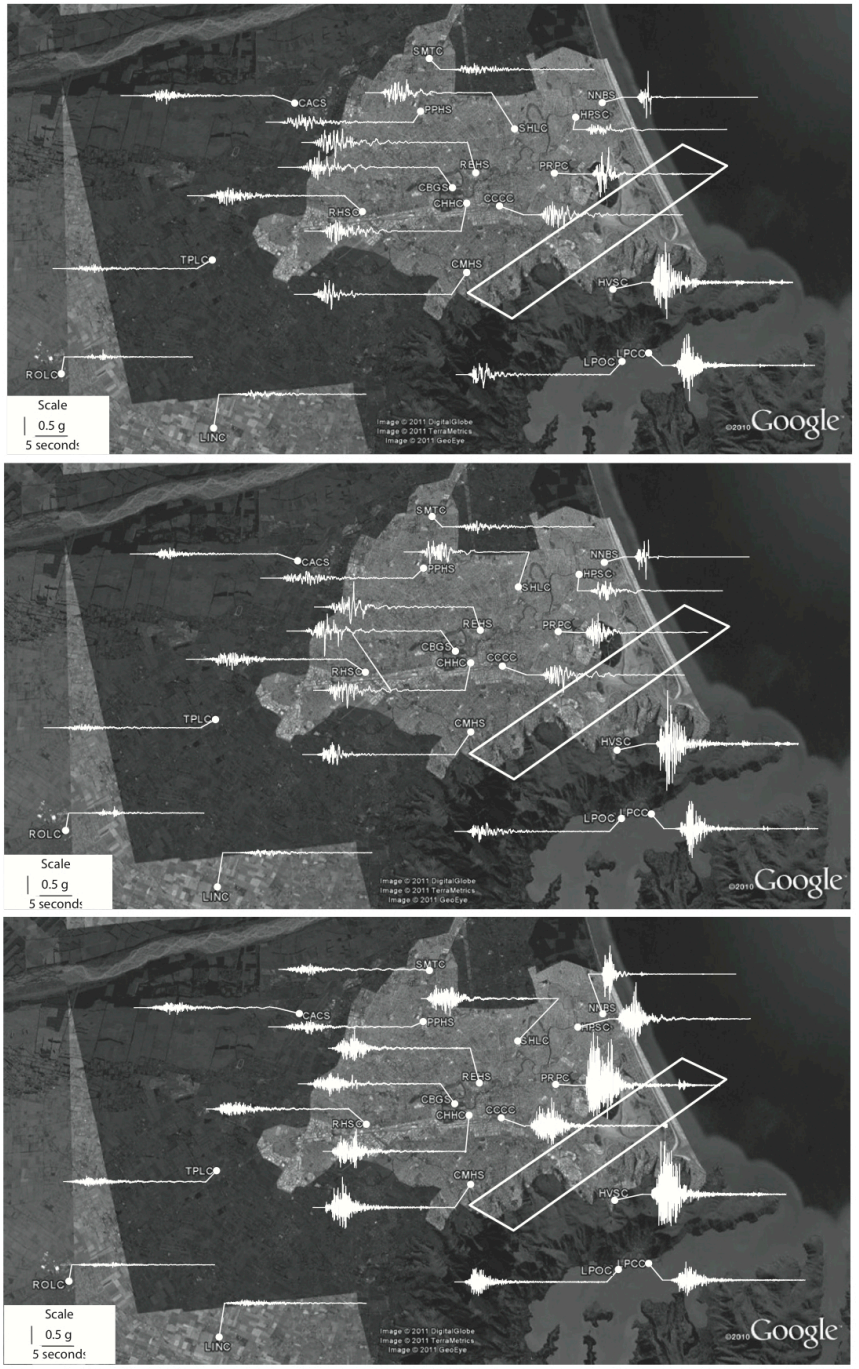

Figure 4.8: From top to bottom, fault-normal and parallel horizontal and vertical acceleration time histories observed at various locations in the Christchurch region from the 21 February earthquake, respectively.

The Christchurch earthquake was then recorded at 25 stations at epicentral distance between 2 and 50 km (see figure 4.8 and table 4.1).

On the basis of some preliminary analyses performed using the fault geometry proposed by Beavan *et al.* (2011) and looking at the soil conditions (see table 4.1), we decided to use only the 10 strong-motion stations (black triangles in figure 4.9) located at distances ranging between 2 and 20 km. The selected stations show in any case a good azimuthal coverage. Some of the discarded stations (e.g., ROLC, TPLC and CACS) simply represent a duplication of the selected ones. Moreover, stations like PRPC, SHLC and HPSC are contaminated by strong site effects linked to intense liquefaction phenomena first recognized in the case of the Darfield earthquake (Beavan *et al.* 2010 and Palermo *et al.* 2010) so we decided to exclude them from our modeling. However, all recordings used in this study are influenced at some degree by site effects. The Canterbury plain is in fact characterized by very shallow layers inducing non-linear amplifications or trampoline effects (Fry *et al.* 2011). Moreover, as pointed out by Holden *et al.* (2011), ground conditions within Christchurch are highly variable and will require further studies for stations in this region to be included in the modeling. To choose the correct frequency band in which filtering data, two independent analyses were performed. First, we searched for the frequency range in which the S-phase polarization was stable (e.g., Emolo & Zollo, 2005), finding 0.05-0.5 Hz as the optimal frequency range for all the selected records (figure 4.10).

Then, we performed some preliminary strong-motion inversions in different frequency bands around the limits obtained from the polarization analysis and selecting the range providing the lowest misfit. We found 0.1-0.5 Hz as the best frequency band.

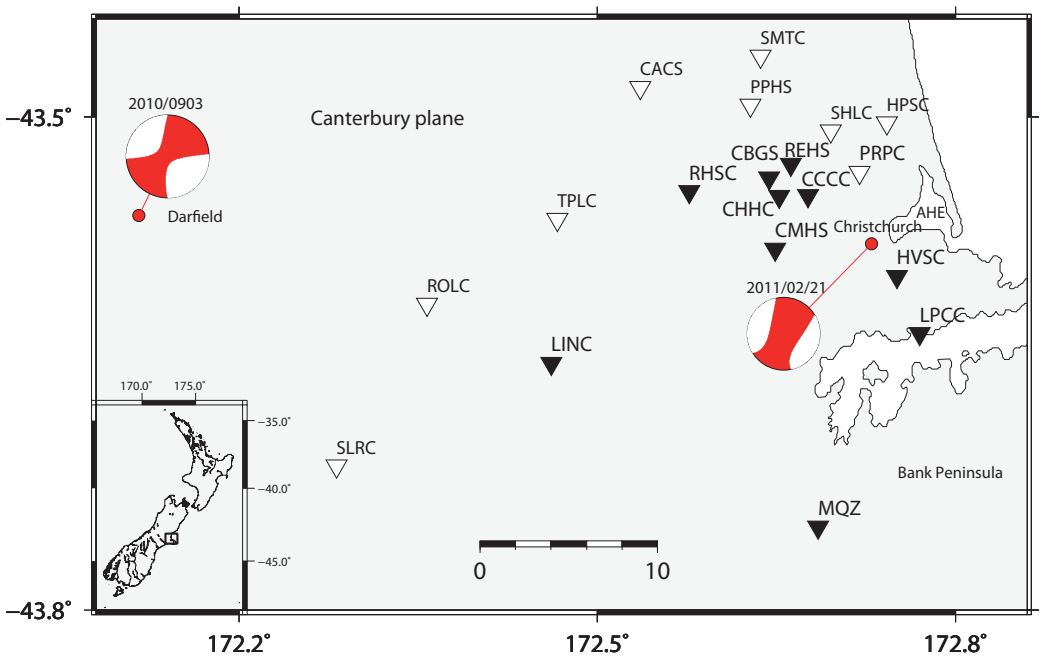

Figure 4.9 Source-receivers geometry for the Christchurch event. The triangles correspond to the GeoNet (New Zealand National Hazard Monitoring Network) and CanNet (Canterbury Network) strong-motion stations installed in the Canterbury plains. The white and black triangles indicate the discarded and used seismic stations, respectively. Red dots represent the epicentral location for the 4 September 2010, Mw 7.1 Darfield and for the 21 February 2011, Mw 6.2, Christchurch (Bannister *et al.* 2011) earthquake. The focal mechanisms, from the Global Centroid Moment Tensor catalogue, for these two events are also shown in the Figure.

Thus, accelerometric data to be used in the inversion were processed removing mean and trend, integrated twice, and band-pass filtered in the range 0.1-0.5 Hz by a 3 poles Butterworth filter. The horizontal components form the CanNet stations were also rotated, from their original orientation, to the North-South and East-West orientation. Finally, data were decimated from their original sampling frequency to 2.5 Hz.

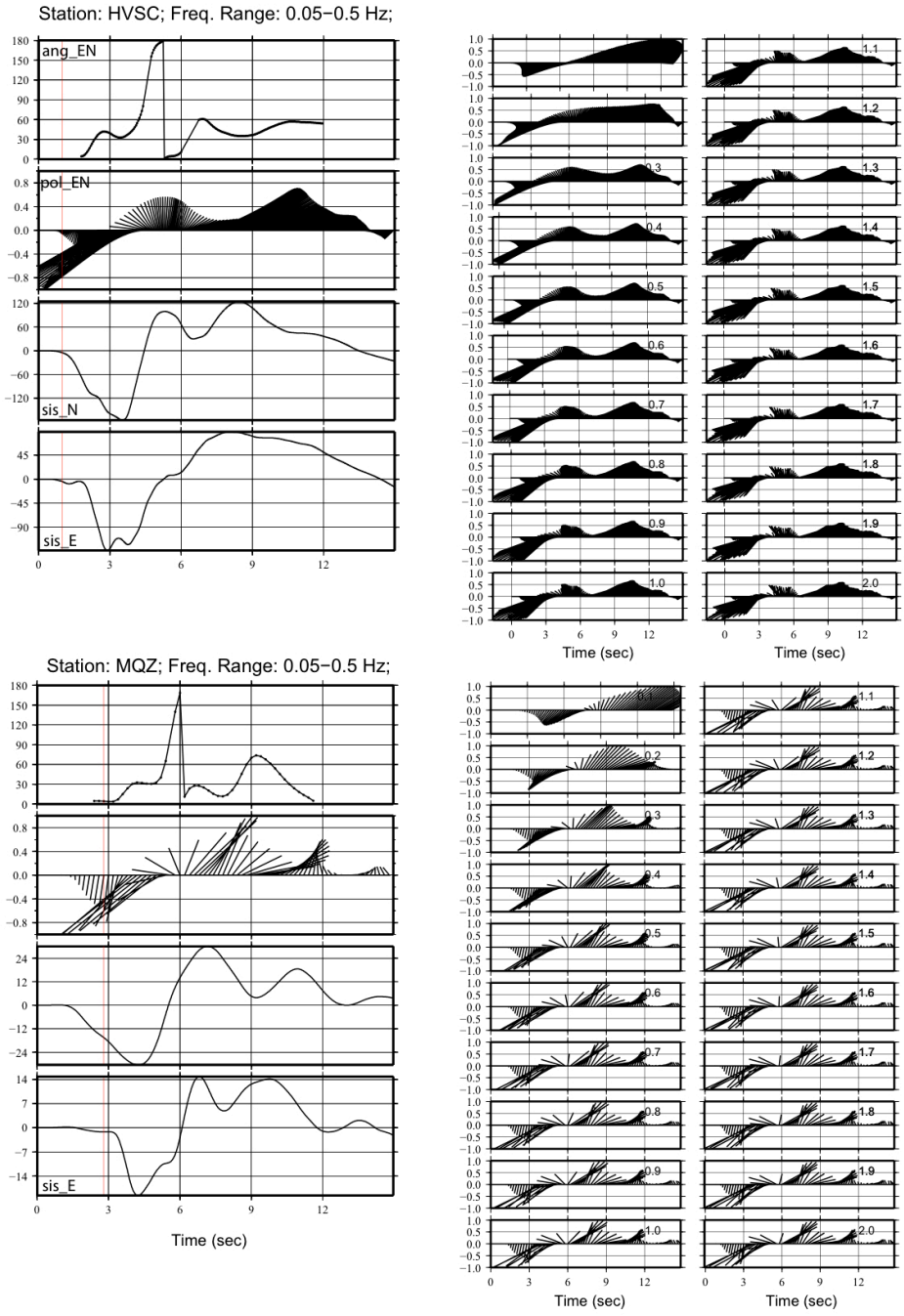

Figure 4.10: Example of polarization analysis for the station MQZ and HVSC.

4.4.2 The InSAR data

The InSAR data used to model the Christchurch earthquake were the same used by Elliott *et al.* (2012), and derived from the Japanese Aerospace Exploration Agency's (JAXA) L-Band ALOS instrument (for all the information related to the two used track we referred to the table 5 of Elliott *et al.* 2012). The two tracks available for the studied area, i.e., tracks 335 (panel a of figure 4.11) and 336 (panel b of figure 4.11), are partially overlapping and cover most of the deformation area around the Christchurch city. The two ascending interferograms were acquired within the time periods 10 January-25 February 2011 (track 335), and 27 October 2010-4 March 2011 (track 336). The two longer-wavelengths ALOS data, particularly the 336 track, present some area on the eastern part of the Christchurch city, where the fringes of the SAR data were incoherent, likely as a consequence of soil liquefaction. In fact, as said before, the 2010 Darfield earthquake generated strong liquefaction phenomena and also building damage on this part of the city (Palermo *et al.* 2010), which presumably changed the scattering properties of the ground.

Nevertheless, coherent fringes coverage is clearly visible just west of the Avon-Heathcote estuary, in particular for the 335 track (figure 4.11 panel a). The fringes shape in this area is of great importance because it could provide information related to the geometry of the rupturing source. The peak displacement along the line-of-sight (los) was about 50 cm (toward the satellite) in the south-east area of the Christchurch city of about 50 cm, and about 24 cm around the center. For all the information related to the processing of the SAR data we refer to the work of Elliott *et al.* (2012). Two additional tracks from ascending and descending orbit were available for the Christchurch area from the Italian Cosmo-SkyMed (CSK) X-band radar satellite, acquired on 19 and 23 February 2011, and 20 February and 16 March 2011, respectively. However, these data are highly incoherent so we decided to not using them in our modeling.

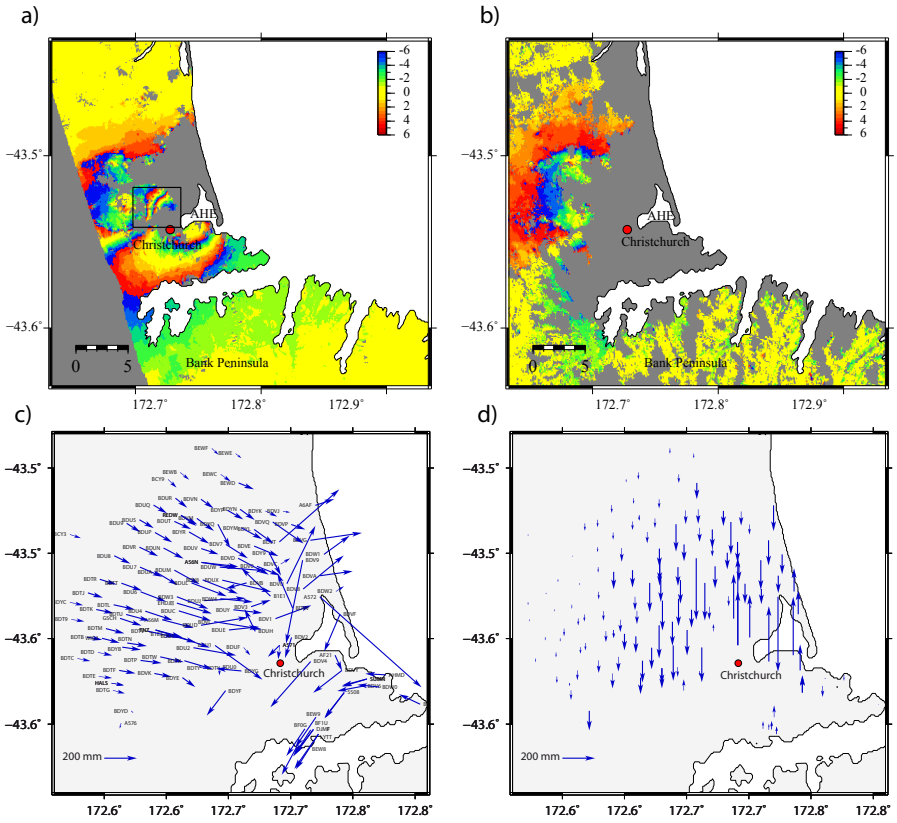

Figure 4.11: Coseismic geodetic deformation data (InSAR and GPS) for the Christchurch earthquake. Panels a and b show the two ascending interferograms, acquired within the time periods 10 January-25 February 2011 (track 335) and 27 October 2010-4 March 2011 (track 336), respectively. In panel a the black box indicates the area with the highest complexity of the fringes shape. The panels c and d represent the horizontal and vertical component, respectively, of the GPS sites used in this work. In the Figure, red dots correspond to the epicentral location of the Christchurch earthquake (Bannister *et al.* 2011).

4.4.3 The GPS data

A total of 193 GPS sites are available for the Christchurch earthquake: 57 sites are campaign GPSs collected between the 28 February and the 14 April 2011 subsequently the Darfield earthquake; 5 points are continuous GPS (cGPS) from regional sites of the Land Information New Zealand (LINZ) operated by the

GeoNet; 8 are cGPS operated by private companies in the Christchurch city; and 123 sites are low-accuracy campaign GPSs collected between the 14 and the 27 April 2011. For all the information relating to the processing of the GPS data we refer to the work of Beavan *et al.* (2011). To select the GPS sites to be inverted in order to determine the earthquake rupture model, we perform an initial selection based on the epicentral distance of GPS sites. In order to select the sites closest to the epicentral area, we set a threshold distance of 30 km, keeping in this way 132 sites (panel c and d Figure 4.11). Looking at the general trend of the GPS data (panel c of Figure 4.11), we can observe the presence of some sites (e.g., A572, BDUH, BDUF, and B1E1) having a shape and/or amplitude, especially on the horizontal component, which are not consistent with the general trend highlighted by other GPS. The general trend seems to suggest the presence of a fault plane, having a strike around 60^{o} and characterized by a strike-slip component. Beavan *et al.* (2011) tried to model the outliers increasing the complexity of the model, but they were not able to successfully model these anomalous GPS data. Thus, the analysis performed by Beavan *et al.* (2011) leads us to hypothesize that these sites were affected by large errors, associated, for instance, with the liquefaction phenomena, rather than the consequence of a complex rupture model.

We tried to model the complete set of data with a 2 fault model, without more success. We therefore performed a second selection in order to exclude from the data-set those data that could be considered as outliers (figure 4.12). To this end, we perform the following procedure:

- we computed, over a regular grid centered on the epicentral of the Christchurch earthquakes, the SAR values using a bicubic spline interpolation, obtaining in this way, the SAR values at the GPS sites;
- we projected the three GPS components on the line of sight (LOS) of the SAR and then computed the difference, at the GPS sites, between the SAR

values from the interpolations and the corresponding SAR values obtained from the three GPS components;

- using only some selected and considered most reliable GPS sites, we computed the mean value (μ) and the standard deviation (σ) of the SAR differences obtained in the previous step;
- we defined the interval [min;max], being

$$\min = \mu - \sigma$$

$$\max = \mu + \sigma$$

- and finally retained only those GPS data inside this range.

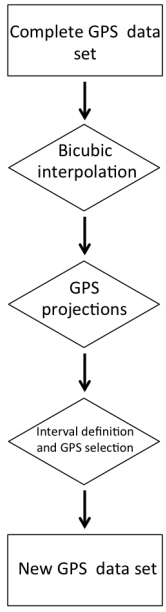

Figure 4.12: Block diagram representing the method adopted for GPS sites selection.

The results of this analysis are listed in figure 4.9. To compute the selection interval we chose only the GPS that in some previous analysis showed a surface

deformation very similar to that provided by the InSAR data. The corresponding GPS stations are only those reported in the red box in figure 4.8. The results obtained for this study, provide a μ and σ respectively of 1.5 and about 3 cm. Finally, we retain a total of 76 GPS site for the inversion. Moreover, the mean value of 1.5 cm also provides an indicative estimation of the offset value associated with the InSAR data. Moreover most of the GPS excluded by this analysis also coincides with the GPS sites with the greatest measuring error (see the GPS table provided by Beavan *et al.* 2011).

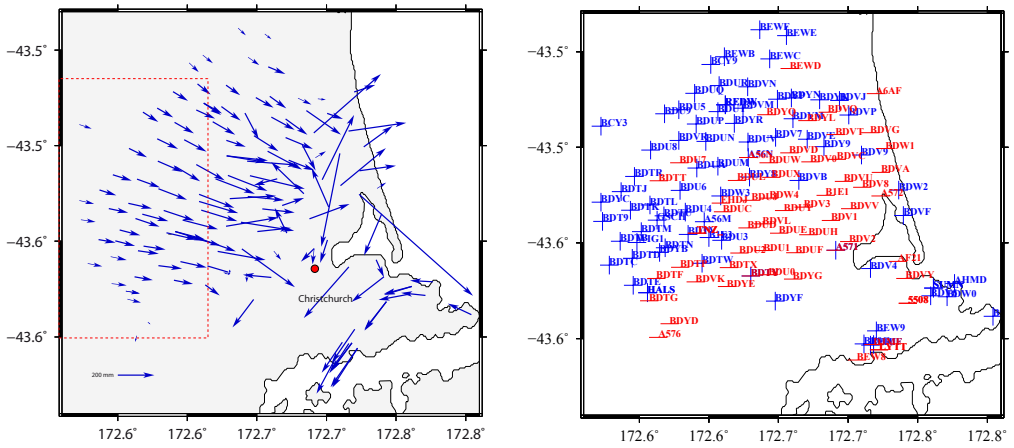

Figure 4.13: GPS data selection. In the left panel the red box delimitates the GPS sites used to select the GPS data to be used for the inversion (see text for details). The right panel hightlights the result of the GPS selection analysis. In this panel the blue and red colors indicate the used and discarded GPS sites, respectively.

4.5 Inversion results

The strong-motion, InSAR and GPS data selected as described in the previous section constitute the whole data set we used for the inversion.

Following the principle of parsimony, economy or succinctness as set out by the Occam's razor, we first tried to model the Christchurch earthquake using the simplest possible fault model, i.e., we started to model the event using a single fault

plane. A similar approach was also followed by Beavan *et al.* (2011) and Elliott *et al.* (2012), even if the complex pattern of InSAR and GPS data around the Christchurch city western of the Avon-Heathcote estuary suggests a more complex model. The same complexity seems also to be required from the moment tensor solutions from seismological catalogues (GeoNet) that shows a large non double-couple component for this event (Figure 4.9).

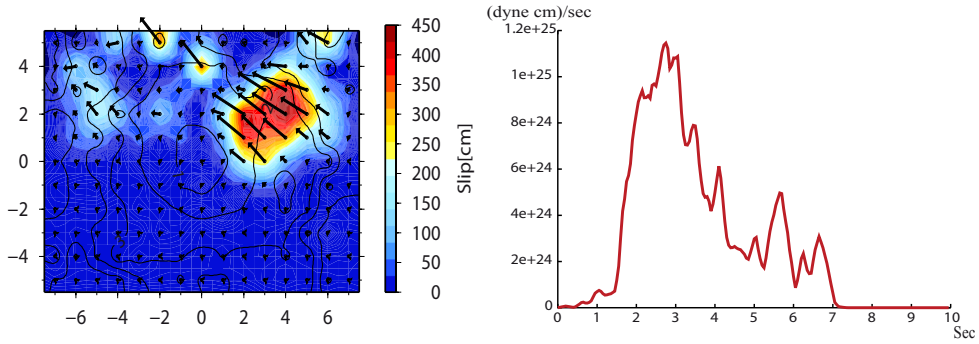

Figure 4.14: Kinematic rupture model for the Christchurch earthquake. The left panel shows the slip and onset time distribution for the Christchurch event, obtained assuming a single-fault plane model from the joint inversion of InSAR, GPS and strong-motion data. The position and geometry of the fault plane has been instead obtained from the analysis of coseismic geodetic data alone (InSAR and GPS). In the Figure, the black arrows indicate the slip vectors. The left panel shows the Global Source Time Function (GSTF) for the obtained slip model.

As described in the Method section (paragraph 4.3) , before performing the data inversion to retrieve the kinematic rupture model, we started searching for the geometry of the (single) fault plane to be used as *a priori* information for data inversion. Using the geodetic coseismic information (76 GPS sites and the track 335 for InSAR data), and fixing the fault center at the hypocentre, as suggested by

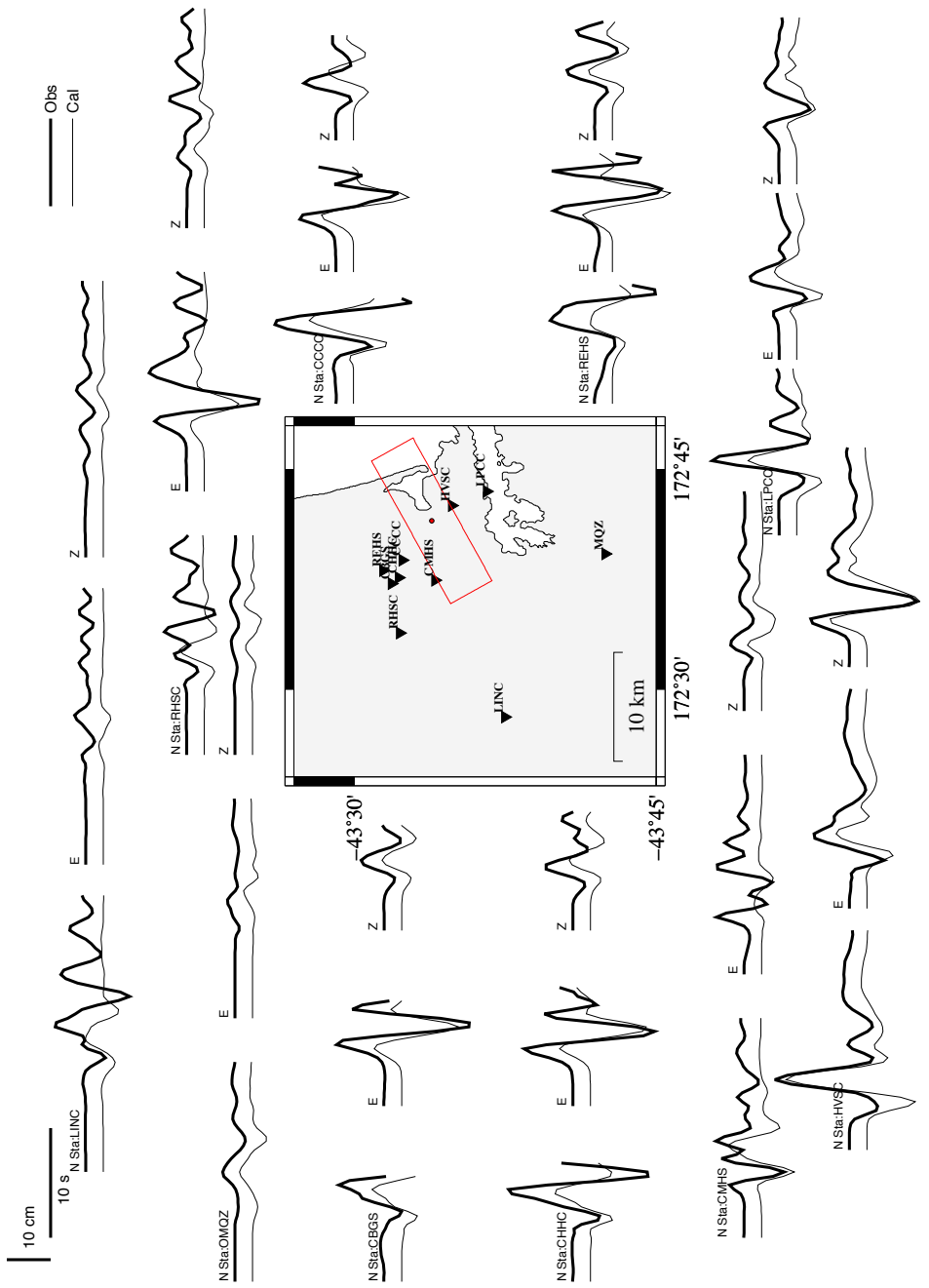

Figure 4.15: Real (thick lines) and synthetic (thin lines) computed, for the single fault model (red box), ground-displacement strong motion records for the north–south, west-east and up-down components, respectively. Data are band-pass filtered in the 0.1-0.5 Hz frequency range. The Figure in the middle shows the source-receiver and fault plane geometry used for the strong-motion inversion.

Bannister et al. (2011), we obtained a fault plane with a strike of about 61°, dipping toward SE with an angle of 66°, and an average rake of 166°.

With this fault geometry we then performed the joint inversion using data from the 10 selected strong-motion stations, the two SAR tracks and the 76 GPS sites. Plane dimensions equal to L=15 km and W=11 km and it was discretized in 1 km^2 subfaults.

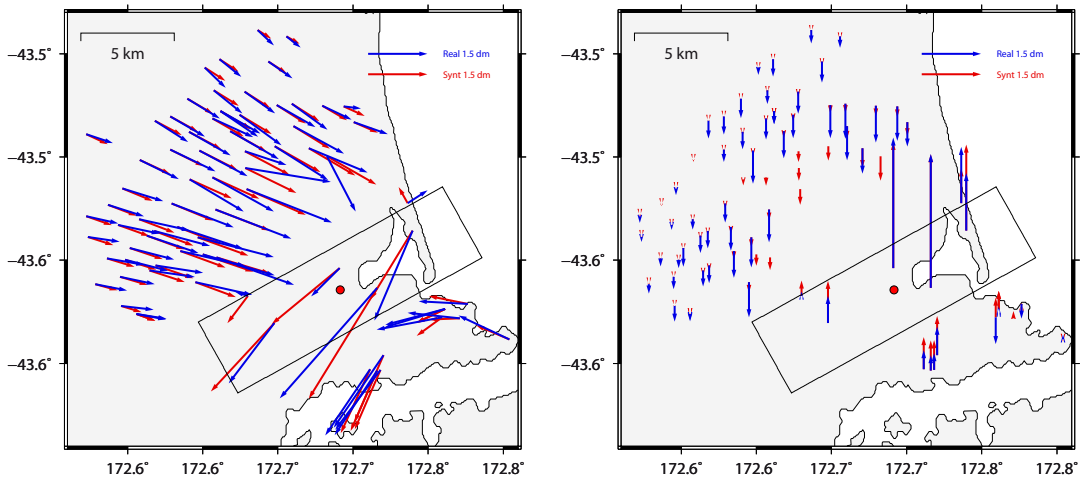

Figure 4.16 Coseismic GPS vector fitting for the single fault model. Left panel: observed (blue arrows) and modeled (red arrows) horizontal displacement corresponding to the kinematic rupture model shown in Figure 4. Right panel: observed (blue arrows) and modeled (red arrows) vertical displacement. In The black rectangulat frame indicates the fault geometry (projected into the surface), while the red dot is the epicentral location (Bannister *et al.* 2011).

The local STF of each subfault is represented by three triangular functions of 0.6 s duration with an overlapping of 0.3 s. The maximum allowed duration of slip for a subfault is thus 1.2 s. The results of this inversion are provided in Figures 4.14-4.15-4.16-4.17. The dislocation model that we retrieved (Figure 4.14) is characterized by a large patch of slip, localized NE of the hypocentre, with a maximum slip value of about 4.2 m. The average slip on the fault is 0.55 m that corresponds to a seismic moment of about 2.8 x 10^{25} dyne cm. The rupture velocity

is characterized by a slip weighted average value of 1.9 km/s s (to compute this average value we used a weighted linear regression between distance of any sub-faults and rupture time; the weight is given by the slip value). The source time function has a total duration of about 7 s, and is characterized by 2 main picks at 3 and 6 s (Figure 4.14).

Although the general fit between real and synthetic data is quite good for all used data (strong-motion, figure 4.15; GPS, figure 4.16; InSAR, figure 4.17), looking at the section in the direction of minimum variation of the InSAR fringes (c-d section in figure 4.17) it is possible to conclude that the source model derived using a single fault plane is not able to explain the complexity of the real data in the area west of the Avon-Heathcote estuary. We therefore increased the complexity of our model adding a second fault plane.

As for the previous case, even for the two faults model we first inferred the geometry and position of the two fault planes, adopting the same strategy followed for the single fault model. Thus, according to the geodetic coseismic data distribution (InSAR and GPS data) we first defined the exploration intervals for the different parameters and then we performed the inversion searching for the strike, dip, average rake and fault center of the two faults.

In particular, the exploration interval for the strike parameter, for the second fault plane included in our modeling was mainly suggested by the curvature in the NNE direction of the InSAR data (track 335). Moreover, while the center of the largest plane was fixed like in the previous case (single fault model) at the hypocentre location provided by Bannister *et al*. 2011, the fault center of the second fault plane was instead explored.From the inversion of the InSAR and GPS data, we found a first plane having a strike of about 60° and a dip of 68°, results that are very similar to the single fault model, and characterized by a prevalent strike-slip movement with a small reverse component.

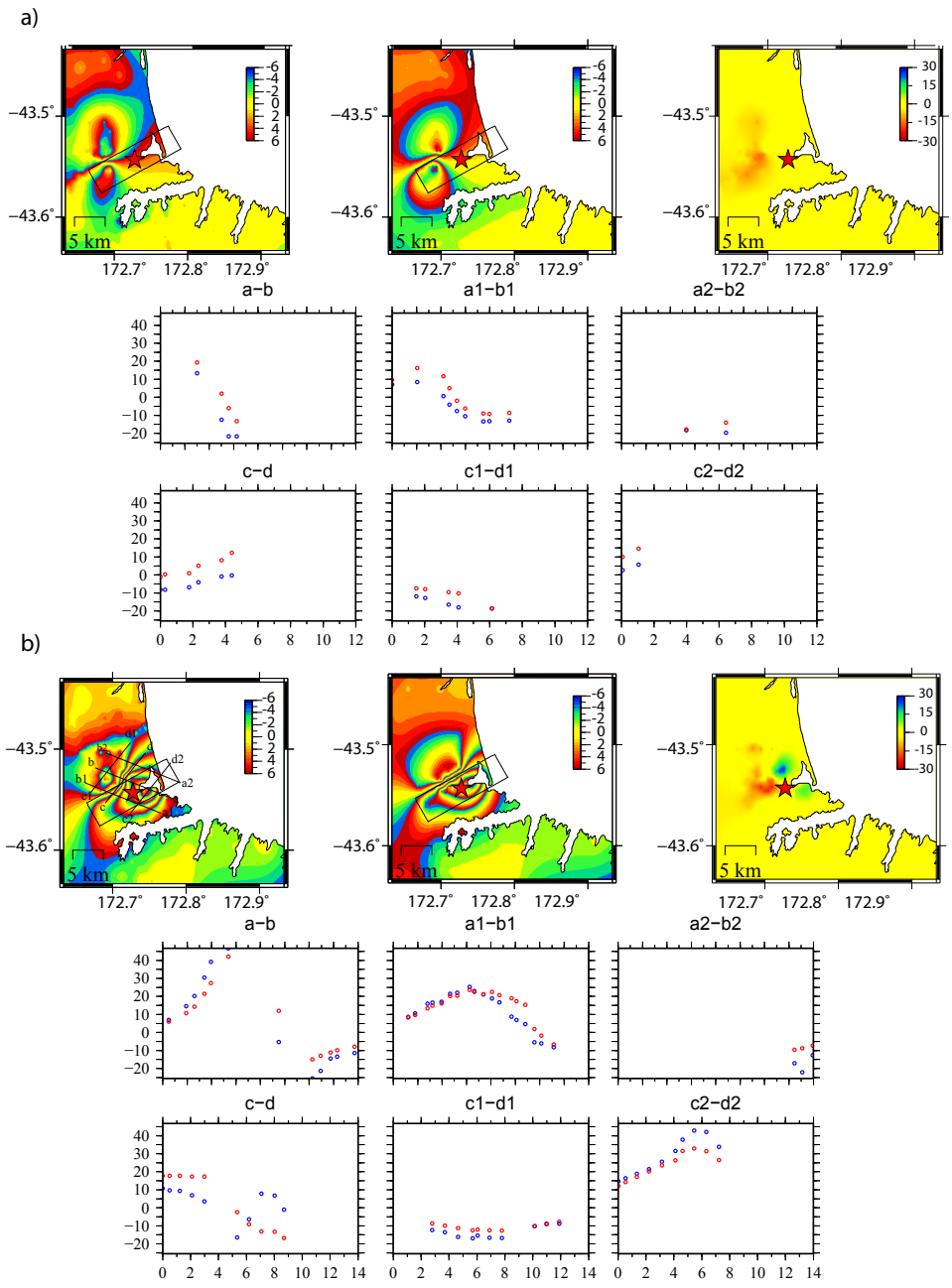

Figure 4.17: Observed (left), modelled (centre) and residual (right) SAR interferograms based on the single fault plane model, for the Christchurch earthquake. The panel a and b represent the 336 and 335 used tracks, respectively. Also shown, sections across the interferograms. The location of the sections are shown on the observed interferograms of panel b.

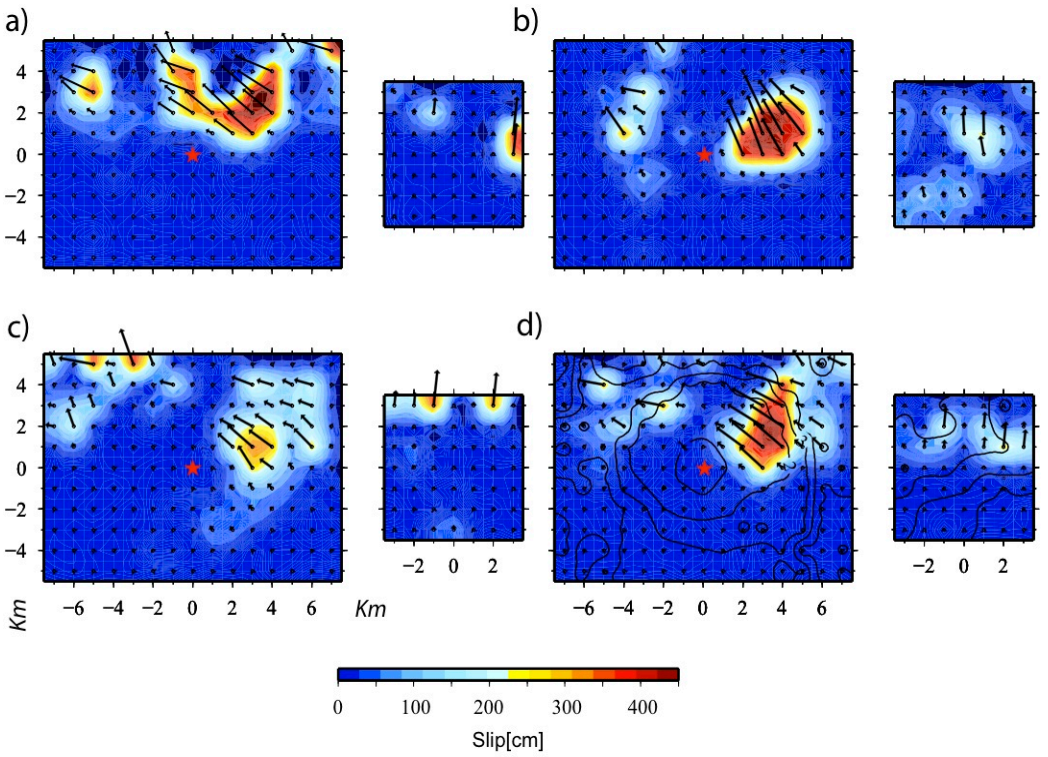

Figure 4.18 Slip maps from the inversion of real data, for the two fault model. Panels a, b, c and d display the slip maps for the GPS, InSAR, strong-motion and joint inversions, respectively. The joint inversion combines the three different real data-sets. Black arrows indicate the slip vectors. For the joint inversion, we also show the rupture time as contour lines. The red stars represent the hypocentre location on the fault plane.

The second fault plane has strike and dip equal to 10° and 57° respectively, and a center located about 1.5 km northward of the main fault center, at a depth of 3.7 km. Moreover, in contrast with from the main fault, the second one is characterized by a dominant reverse fault style.To perform the joint strong-motion, GPS and InSAR data inversion for the source kinematics we set the planes extensions to 15x11 km^2 and 7x7 km^2, respectively, discretized by 1x1 km^2 subfaults.

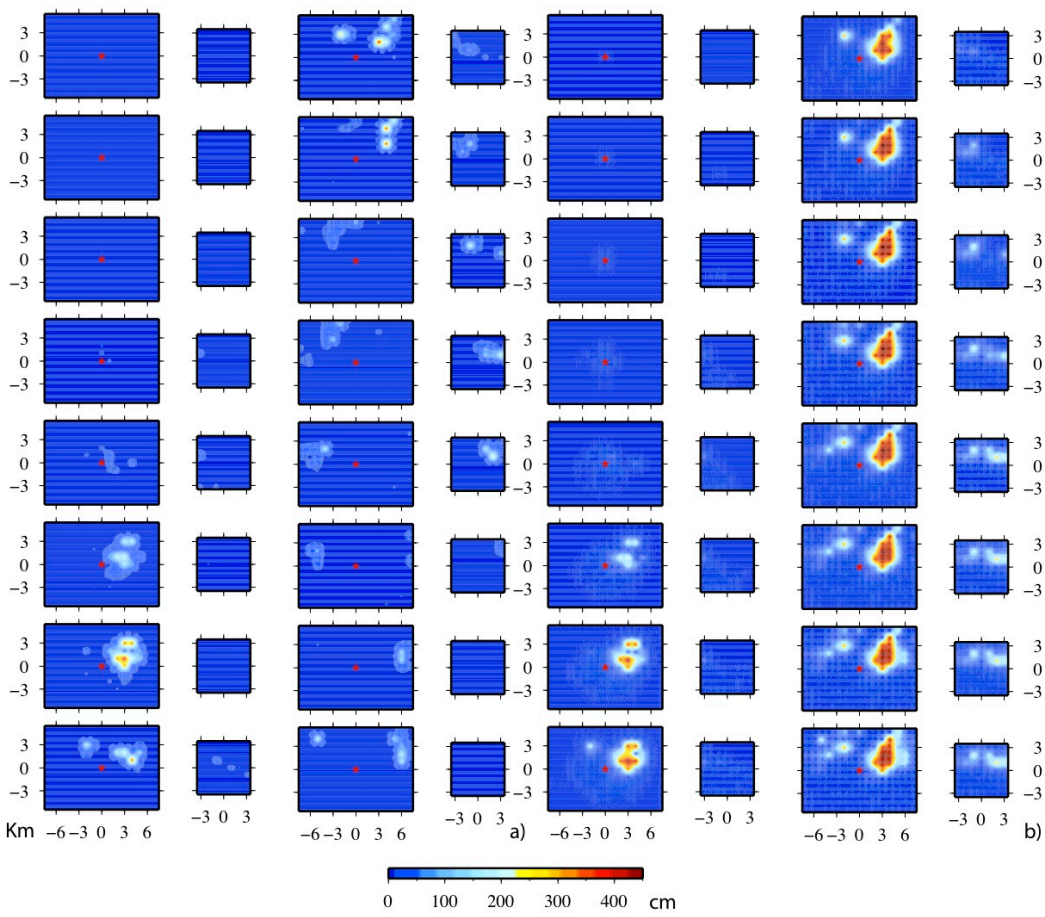

Figure 4.19 Time evolution of the rupture, for the two faults model, from the joint inversion of InSAR, GPS, and strong-motion data given at intervals of 0.4 seconds. The left and right panels show the non-cumulative and cumulative slip evolution, respectively. Red stars correspond to the hypocentre location on the fault plane.

The rupture model obtained from the inversion is shown in figure 4.18, where we report the slip distribution, for the strong motion (panel c), GPS (panel a), SAR (panel b) and joint inversion (panel d), over the two fault planes. The main fault plane is characterized by a dislocation pattern very similar to the distribution inferred for the single fault model. The main patch of slip (maximum slip of about 4.1 m) is again located NE of the hypocentre, while the average slip over the whole fault plane is about 0.5 m. Moreover, an average rake of 150^0 also characterizes the

main plane. The second plane is instead characterized by a lower average slip (about 0.32 m with a maximum value of about 2 m) and shows a main reverse movement (average rake about 90^{o}). The global average slip over both fault planes is about 0.45 m corresponding to a seismic moment of about 3.0 x 10^{25} dyne cm (i.e., Mw 6.2). Most of slip in our rupture model is concentrated between 2 and 5.5 km depth. This result is in agreement with the lack of superficial evidence of the rupture plane and with the fringes shape, highlighted especially from the 335 track.

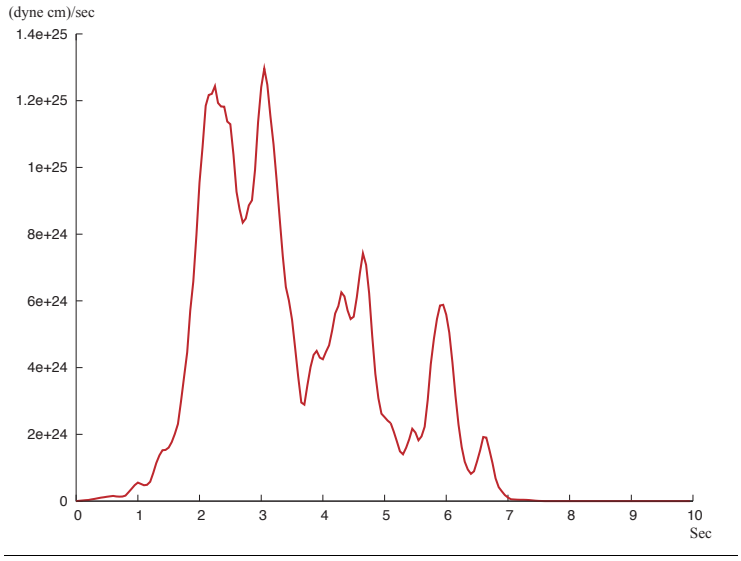

Figure 4.20: Global Source Time Function (GSTF) for the two faults plane model obtained from the joint inversion of InSAR, GPS and strong motion data. The GSTF depicts the evolution of the moment-rate with time.

The rupture velocity has a slip weighted average value of about 1.9 km/s. Analyzing the rupture-times distribution (Figure 4.14 panel d), we infer that, on the main fault plane, the rupture front accelerates at the beginning and then its speed is reduced. Moreover, the rupture front acceleration was higher on the right side of the fault plane.

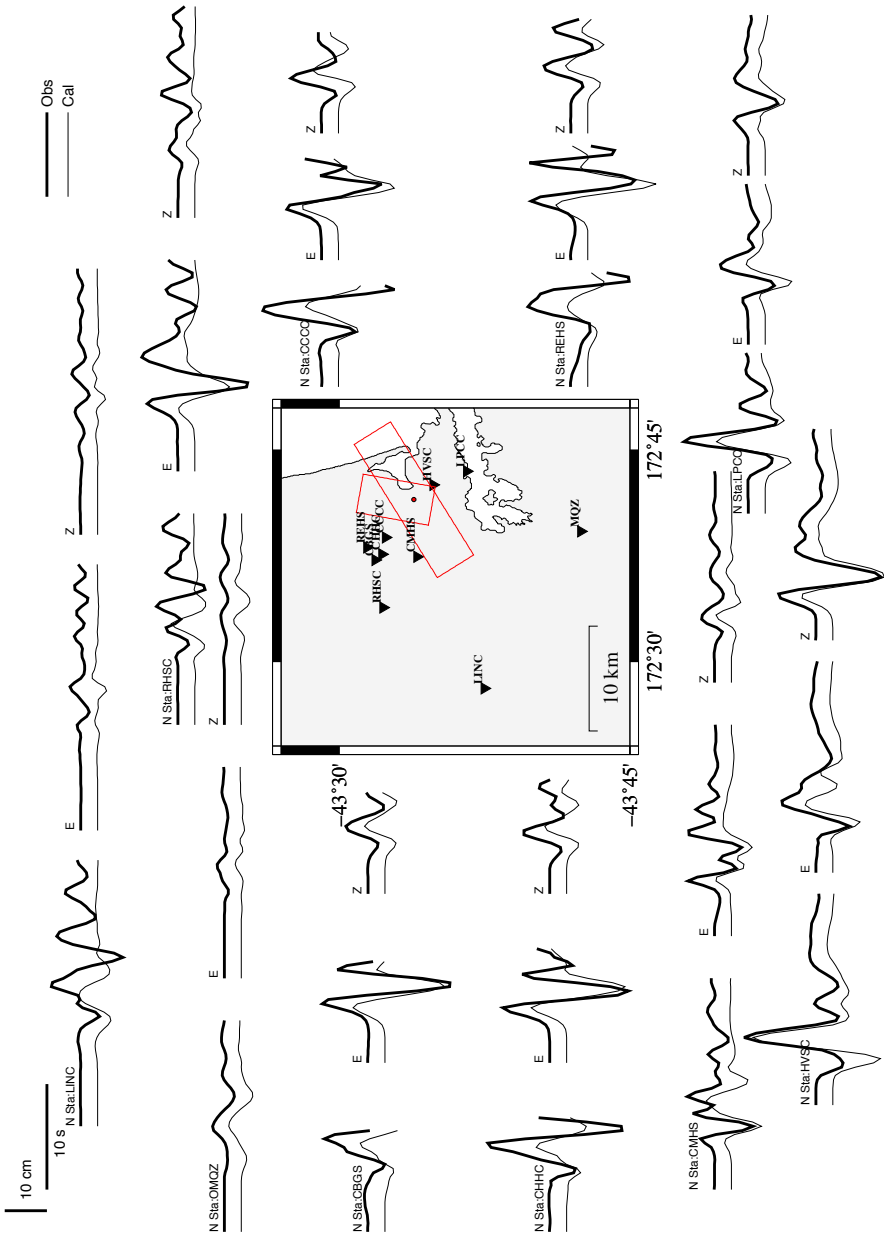

Figure 4.21 Real (thick lines) and synthetic (thin lines) computed for the two fault planes model (red box), ground-displacement strong motion records for the north–south, west-east and up-down component, respectively. Data are band-pass filtered in the 0.1- 0.5-Hz frequency range. The panel in the middle shows the source-receiver and the fault plane geometry (surface projection) used for this analysis.

The rupture duration of the whole faults system lasted about 7 s (Figure 4.18 panel d), like for the single fault model. This observation indicates that the second fault plane broke at the same time as the first one. In figure 4.19 we provide the snapshots, for the non-cumulative (panel a) and cumulative (panel b) slip, at intervals of 0.4s describing the time evolution of the rupture. It is possible to observe that appreciable values of slip appear 1.6 s after the origin time, while the final slip pattern on the first plane is obtained after 5.2 s. Moreover, the second fault starts contributing to the breakage after about 4 s from the nucleation time.

The source time function for this model is characterized by the presence of three peaks (figure 4.20), the main of which appears at about 2 s and is associated with the main slip patch (this first peak is very similar, for shape and amplitude, to that which characterizes the global source time function for the single fault model); the second peak at about 4 s is due to the rupture of the second fault, instead.

Looking at the rupture models obtained from the separate inversions of the single data sets (Figure 4.18), it is possible to conclude that a second fault plane is required, mostly by the InSAR data. The RMS misfit function is markedly improved for the InSAR data, passing from 0.42 for the single fault plane to 0.27 for the two faults model (see also figure 4.23).

Finally, another important result is observed from the residuals analysis on the InSAR data. The introduction of a second fault plane, to model the complex fringes shape near the rupture zone, leads indeed to a clear reduction of the maximum residuals value (from 30 cm for the single fault model to 10 cm for the two-faults model) for both the 335 and 336 tracks (see figures 4.17 and 4.23). Moreover, we found an offset of about 0.1 and 0.3 cm for the track 335 and 336, respectively; values that are consistent with 1.5 cm expected from the initial analysis performed with the GPS data.

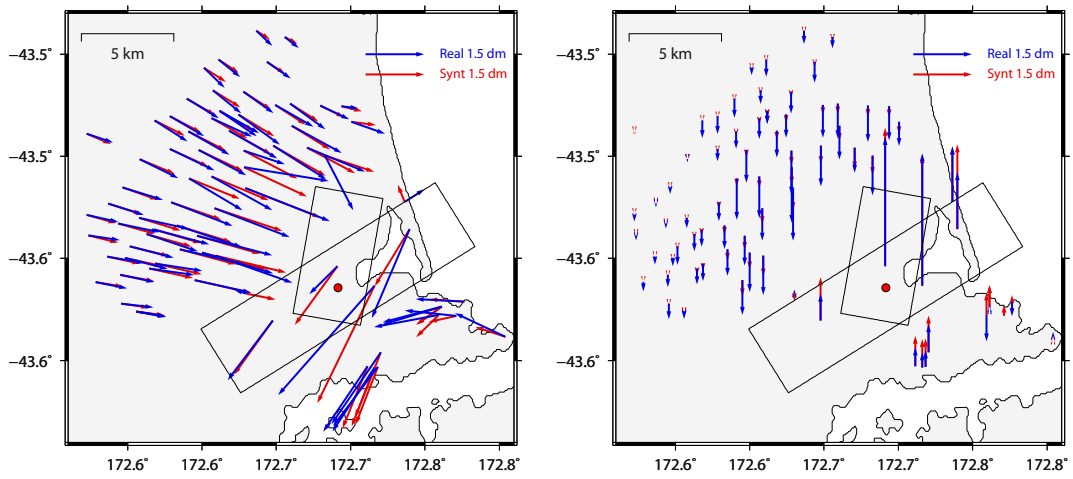

Figure 4.22: Coseismic GPS vector fitting for the two faults model. Left panel: observed (blue arrows) and modelled (red arrows) horizontal displacement corresponding to the kinematic rupture model shown in Figure 8, panel d. Right panel: observed (blue arrows) and modelled (red arrows) vertical displacement. The black rectangular frames indicate the fault geometry (surface projection), the red dot the epicentral location (Bannister *et al.* 2011).

We tested the 1 fault and two fault models both with the restricted (76 stations) and complete (203 stations) GPS data-sets, but it did not made much difference (see Table 1). Another point that needs to be considered is the evaluation of the statistical meaning of models described by a different number of parameters, when the same data sets are used. This study can provide an independent way to choose between the models with one or two fault plane. This analysis is addressed by the corrected Akaike Information Criterion (AICc) for model selection Akaike (1974). This criterion sets that, among various models with different parameters number, we have to choose the one that minimizes the function:

4.2

$$AICc = N \cdot \ln(2\pi E) + \frac{N(N+P)}{N-P-2}$$

where, E represents the misfit value, N the number of data and, finally, P the

number of parameters.

rms	InSAR	GPS (76 stations)	GPS (203 stations)	Strong Motion	Joint
1 Fault model	0.42	0.39	0.77	0.62	0.59
2 Faults model	0.27	0.35	0.72	0.61	0.53

Table 4-2: Root Mean Square (RMS) values from the inversion analysis. In the table we report the different RMS values obtained from the inversion of any separate data-set (InSAR, GPS and Strong-motion) and for the joint inversion (Joint). Results are listed for the two source models studied in this paper. Moreover, for the GPS data two different cases, corresponding to the 76 selected GPS stations and to the complete data-set, are reported. The joint RMS is obtained combining InSAR, strong-motion and selected GPS data.

To search for the minimum of the AICc corresponds to finding the best compromise between fit quality and simplicity of the model.

The results of the Akaike test show very clearly how the misfit improvement obtained for the geodetic coseismic deformation data, from a statistical point of view is sufficient to warrant the introduction of the second fault plane, and so for the introduction of a greater number of parameters. The same however is not true for the strong-motion data. These results, in any case, can be justified for the narrow frequency band used for the strong-motion data inversion, which clearly is not sufficient to reconstruct the rupture complexity.

4.5.1 Resolution test

To assess the resolution associated with the different data sets and evaluate the advantages of the joint inversion, we present here the application of the inversion scheme to the synthetic data.

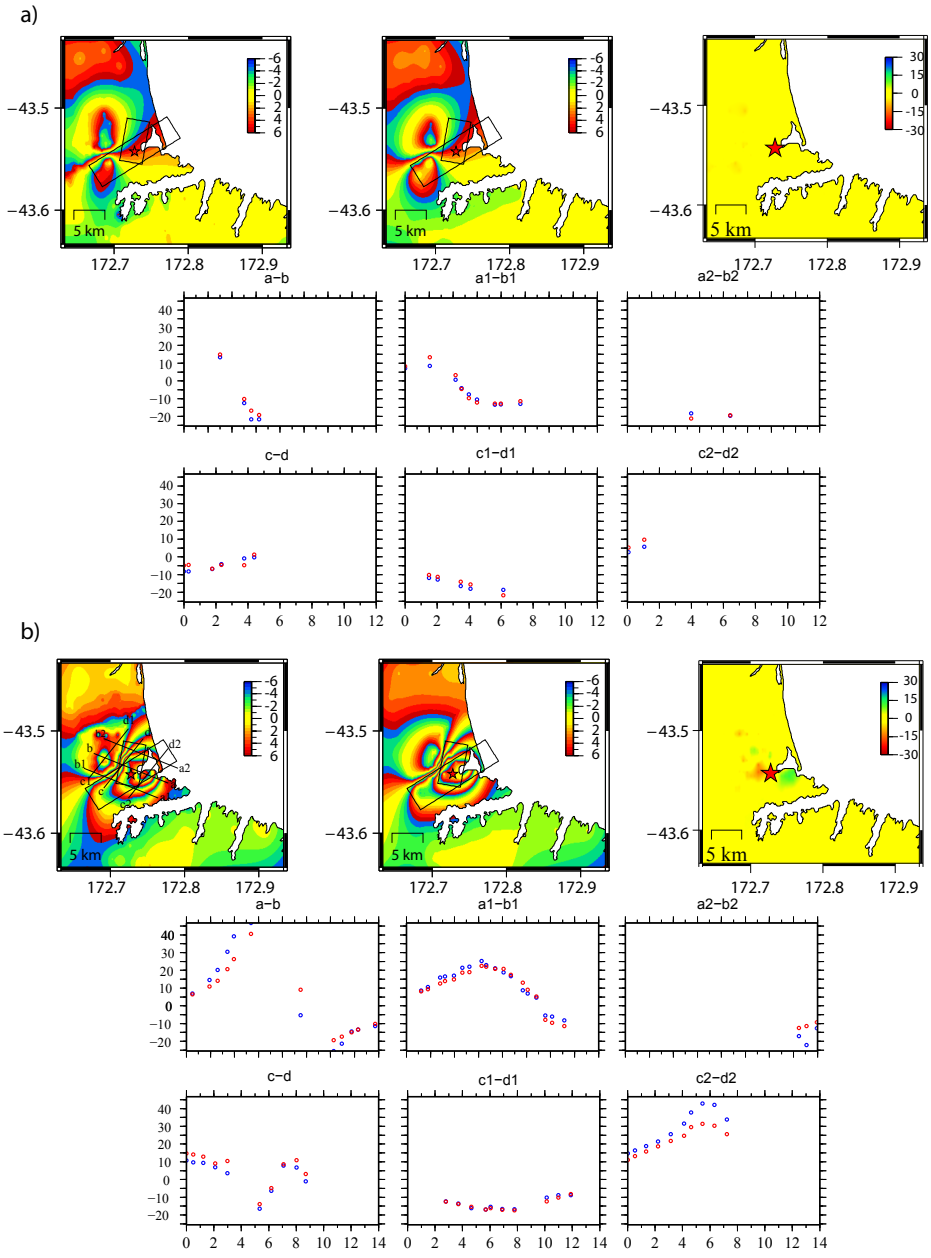

Figure 4.23: Observed (left), modelled (centre) and residual (right) SAR interferograms based on the two fault planes model, for the Christchurch earthquake. The panel a and b represent the 336 and 335 used tracks, respectively. Also shown, sections across the interferograms. The location of the sections are shown on the observed interferograms of panel b.

This test allows to study the performances and limitations of the algorithm and to analyze its spatial and temporal resolution for the real data. For this test we only used the two faults model and the same conditions as for the real case.

I will describe now the source model that I used to compute the synthetic data. In particular I used the slip distribution shown in figure 4.24, panel a. Four asperities of different shape and dimension (a1, a2, a3, a4), three on the main fault and one on the secondary fault characterize this model. These asperities were located at strategic points of the fault, because we want to see if they are actually resolved by the data. The total seismic moment associated with this slip distribution is equal to $3.0x10^{25}$ dyne cm. The rake angle is uniform and set to 110°, a value that represents a good compromise between the two findings obtained for the two fault planes from the inversion of the real data.The rupture velocity is uniform on both planes (2.0 and 1.8 km/s, respectively) except on the slip patch where the velocity rupture increases to 2.7 km/s; so we have a total average rupture velocity over the two fault plane of 2.2 km/s. Moreover, the rupture initiates at the same hypocentre location as for the inversion of the real data. A normally distributed random noise was finally added to the synthetic data.The random noise had a standard deviation of 0.1. Figure 4.24 (panel b, c, d, e) presents the slip distribution obtained from the inversion of both separate and joint data sets. Concerning the InSAR analysis we performed the joint inversion of the two available tracks (335-366). The InSAR data allow finding quite well the position and shape of the asperities a1, a2 and a4 (see panel b figure 4.24), but they are not able to locate the asperity in the deeper part of the main fault. Furthermore the asperities a1 and a2, which are separated in the initial model, seems to be connected each other in the slip distribution retrieved through the inversion, showing a limit in the resolving power of these data.

As in the case of the InSAR data, the GPS data identify the asperities a1, a2 and a4 (see panel c figure 4.24). Again, the shape of the asperities is only approximately retrieved and then also this kind of data has a lower resolution in the lower part of

the model. Compared to InSAR however, the shape of the asperities a1 and a2 is better resolved, though the two asperities appear again linked. Differently from the geodetic data, the inversion of strong-motion data provides a rupture in which all the asperities are quite correctly identified both for their shape and position (see panel d figure 4.24).

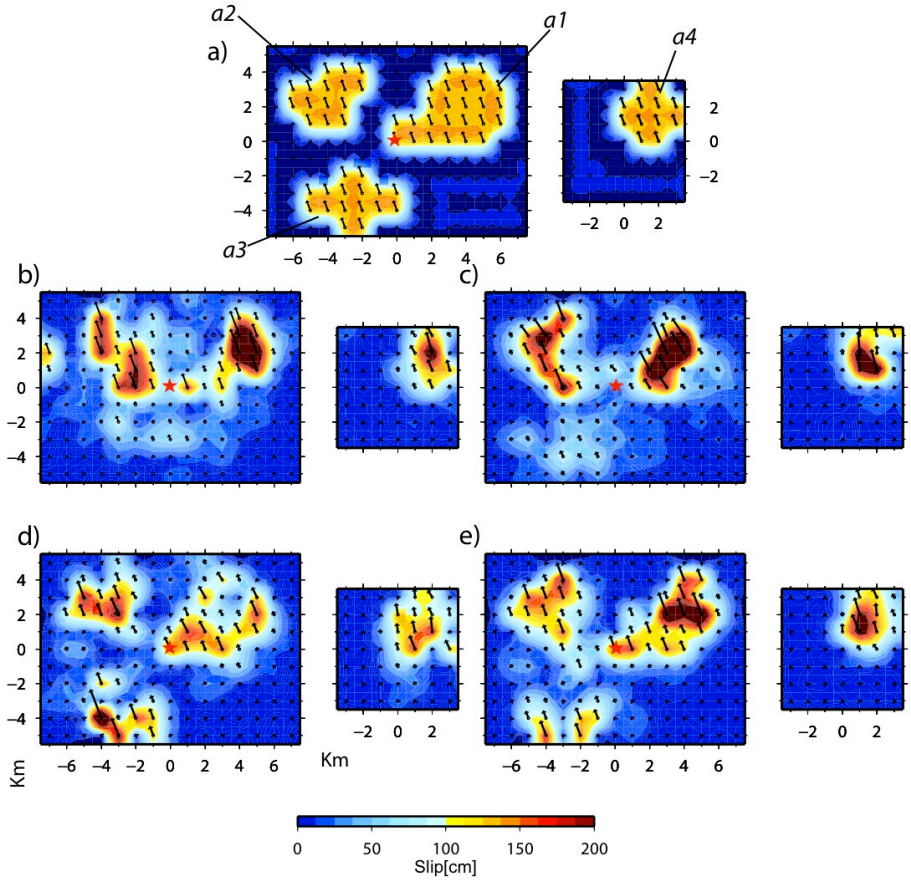

Figure 4.24: Slip maps from the resolution tests. Panels a, b, c, d and e correspond to the slip maps for the synthetic model (two fault planes), and then for the GPS, InSAR, strong-motion and joint inversions, respectively. The joint inversion combines the three different synthetic data sets. The black arrows indicate the slip vectors, while the red star represents the hypocentre location.

Moreover, the strong-motion data also provides a good resolution of the deepest

part of the main fault, which is most likely due to the relative shorter distance of all the stations from the source. Finally, the joint inversion (see panel e figure 4.24) of the three data sets shows a very good improvement on the resolution of the initial slip model with respect to the single data-sets cases. It should be noted that the seismic moment inferred from the InSAR, GPS, strong-motion and joint inversions, though in a general good agreement with the starting model, is slightly overestimated. Concerning the rupture velocity, the joint inversion provides an average value of 2.0 km/s, slightly lower than the average value of the initial model (2.2 Km/s).So these tests allow us to conclude that the main features retrieved from the joint inversion of real data are quite well resolved.

4.5.2 Errors analysis

We evaluated errors estimates on our final model following the approach proposed by Emolo & Zollo (2005). For each subfault we focused on one by one of the 5 parameters defined on it (i.e., rupture time, rake, and the three moment values).

Fixing all the model parameters at their best values, we perturbed the selected parameter around its best p_{best}. Then, for each $p \in [0.9p_{best}; 1.1p_{best}]$ we evaluated the misfit E(p), accounting for all the available data and finally we computed the function

4.3

$$\mathrm{pdf}(p) = Ce^{\left[-\frac{E^2(p)}{2\sigma_0^2}\right]}$$

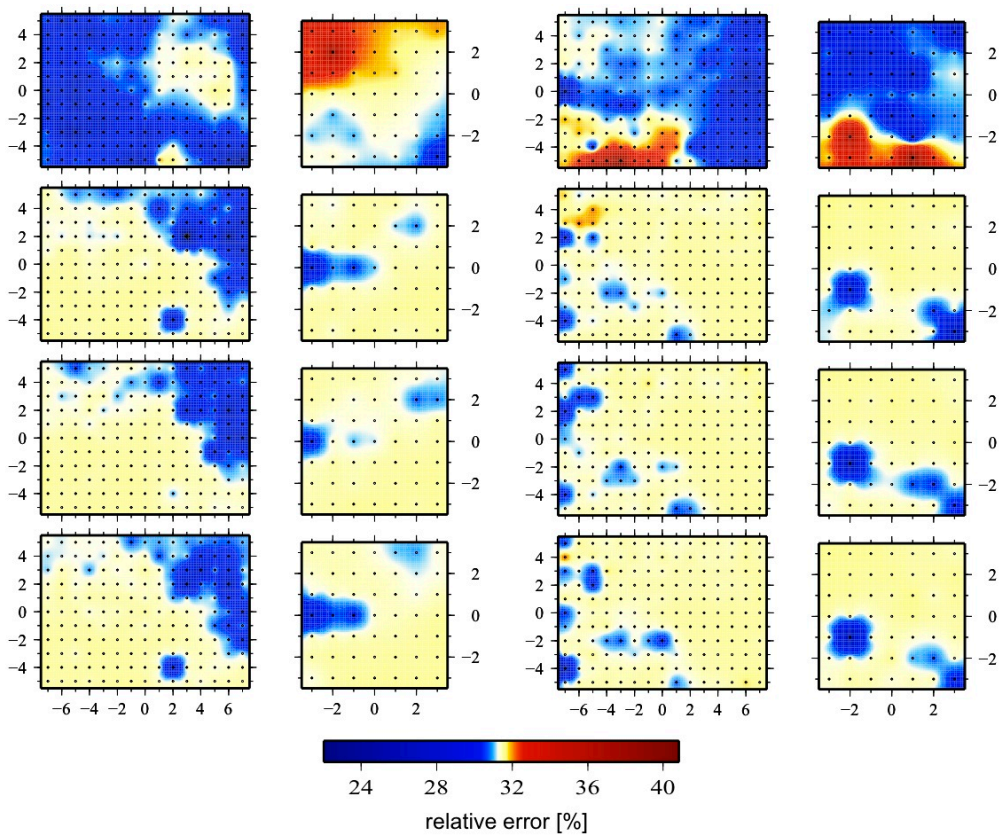

Figure 4.25: Relative error distributions for the InSAR (left) and GPS (right) data inversions. From the top to the bottom are displayed the relative errors for the slip vector and for the 3 moment values, corresponding to the three triangular functions whereby we discretized any local source time function.

where the normalization constant C is given by:

4.4

$$C = \frac{1}{\int_{0.9p_{best}}^{1.1p_{best}} e^{\left[-\frac{E^2(p)}{2\sigma_o^2}\right]} dp}$$

In this way the function *pdf*(*p*) assumes the meaning of a marginal probability distribution function for the parameter p_{best}. The parameter σ_0^2 in the two previous

equations is the unknown variance of the misfit function, and accounts for errors both in the modeling and in the data. It determines the shape of the *pdf* and, in the present case, it has to be assigned arbitrarily, according to the best-fit model variance.

We can characterize these probability distribution functions by their overall widths.

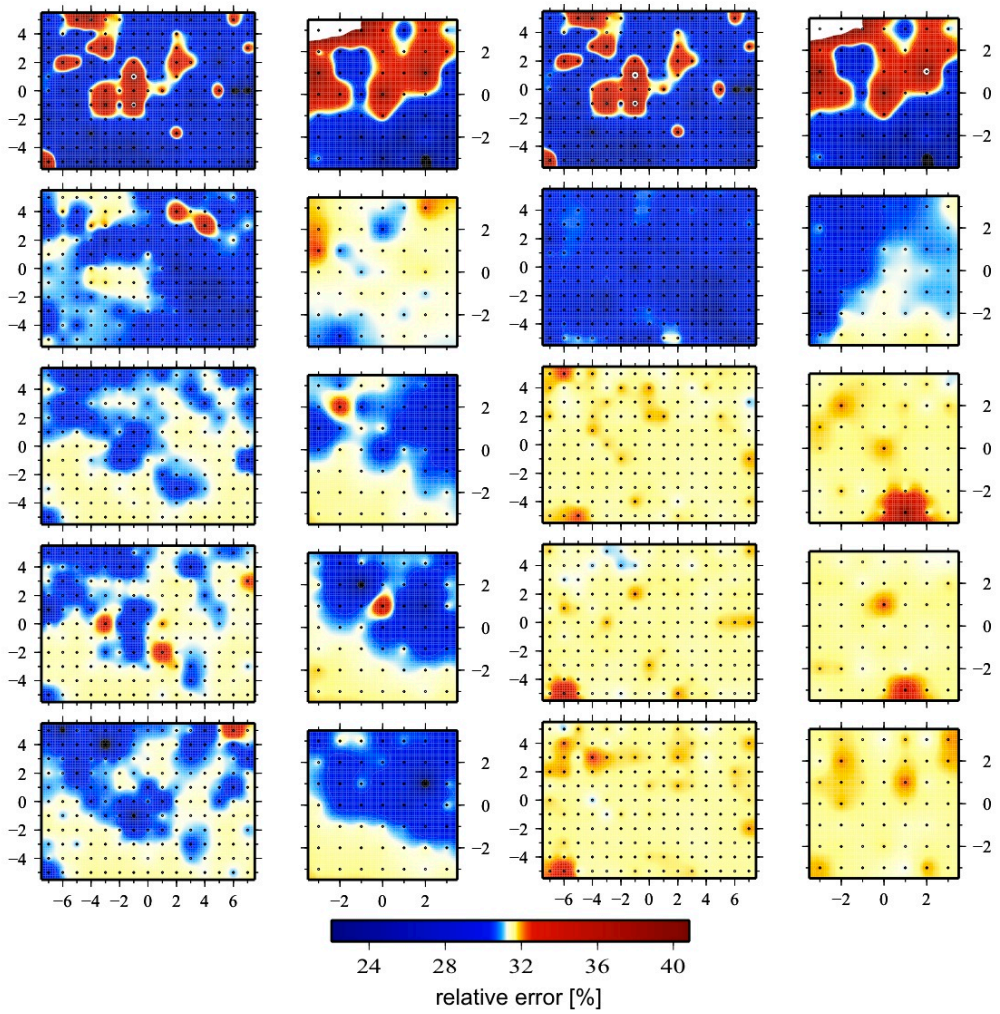

Figure 4.26: Relative error distributions for the strong-motion data (left) and joint (right) inversions. From the top to the bottom are displayed the relative errors for the onset-time, slip vector and for the 3 moment values, corresponding to the three triangular functions whereby we discretized any local source time function.

One way of measuring the width of a distribution is to multiply it by a function that is zero near the center of distribution and that grows on either side of center. The area under the resulting function gives a quantitative measure of the width of the distribution. If one chooses the parabola $(p- p_{best})^2$ as that function, then this area gives the variance σ^2 of the distribution.

4.5

$$\sigma^2 = \int_{0.9p_{best}}^{1.1p_{best}} (p - p_{best})^2 \cdot pdf(p)dp$$

According this approach we computed the relative errors for all the model parameters and both for separate and joint data sets. The results of this analysis are shown in the figure 4.25 and figure 4.26. We generally find a relative error of about 25-30 %, with the largest errors associated with the rupture times. This last result is consistent with the slight underestimation on the velocity rupture we found from the resolution test.

4.6 Discussion and Conclusion

The Canterbury Plain over the last two years has been characterized by two main seismic events: the September 4, 2010, Mw 7.1 Darfield earthquake and the February 21, 2011, Mw 6.2 Christchurch earthquake. The latter occurred in an area characterized by a large aftershock activity related to the Darfield earthquake and by an increase of the Coulomb static stress induced by the previous earthquake (Zhan *et al.* 2011). All this information seems to suggest that the Darfield earthquake may have influenced the occurrence of the Christchurch event.

A large quantity of data of different nature, e.g. InSAR, GPS, and strong-motion data, are available for the Christchurch earthquake. In particular, the coseismic

geodetic data suggest a complex geometry for the source, as in the case of the Darfield event (Elliott *et al*. 2012, see figure 4.32) that occurred in the western part of the Canterbury plains.

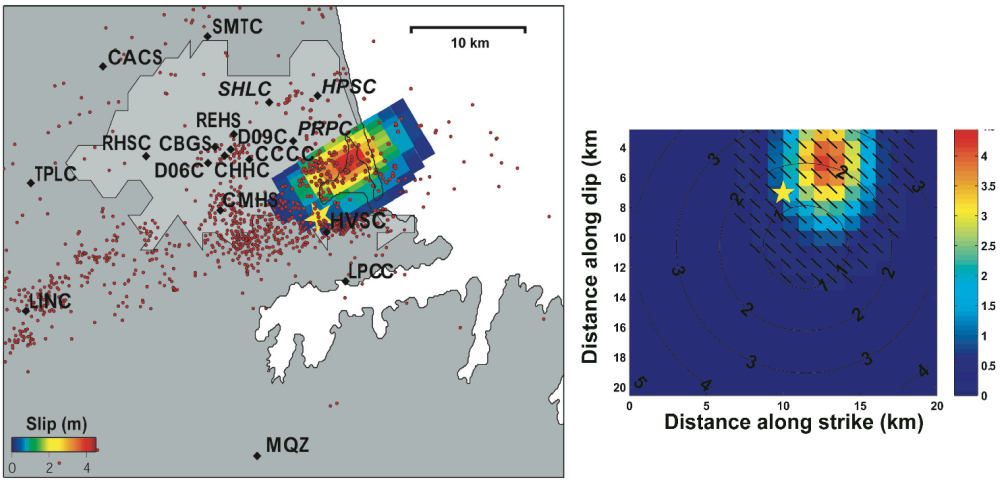

Figure 4.27: Kinematic rupture model retrieved by Holden et al., 2011.

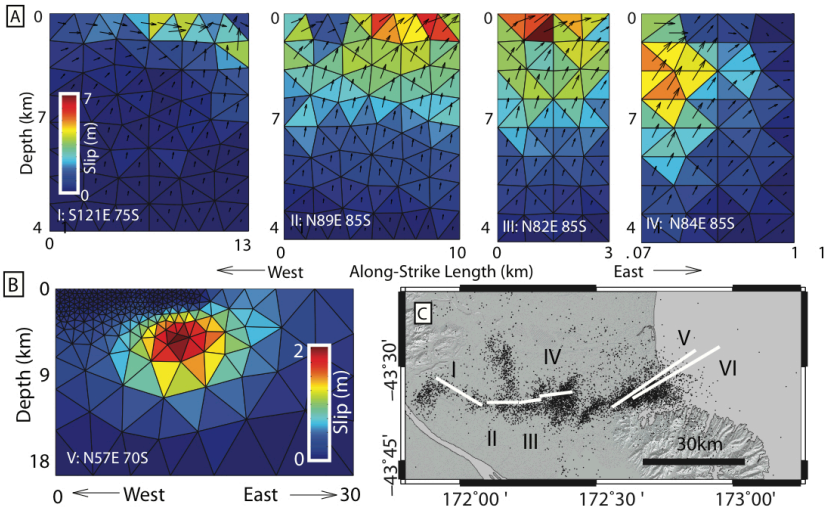

Figure 4.28: Kinematic rupture model retrieved by Barnhart et al. 2011. A: rupture model for the Darfield earthquake; B: source model for the Christchurch earthquake.

We used the non-linear inversion method proposed by Delouis *et al.* (2002) to

invert the available data sets in order to determine the geometry of the fault plane(s) and the kinematics features of the seismic source for the Christchurch event.

Adopting a single-fault model, we found a plane striking N59° and with a dip angle of 66°. This result is consistent with the inferences obtained by Barnhart *et al*. 2011 (strike=59^o and dip=64^o), see figure 4.28 and by Beavan *et al.* (2011) (strike=59^o and dip=66.5^o), see figure 4.29, analyzing the GPS data. The faulting mechanism is prevalently strike-slip with a small reverse component (average rake = 150^o), quite consistent with the solution reported in the catalogues GCMT, while differences mainly for the rake are found with respect to the GeoNet catalogue. Our average rake angle is consistent to that found by Beavan *et al.* (2011) but is different to that by Barnhart *et al*. 2011 ($\sim 70^o$).

The kinematic rupture model found in this case is very similar to those provided by Beavan *et al.* (2011) and Barnhart *et al*. 2011 and it is characterized by a main slip patch located NE of the hypocentre. Compared to the Beavan *et al.* (2011) and Barnhart *et al*. 2011 models, however, our model presents a much more localized slip patch characterized by a maximum slip value of about 4.3 m, larger than 2.5 m found by Beavan *et al.* (2011) and 2.1 m found by Barnhart *et al*. 2011.

Our maximum value of 4.3 m is in any case very close to that retrieved by Holden (2011), 4.2 m, inferred from the inversion of the strong-motion data (figure 4.27).

Compared to the Holden (2011) kinematic model, which prescribes a total rupture duration of about 4s, we found a lower average rupture velocity, which leads us to have a total duration of the rupture of about 7 s. Then, we moved to consider a more complex fault model as also done by Beavan *et al.* (2011) (figure 4.29), Atzori *et al*. 2012 (figure 4.30), Beavan *et al*. (2012) (figure 4.31) and Elliott *et al.* (2012) (figure 4.32). Our geometries, retrieved from the inversion of InSAR data, are quite different from the two-fault models proposed in previous researches even if they share some features with both already published models.

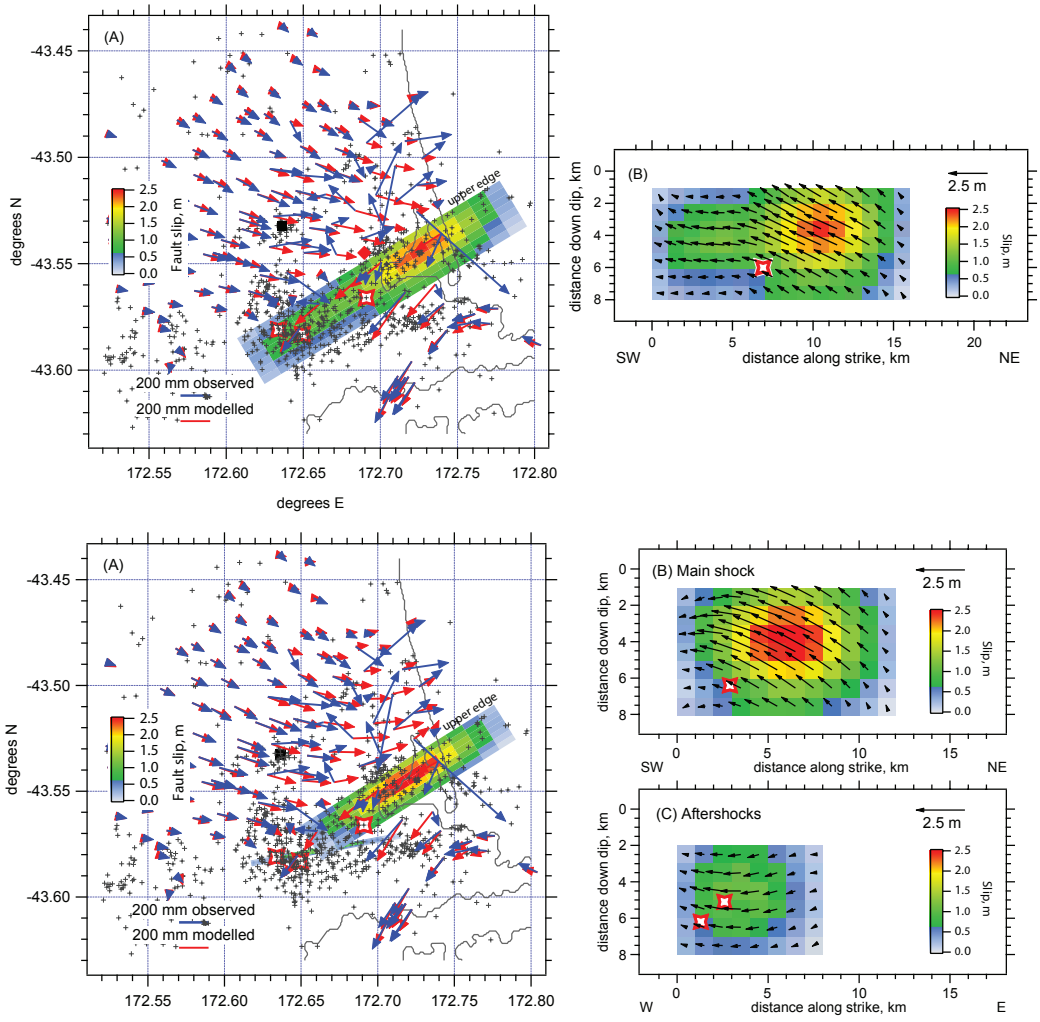

Figure 4.29: Kinematic rupture model retrieved by Beavan et al., 2011.

In particular while our main plane is similar to that of Beavan *et al.* (2011), the two models completely differ for the second plane. In fact, the second plane by Beavan *et al.* (2011) is characterized by a strike-slip mechanism and is located south of the main plane (in this work the position of the second fault plane was obtained from

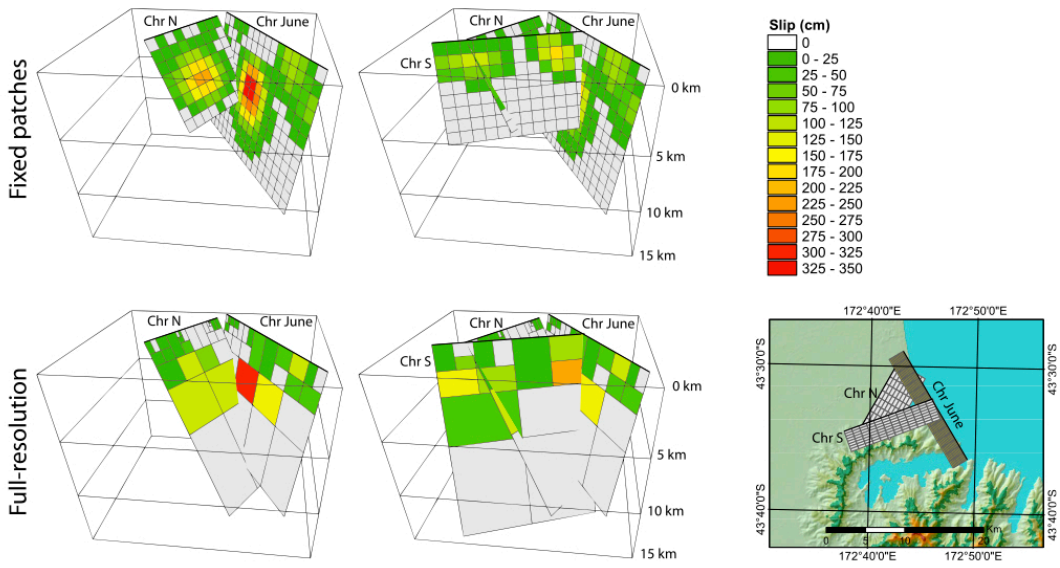

Figure 4.30: Kinematic rupture model retrieved by Atzori et al. 2012. In figure have been reported the two fault plane related to the Christchurch earthquake and the fault plane related with the 6 June 2011 aftershock.

the aftershock distribution), while in our model the second plane is located north of the first and is mainly associated with a reverse mechanism.On the other hand, our model is similar to those proposed by Elliott *et al.* (2012) and Atzory *et al*. (2012) who studied the InSAR data. These models share a quite similar geometry with two planes having different strike, the lower strike fault plane characterized by a dominant reverse movement and the higher strike plane with a mainly strike-slip mechanism. The two models strongly differ for the slip dstribution. In fact, the Elliott *et al.* (2012) and Atzori *et al*. 2012 rupture models prescribe the large part of the total seismic moment as associated with the reverse fault plane with the lower strike while in our model, most of the seismic moment is instead associated with the fault plane having higher strike and strike-slip mechanism, which is also, in our case, the plane containing the hypocentre of the event.

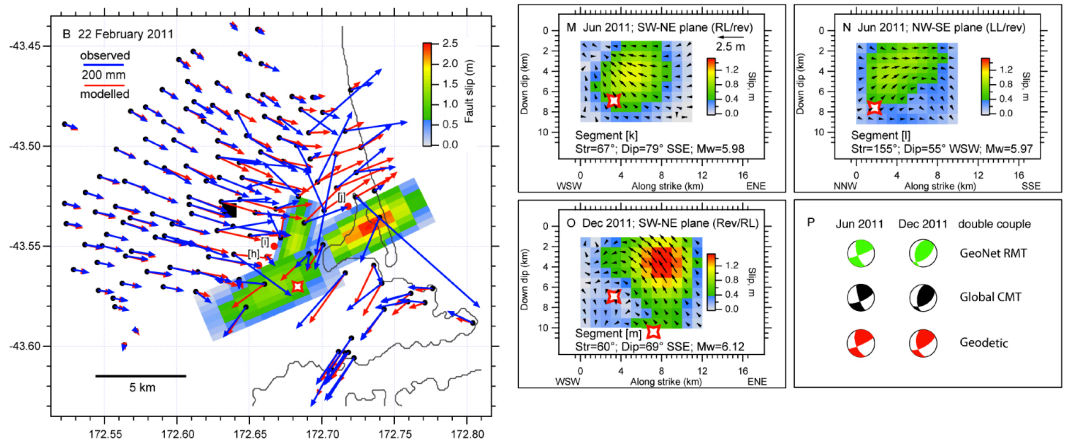

Figure 4.31: Kinematic rupture model by Beavan *et al.* 2012.

Compared to the fault geometry proposed in Beavan *et al*. 2011, in a following work (Beavan *et al*. 2012) the author introduced in his model a third fault plane located north of the main fault plane. This fault plane shows a good agreement for geometry, position and mechanism compared to our northern segment. The possibility of introducing a third fault plane was also investigated in this work, but was rejected because it did not report any improvement in misfit compared with the two fault models, for all of the data-set used. On the other hand already in Beavan *et al*. 2011 the author noted that the introducing of a second segment, located south of the main one, did not lead to any statistically significant improvements on the model.

Concluding, we found that the addition of the second fault plane in our model for the Christchurch earthquake, leads to a marked improvement in the fit of the InSAR data (track 335), even if it does not provide a substantial improvement in fit between real and synthetic data for the strong-motion and GPS data sets. The second fault plane, however, allows us to reproduce in our synthetic data some complex shape of the InSAR fringes that cannot be explained by a single fault model. Finally, it should also be highlighted how the introduction of the second

fault plane in any case does not lead to a degradation of the RMS for both the GPS and strong-motion data.

Furthermore, another point that seems to endorse the choice of a complex fault geometry for the Christchurch earthquake is that also the Darfield earthquake is characterized by a complex faulting geometry with the alternation of planes having different strike and whose mechanism changes from strike-slip to reverse (Elliott *et al.* 2012. Beavan *et al*. 2012. Atzori *et al*. 2012).

The geometry and source model for the Christchurch earthquake retrieved in this work well fit with the regional stress field actually present in the Canterbury plains and characterized by a maximum contraction axis σ^1 of $0^o/115^o$ (Sibson *et al*. 2011, Wallace *et al*. 2007) (figure 4.5). From this point of view a key role, however, has the uncertain orientation of σ_3 axes. Indeed if the predominant strike-slip event (see figure 4.1) seems to suggest a horizontal σ_3 axis, the simultaneous presence of inverse events in the Canterbury area, may indicate local variation of σ_3. Furthermore, considering the mixture of strike-slip and reverse faulting during the entire Canterbury sequence, it seems likely that the stress field is of the form $\sigma_1 > \sigma_v = \sigma_2 \sim \sigma_3$ with local variance between $\sigma_v = \sigma_2$ and $\sigma_v = \sigma_3$.

Therefore, considering this, we hypothesize that orientations and mechanisms ($150^0$and 90^0 for southern and northern segments, respectively) of two fault planes used to model the Christchurch earthquake are associated to a local rotation from horizontal plane of the σ_3 axes. As suggested also by other authors (Holden *et al*. 2011, Sibson *et al*. 2011, Barnhart *et al*. 2011) it is possible that perturbation of local stress in the Christchurch area could be driven by the presence of the now extinct volcano Banks Peninsula south of the Canterbury plains

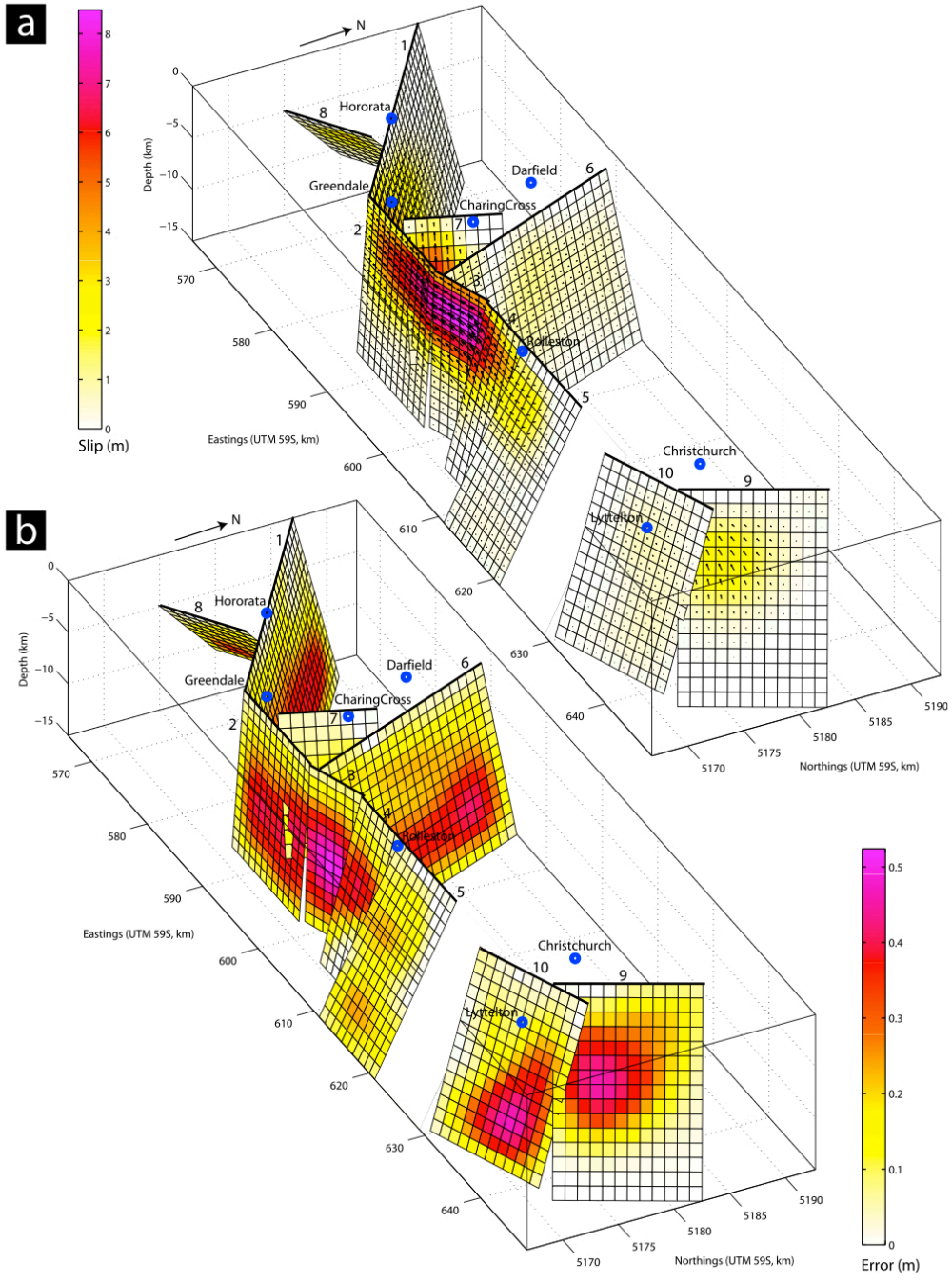

Figure 4.32: Kinematic rupture model retrieved by Elliott et al., 2012.

5 Earthquake Source Kinematics of Moderate Earthquakes From the Inversion of Apparent Source Time Functions

5.1 Introduction

One main target of observational seismology is to estimate the earthquake source characteristics from the recorded ground motion. To this end, various methods aimed at reconstructing source kinematic models from the inversion of seismogram have been proposed during the time (e.g., Beroza *et al.* 1988; Hartzell & Liu 1995; Delouis *et al.* 2000; Emolo & Zollo, 2005; Liu *et al*. 2006; Piatanesi *et al.* 2007; Lucca *et al.* 2012). The kinematic description of the earthquake source, as compared to the dynamic one, has the advantage of using a limited number of parameters, characterizing the source time function, i.e., the final slip and rupture velocity distributions on the fault, the slip duration, the fault geometry and orientation. Nevertheless, even using a simple kinematic description of the source,

the problem of inverting the ground-motion recordings may become strongly non-linear, when considering variable rupture velocity and/or rise-time on the fault. From this point of view, the most important effect is the trade-off between the slip value and rupture-velocity distribution on the fault, which can produce similar effects on the seismic waveforms (Emolo 2001; Emolo *et al.* 2008; Ameri *et al.* 2009).

The method proposed in this work to determine the slip and rupture velocity distributions on the fault plane is based on the inversion of the apparent Source Time Function (aSTFs). The aSTF differently from a local Source Time Function, takes into account also the propagation times between the source and receivers and therefore incorporates the directivity effects of the seismic source; a local Source Time Function represents the slip history for any source in which the fault plane is discretized. The technique used to obtain the aSTF of a seismic event is that proposed by Vallée (2004) based on the analysis of Empirical Green function (EGF). A method based on the inversion of an aSTF, compared to ones where the theoretical Green functions are considered, has the advantage to naturally include the path propagation, anelastic attenuation and site amplification effects which can affect the source parameter modeling if not properly described by numerically computed Green functions. Moreover it also allows performing the inversion at frequencies higher than those generally used in seismograms inversions that, for large magnitude earthquakes, are, at the most, are few Hertz. In this method indeed, the frequency band in which the inversion is performed does not depend on the particular velocity model used but only on the frequency range in which the aSTF have been derived. At the same time the main disadvantage is due to the reliability of the retrieved aSTF for an extended fault rupture, which in turn depends on the availability of an adequate set of Empirical Green Function (EGF) records, which provide an optimal azimuthal coverage of the source. When using a single EGF event, as in the present study it is critical to find the proper range of source-to-site

distance for which the propagation effects from any point on the fault can be adequately approximated by using a single EGF. The EGF devonvolution technique proposed by Vallée (2004) for the computation of the aSTFs of a seismic event in particular is based on the projected Landweber method. This method was introduced in seismology by Bertero *et al.* (1997), with the additional constraint that the area of the aSTFs (which represents the scalar moment of the earthquake) has to remain the same at all the stations.

5.2 The Empirical Green Function Approach

Knowledge of the seismic source requires modeling the propagation between the source and the receiver (Green's functions). Under the hypothesis of linear wave propagation, the Green's functions may also be replaced by the records of small earthquakes occurring on the same fault with the same focal mechanism and the same stress drop, commonly referred to as Empirical Green's functions (EGFs).

The use of small events as EGFs was first proposed by Hartzell (1978). It was subsequently used and developed by Mueller (1985), Fukuyama and Irikura (1986), Mori and Frankel (1990), Ammon et al. (1993), Velasco et al. (1994), Courboulex et al. (1997a), and Ihmlè (1996). The idea is to deconvolve the mainshock from the smaller event (EGF) to obtain a apparent source time function (aSTF) at each considered station. The durations of each aSTF are then examined to retrieve some interesting properties regarding the extent and rupture velocity of the event.

By starting from the representation theorem, for a large earthquake of moment M_1, we can write:

5.1

$$U_i^1(\boldsymbol{x},\omega) = -M_{pq}M_1 ik_q G_{ip}(\boldsymbol{x},\boldsymbol{\xi}_0,\omega)\iint_S f(\boldsymbol{\xi},\omega)e^{-i\boldsymbol{k}(\xi-\xi_0)}d\xi^2$$

where G_{ip} denotes the spatial derivative of the Green function. Here we assume that 1) the Green function G_{ip} is the same for all the points of the fault except for a phase shift $\boldsymbol{k}(\boldsymbol{\xi} - \xi_0)$ due to the varying distance between source and receiver (far-field approximation), 2) the earthquake has a constant mechanism. M is a unit tensor independent of $\boldsymbol{\xi}$ and ω, $f(\boldsymbol{\xi}, \omega)$, the inverse Fourier transform of $f(\boldsymbol{\xi}, \omega)$, is a causal, positive scalar function, monotonically increasing over [0, D], where D is the unknown duration of the source, and constant elsewhere (for more details see Vallée 2004).

For a smaller earthquake of scalar moment M_0, with same location and similar focal mechanism of large earthquake, $f(\boldsymbol{\xi}, \omega)$ can be approximated by

5.2

$$f(\boldsymbol{\xi}, \omega) = \delta(\boldsymbol{\xi} - \boldsymbol{\xi}_0) TF\big(H(t)\big) = \frac{\delta(\boldsymbol{\xi} - \boldsymbol{\xi}_0)}{i\omega}$$

where $TF(H(t))$ is the Fourier transform of the Heaviside function, which leads to

5.3

$$U_i^0(\boldsymbol{x}, \omega) = -M_{pq} \frac{M_0}{i\omega} i k_q G_{ip}(\boldsymbol{x}, \boldsymbol{\xi}_0, \omega)$$

Therefore, by deconvolving equation (4.1) from equation (4.3), we obtain the aSTF, defined as F_θ in the equations:

5.4

$$F_\theta(\omega) = \frac{M_1}{M_0} i\omega \iint_S f(\boldsymbol{\xi}, \omega) e^{-i\boldsymbol{k}(\xi - \xi_0)} d\xi^2 = \frac{M_1}{M_0} i\omega \iint_S f(\boldsymbol{\xi}, \omega) e^{-i\omega \frac{\boldsymbol{u}}{v_\phi}(\xi - \xi_0)} d\xi^2$$

where v_Φ, the phase velocity and **u** the wave propagation direction, are assumed constant. This assumption compels us to study separately each wave type in the EGF analysis. The aSTF is a positive, bounded-support function and its duration

will also depend on the position of the station, the phase, and the rupture velocity but it will of course remain bounded. Another important property of the aSTF is that its integral value is independent of the stations or the wave type used in the deconvolutions and is equal to the relative moment between the mainshock and the EGF.

5.3 Projected Landwebber Method

The deconvolution method of Vallée (2004) is based on the approach of Bertero et al. (1997), who developed a simple method to include positivity and temporal constraints on the aSTFs, based on the Landweber method. It was shown by Bertero et al. (1995) that the latter method was slower but more accurate than conjugate gradient methods.

Called U^1 and U^0 the mainshock and EGF waveform, respectively, the problem is to identify the aSTF F_θ verifying

5.5

$$\left|\left|U^0 * F_\theta\right|\right| - U^1 = minimum$$

or equivalently

5.6

$$U^{0^*} * U^0 * F_\theta = U^{0^*} * U^1$$

(e.g., Bertero, 1989), where U^{0*} is the adjoin operator of U^0. Through mathematical manipulations, equation (4.6) can thus be written as

5.7

$$F_\theta = F_\theta + U^0(-t) * (U^1 - U^0 * F_\theta)$$

In an iterative scheme, the last equation becomes

5.8

$$F_\theta^{(n+1)} = F_\theta^n + \tau U^0(-t) * (U^1 - U^0 * F_\theta^n)$$

where τ is the relaxation parameter which must satisfy the condition $0 < \tau \leq 2/(\sup_\omega |U^0(\omega)|)^2$ and is classically chosen equal to $1/(\sup x |U^0(\omega)|)^2$.

Let us suppose that we know that the aSTF belongs to some closed and convex set C. Then equation (4.8) can be modified as follows:

5.9

$$F_\theta^{(n+1)} = P_c\left(F_\theta^n + \tau U^0(-t) * (U^1 - U^0 * F_\theta^n)\right)$$

where P_c denotes the metric projection on C. In the absence of noise, F^n is shown to converge, but only weakly, toward the expected solution of

5.10

$$\left|\left|U^0 * F_\theta\right|\right| - U^1 = minimum, \qquad F_\theta \in C$$

Bertero et al. (1997) defined C as the set of nonnegative causal functions that are zero for $t > D$. However, we can be even more restrictive and let C be the set of nonnegative causal functions that are zero for $t > D$ and for which the integral over $[0D]$ is equal to M_1/M_0. It can be immediately verified that the newly defined set that we call Cm is closed and convex. We now must define the projection P_{Cm} itself

in order to compute equation (4.9). Given a function h, it can be shown that $P_{Cm}(h)$ can be naturally computed, that is, we essentially add a proper, additive constant to h to derive $P_{Cm}(h)$ from h. it is shown that P_{Cm} is approximated by:

5.11

$$P_{Cm}h(t) = \begin{cases} P + \left(h(t) + k\dfrac{M' - \dfrac{M_1}{M_0}}{\alpha D} \right), & if\ t \in [0, D] \\ 0, & elsewhere \end{cases}$$

where k is a positive real number.

Given P_{Cm}, the computation procedure is again completely as the one of Bertero et al. (1997): we start from $F_\theta{}^0 = 0$, compute equation (4.8) in the frequency domain, and come back to the time domain to use P_{Cm} as defined by equations (4.9) and (4.11). We then obtain $F_\theta{}^1$ and repeat the operation, transforming into the frequency domain to compute again equation (4.8) and so on. The scheme (4.9) is semiconvergent, that is, it approaches the solution before diverging again. However, the minimum seems very flat, and good results are obtained after a few hundred iterations.

5.4 Metodology

The approach used to invert the aSTFs generalizes the technique proposed by Emolo and Zollo (2005) to invert strong-motion data. The model parameters are the values of slip and rupture velocity specified, as in the original formulation, at a set of control-points on the fault plane. The distributions over the whole fault at a finer scale are then obtained by a bicubic interpolation; this is required, for example, for the correct computation of the representation integral to solve the forward problem

thus avoiding undesired spatial aliasing effects. The best slip and rupture velocity values at the fault control-points are determined by using the Genetic Algorithm (Goldberg 1989; Charbonneau 1995) to search for the maximum of a fitness function, based of the comparison between real and synthetic STFs. A multi-scale approach is adopted, according to which the number of control-points is progressively increased in successive inversion runs so to move from a high- to low-wavelength description of kinematic parameters on the fault. The optimal model parameters set is finally chosen according to the Akaike Information Criterion (Akaike, 1974) for model selection and modified from its original formulation by Cavanaugh (1997). Following this Akaike's criterion, the best parameterization is the one that minimizes the function:

5.12

$$AICc = N \ln(2\pi E) + \frac{N(N+P)}{N-P-2}$$

In equation 5.12, N is the number of data, P is the number of the model parameters, i.e., the number of slip and rupture velocity values used to define the model and, finally, E represents the misfit value (obtained like the L_2-norm between real and synthetic data). The model that satisfies this criterion represents the best compromise between fit quality and simplicity of the model.

5.4.1 The Forward Problem

Following the Emolo & Zollo (2005) formulation, the ground displacement associated with the seismic phase propagating, with velocity *c*, at a given receiver located at **x**, can be obtained as the sum of signals emitted by elementary sources (subfaults) densely distributed on the rupturing surface:

5.13

$$u^c(\boldsymbol{x},t) = \sum_{m,n} u^c_{m,n}(\boldsymbol{x},t)$$

where the ground displacement produced by the subfault (m,n), $u^c_{m,n}(\boldsymbol{x},t)$, is given by the representation integral (Aki & Richards, 2002):

5.14

$$u^c_{m,n}(\boldsymbol{x},t) = \iint_{subfault} G^{FF}_{m,n}(\boldsymbol{x},\boldsymbol{\xi};t,0) * \mu\Delta\dot{u}_{m,n}(\boldsymbol{\xi};t-T^c_{m,n})d\Sigma$$

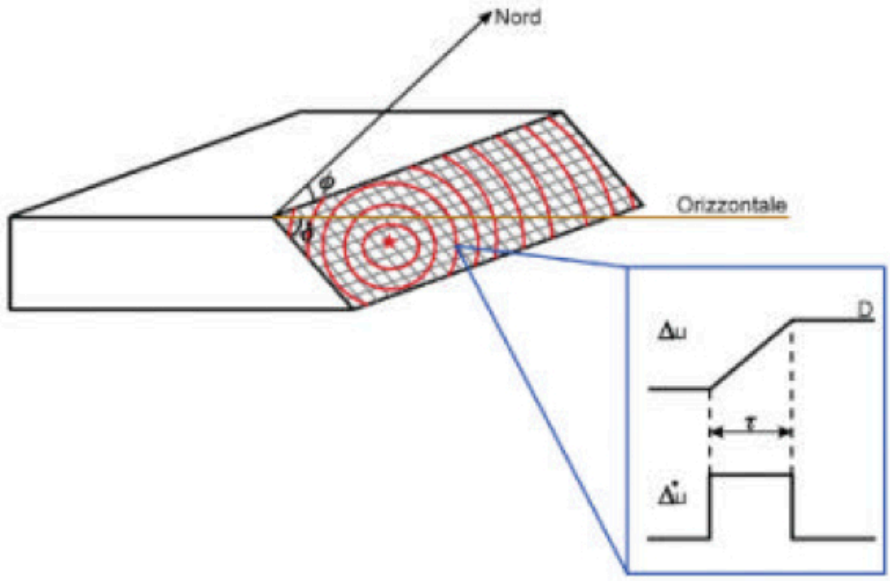

Figure 5.1: The rupture front (red lines) starts from a point (asterisk) and then propagates on the fault with a general heterogeneous velocity. When a fault point is invested from the rupture front, starts to move i.e. changes from a null value to a final dislocation value D at time t. In figure are also shown the strike (ϕ) and dip (φ) angle that allow the identification of the fault plane orientation.

In (5.14), $G^{FF}_{m,n}$ is the Green's function in the far-field approximation μ is the

medium rigidity, $\Delta\dot{u}_{m,n}$ is the time-derivative of local Source Time Function and $T^c_{m,n}$ represents the time needed by the wave c to travel from the elementary source (located on the fault plane at the position $\boldsymbol{\xi}$) to the receiver.

In the case of a single Green's function, that can be considered representative of a median fault-point $\bar{\boldsymbol{\xi}}$, as, for instance, on Empirical Green's Function, we have

5.15

$$G^{FF}_{m,n}(\boldsymbol{x},\boldsymbol{\xi};t,0) \simeq G_{EGF}(\boldsymbol{x},\bar{\boldsymbol{\xi}};t,0)$$

Replacing the equation 5.14 in equation 5.13, and using the condition 5.15, we find:

5.16

$$u^c(\boldsymbol{x},t) = G_{EGF}\left(\boldsymbol{x},\bar{\boldsymbol{\xi}};t,0\right) * \sum\nolimits_{m,n} \iint\limits_{subfault} \mu\Delta\dot{u}_{m,n}(\boldsymbol{\xi};t-T^c_{m,n})d\Sigma$$

Since the apparent Source Time Function can be computed deconvolving the EGF from the observed seismogram

5.17

$$aSTF(\boldsymbol{x},t) = (u^c * G_{EGF})^{-1}$$

The final formulation of our forward modeling can be written as

5.18

$$aSTF(\boldsymbol{x},t) = (u^c * G_{EGF})^{-1} = \mu \sum_{m,n} \iint\limits_{subfault} \Delta\dot{u} \;\; (\boldsymbol{\xi};t-T^c_{m,n})d\Sigma$$

The Empirical Green's Function (G_{EGF}) must satisfy three conditions:

1. Its magnitude is at least one unit smaller than the mainshock one;

2. The fault mechanism for the mainshock and EGF events are similar and EGF is located on the mainshock fault plane, so that it can approximate the path propagation effects, including anelastic attenuation and site effects.
3. Distances of receivers from the fault are much larger than the linear extension of the fault, so that a single EGF record can be used to reproduce the propagation effects from any fault point;

The local Source Time Function in equation 5.14 is approximated by a box-car function. Its onset time clearly depends on the time at which the rupture front reaches the sub-fault (m,n), to resolve the equation 5.18 we have also to estimate the rupture time on the fault. For a heterogeneous rupture-velocity distribution this problem is solved using the 2D finite-difference code of Podvin & Lecomte (1991), which computes the rupture times at any point of a discretized fault plane, given a source nucleation position and a distribution of the rupture velocity.

5.4.2 The Podvine & Lecomte Algorithm

The calculation of synthetic seismograms makes use, among other parameters, of the time distribution on the fault rupture. The subject of inversion will be, rather than the times, the rupture velocity. Therefore it is necessary to have a method able to allow calculation of times from the rupture velocity. For its reliability and calculation speed, we chose for this purpose the algorithm of Podvin & Lecomte (1991). This algorithm, starting from the distribution of slowness (s), parameterized on a regular grid in a propagation medium, and noting the position of the origin of the times (the position of an artificial source of seismic waves or, as in our case, the position on the fault hypocentre the earthquake), calculates the time path of the wave faster in the nodes of the grid solving the first order equation eikonal

5.19

$$\left(\frac{\partial T}{\partial \xi}\right)^2 + \left(\frac{\partial T}{\partial \varsigma}\right)^2 = s^2$$

where T is the travel time of the seismic wave with slowness s.

Rather than using representation through a regular grid of slowness as a mathematical tool to solve, with finite differences, equation 5.19, Podvin & Lecomte (1991) approximates the slowness model using a model with square cells of side h with a constant slowness value. Applying, systematically, Huygens's principle to this model, we have the following five estimators for the travel time from the M point to P point (see Podvine & Lecomte 1991).

5.20

$$\text{if } \left(0 \leq t_N - t_M \leq \frac{h_S}{\sqrt{2}}\right), \text{ then } t_P = t_N \pm \sqrt{{h_S}^2 - (t_N - t_M)^2}$$

for direct waves that travel $M \rightarrow N \rightarrow P$

5.21

$$\text{if } \left(0 \leq t_O - t_M \leq \frac{h_S}{\sqrt{2}}\right), \text{ then } t_P = t_O \pm \sqrt{{h_S}^2 - (t_O - t_M)^2}$$

for direct waves that travel $M \rightarrow O \rightarrow P$

5.22

$$t_P = t_M + \sqrt{2} h_S$$

for direct waves that go from M to P,

5.23

$$t_P = t_N + h \min(s, s')$$

for direct waves that travel $M \rightarrow N \rightarrow P$ as *head wave*, and

5.24

$$t_P = t_O + h \min(s, s'')$$

for waves that travel $M \rightarrow O \rightarrow P$ as *head wave*. The travel time from M to P is assigned the smallest value among those supplied by the five estimators 5.20 - 5.24.

5.4.3 The Inverse Problem

The final slip and rupture velocity values at the control-points along the fault are determined by searching for the maximum of a fitness function F, defined hereinafter. For this aim we used the Genetic Algorithm (GA), which provides a very efficient and fast method for the global exploration of a misfit function in a multidimensional model space (Goldberg 1989; Sambridge & Drijkoningen 1992; Charbonneau 1995; Boschetti *et al.* 1996). After each run of the inversion procedure the number of control-points is progressively increased. At each step, the parameter search is performed in the neighborhood of the model determined in the previous step, with a smaller number of grid nodes. The range of allowed slip- and rupture-velocity values (which we used to define the initial population for the GA) around the model estimated in the previous run are then progressively decreased as we move ahead with the inversion. This approach is similar to the "multi-scale" strategy that is commonly used in seismic tomography and in migration techniques (Lutter *et al.* 1990; Jin & Beydoun 2000), to explore efficiently complex, multi-dimensional, model parameter spaces.

If we consider a set of N_s seismic station for which the aSTFs are available, the fitness function to be maximized is given by

5.25

$$F = \frac{E_{max} - E}{E_{max}}$$

where

5.26

$$E = \frac{\sum_{i=1}^{N_s} \sum_{j=1}^{N_T(i)} [(S_{ij}^{obs}) - (S_{ij}^{theo})]^2}{\sum_{i=1}^{N_s} \sum_{j=1}^{N_T(i)} [(S_{ij}^{obs})]^2}$$

E_{max} is the maximum allowed value for the cost function that is assumed, in our applications, as the misfit value obtained for a homogeneous slip model. In the relationship (5.26), S^{obs} represents the observed aSTF and S^{theo} is the aSTF computed for a given set of model parameters. Moreover, $N_{t.}$ is the number of samples of the aSTFs at the receiver i-th.

5.5 Application

On April 6, 2009, at 01:32 UT, a moderate earthquake, M_w6.3, struck central Italy, in Abruzzo region causing more than 300 casualties and an extended damage. The mainshock was preceded by a sequence started a few months before and culminating with a M_L4.1 event on March 30, followed by a M_L 3.9 and M_L 3.5 foreshocks on April 5. The April 6 main event was followed by an intense aftershock activity that lasted several months (Cirella *et al.* 2009; Maercklin *et al.* 2011). The largest events in the sequence were the M_w 5.6 April, 7 and Mw 5.4, April 9 aftershocks which occurr a few kilometers south and north of the main shock (Chiarabba *et al.* 2009).

We applied the inversion procedure described above to determine the rupture parameters of a M_w 4 aftershock occurred on 2009, April 09, at 04:43 UTC. The records from a M_w3 event occurred on 2009, April 13, at 21:19 UTC have been used as EGFs (figure 4.3 and table 5.1). Both accelerometric and velocimetric data recorded by DPC-RAN (National Accelerometric Network managed by the

Department of Civil Protection) and INGV National Institute of Geophysics and Volcanology) networks (figure 5.2 and table 5.2) have been considered for the analysis of the Mw 4 event**.** The apparent source time functions have been computed by applying the stabilized deconvolution technique proposed by Vallée (2004), which integrates in the deconvolution process four physical constraints on the aSTFs, e.g. the causality, positivity, limited duration, and equal area.

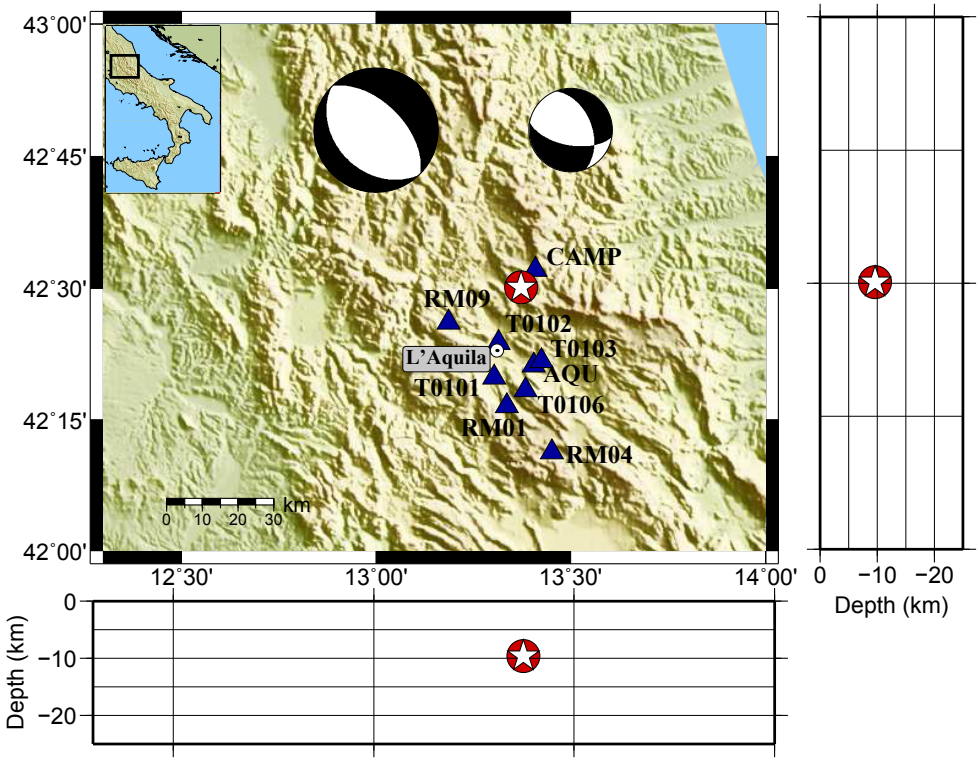

Figura 5.2: Source-receivers geometry. The blue triangles represent the DPC-RAN and INGV seismic stations used in this study. The white star and the red dot represent the location for the master and the EGF events, respectively. The computed focal mechanisms are also shown in the figure.

To satisfy the validity condition for the EGF approach (ref. equation 5.15), a

preliminary study of the complete aftershocks catalogue for the Aquila seismic sequence was carried out based on the difference in magnitude and location for a large number of pairs master event-EGF. The master event was located using the probabilistic location method (NLLOC, Lomax *et al.* 2000) at latitude of 42.50°N, longitude of 13.37°E and depth of 11.27 km. Finally, the focal mechanisms were computed through the FPFIT code (Reasemberg *et al.* 1985) from the P-wave polarities finding for the master event strike=135°, dip=35°,rake=-90°.

The deconvolution was performed for the direct S-wave in the frequency range of 0.2-10 Hz. The S-wave windows were selected by identifying the stable polarization windows (Emolo & Zollo 2005).

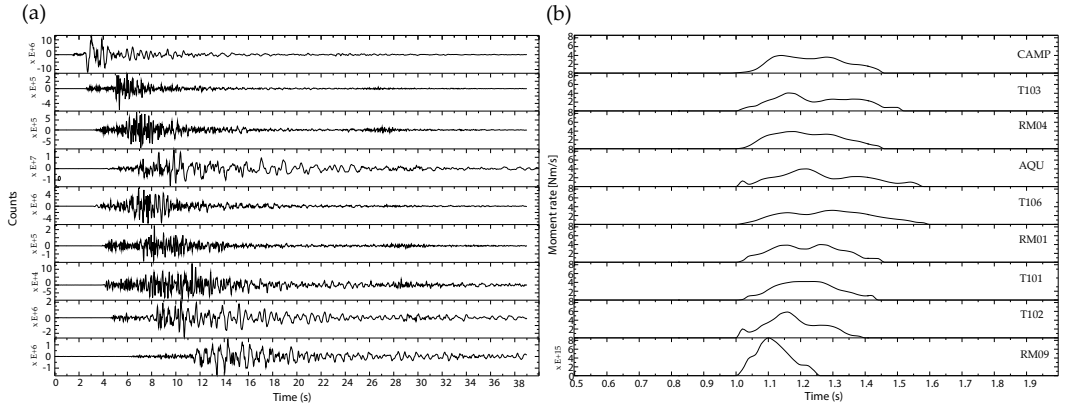

Figura 5.3: a) Waveforms for the M_w4.0, April 09, 2009 earthquake (master event) analyzed in this study. The waveforms are organized as a function of the epicentral distance. b) aSTFs estimated through the deconvolution of the selected EGF from the master event.

We assume that in this frequency band and in the near-source distance conditions (R<50 km), the direct S-wave is the most energetic phase. The minimum frequency (f_{min}) was chosen according to the limit imposed by the expected corner frequency (f_c) of the master event, i.e $f_{min} << f_c$. The maximum frequency has been estimated by analyzing the stability of the direct S-wave polarization with time along the seismogram, which provides a good indication of the optimal frequency range to be

used for the source parameter waveform inversion (Emolo & Zollo 2005).

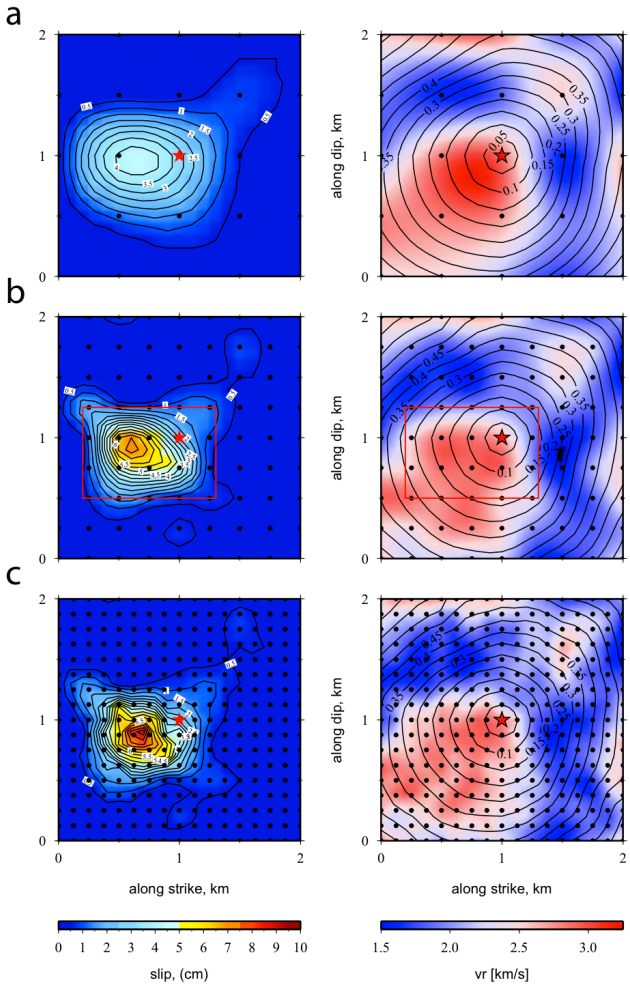

Figura 5.4: Slip (left side) and velocity rupture models (right side) for the M_w4.0, April 09, 2009 earthquake. The results of the inversion corresponding to a different control-points number are shown. The black dots represent the control-points. (a) 5 x 5 grid. (b) 9 x 9 grid. (c) 17 x 17 grid. The red star in each panel indicates the rupture nucleation point on the fault plane, corresponding to the earthquake hypocentre. In the panel b the red box represents the second fault plane adopted (see text for details)

The waveforms of the master event and the corresponding aSTFs, achieved by EGF deconvolution, are shown in the panels a and b of figure 5.3, respectively. We note

the strong directivity effect associated with the source, highlighted by the differences in signal durations and amplitudes at stations CAMP and RM09. The relative position of these station and difference in waveforms indicate a preferred rupture direction to the Southwest for this event.

5.5.1 Kinematics Inversion for the Mw 4.0, April 09, 2009 event

The inversion of real-data is performed assuming an initial 2x2 km^2 fault plane centered at the earthquake hypocentre and running, according to the multi-scale procedure, three inversions using 5x5, 9x9 and 17x17 control-points, respectively. As explained before, the optimal slip and rupture velocity maps were finally chosen using the statistical criterion of Akaike.

Figure 4.4 displays the results obtained at the end of each step of the multi-scale approach. According to the Akaike criterion, we select the 9x9 control-points maps as the best-fit result. For this model we found a misfit of 0.41 and a corresponding fitness of 0.91. Looking at the results corresponding to control-points distribution, we explicitly note the increasing degree of complexity of the resulting images that can be associated with the contribution of small wavelength components, as the number of control-points increases.

The best-fit slip distribution (panel b in figure 5.4) is characterized by an average slip of about 0.8 cm corresponding to a seismic moment of $0.9x10^{15}$ Nm. This estimation is consistent with the value obtained from the inversion of S-wave displacement spectra (Mo= $1x10^{15}$ Nm), by using a parametric modeling approach (Orefice & Zollo 2010).

The rupture velocity distribution presents an isotropic distribution on the fault plane with area characterized by a higher velocity in the southwestern sector of the fault. This acceleration of the rupture front explains the clear directivity effects visible on the aSTFs recorded at RM09 and CAMP stations. In fact, they show large

amplitude with small duration and small amplitude associated with large signal duration, respectively.

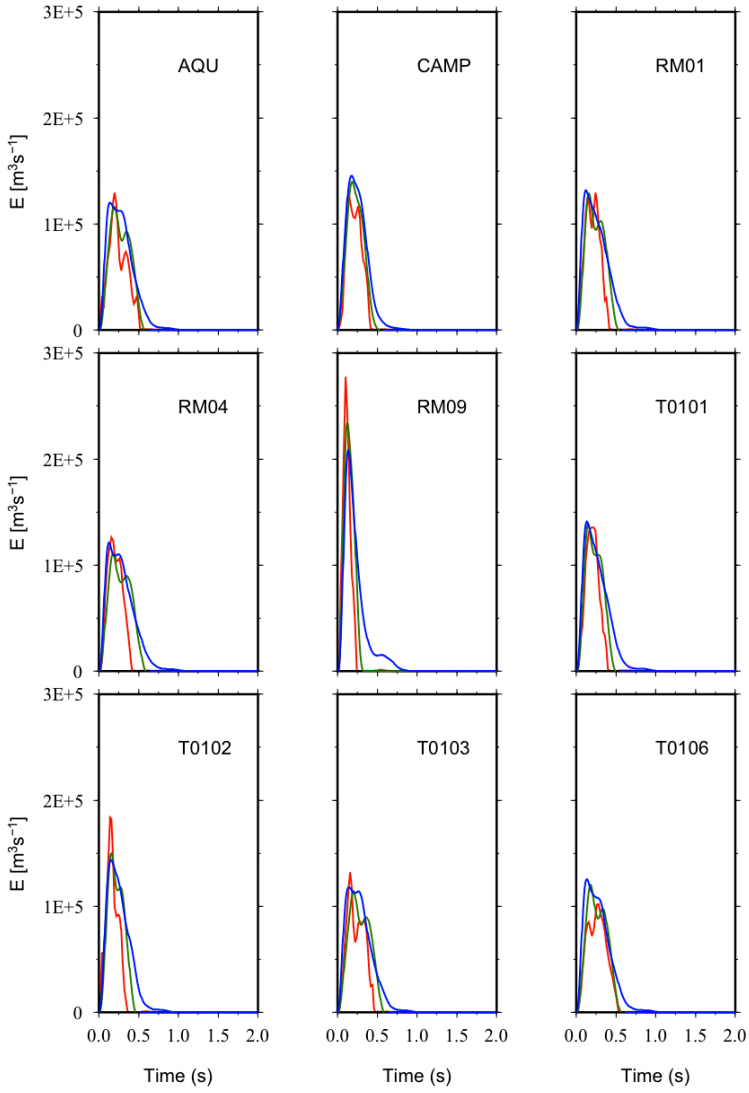

Figura 5.5: Comparison between real (red line) and synthetic (blue and green lines) aSTFs at the different stations. The blue line represents the synthetic aSTFs computed for the whole fault model shown in figure 3 (panel b), while the green line is relative to the fault portion limited by the red box in figure 3 (panel b).

The comparison between real and synthetic aSTFs (Figure 5.5) show that, despite a

general good agreement between the two sets of data, there are some short-period features (especially for the station AQU) that aren't reproduced.
Moreover, a general disagreement between the duration of real and synthetic aSTFs is observed. In fact, the duration of the synthetic aSTFs is generally larger than the duration of the real signals.

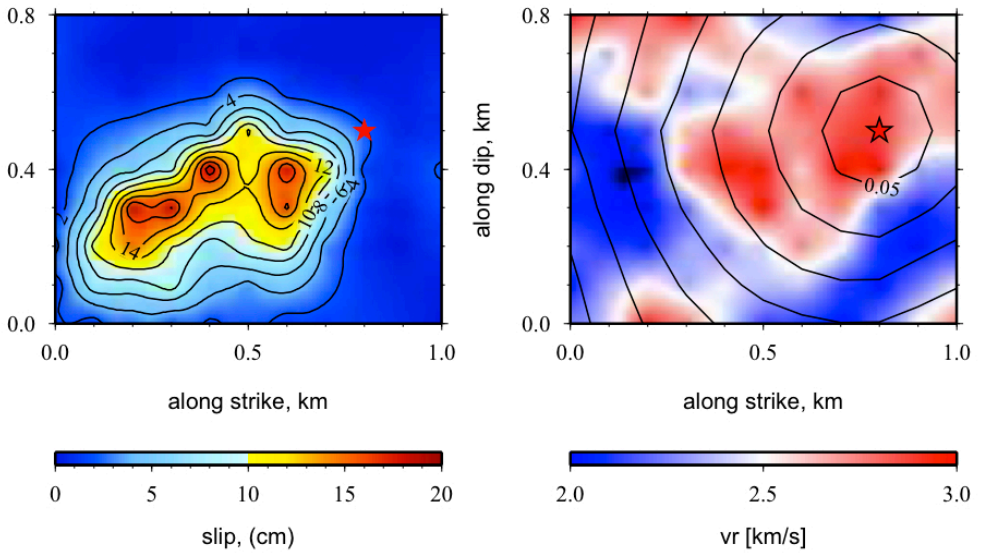

Figura 5.6: Slip (left panel) and velocity rupture models (right panel) for the M_w4.0, April 09, 2009 earthquake. The results of the inversion corresponding to a 11x9 control-points distribution. The red star in each panel indicates the rupture nucleation point on the fault plane, corresponding to the earthquake hypocentre.

To eliminate the inconsistency between theoretical and real aSTFs duration, we observe that a large part of the fault plane is characterized by very low slip values, so we decided to select a smaller fault plane. The new fault plane was identified as the surface included by the 1-cm slip isoline (panel b of figure 5.4) that corresponds to the minimum slip value producing appreciable amplitude in the data with respect to the noise-level.

The new fault dimensions are 1 km along the strike and 0.8 km along the dip direction. These dimensions are also consistent with the source radius estimation (about 500 m) obtained from the corner frequency estimated from the displacement spectra analysis. In this new configuration, the hypocentre is located near the SE side (0.8 km along strike and 0.5 km along dip) of the fault plane (panel b in figure 5.4) testifying a quasi-unilateral rupture propagation to NW for this event.

Event	Date dd/mm/yy hh/mm/ss	M_w	Focal Mechanism strike/dip/rake (Degree)	Localization Lat/Lon (Degree)	Depth (Km)
Master	09/04/2009 04:43:09	4.0	135/35/-90	42.509/13.379	9.3
EGF	13/04/2009 21:19:52	3.0	130/40/-80	42.502/13.373	9.6

Table 5-1: Main characteristic of analyzed event. Localization and focal mechanism are estimated through NLLOC (Lomax *et al*., 2000) and FPFIT (Reasemberg *et al*., 1985), respectively.

We then performed a new inversion for this smaller fault plane considering both constant and variable rupture velocity models and using 11x9 control-points distribution. The selected control-point configuration allows us to reconstruct the aSTFs up to the maximum frequency that we want to model (10 Hz). The results of this inversion are reported in figures 4.5 and 4.6. Concerning the constant velocity rupture model, different inversions were performed for different velocity values in the range 2.0-3.0 km/s, obtaining the minimum misfit for <vr>=2.8 km/s.

The results for the model with variable rupture velocity are shown in the figure 5.6 panel a and b. This model is preferred from the statistical point of view according to Akaike criterion, since it provide a lower value of the Akaike parameter (equation 5.12) than constant velocity rupture model. Two main dislocation patches, with an areal dimension of about 400 and 600 m^2, characterize the slip distribution, which

has an average value of 3.6 cm, corresponding to a seismic moment of 0.9 x 10^{15} Nm, when the 1 x 0.8 km2 fault plane is considered. The rupture initially enucleated in an area of low slip, but with relatively high rupture velocity. The rupture velocity distribution is characterized by an initial acceleration followed by a deceleration of the rupture front. The deceleration occurs in correspondence of the separation zone between the two-slip patches. The rupture velocity model presents an average velocity rupture of 2.5 km/s, which is consistent with the value retrieved by Cirella *et al*. 2009 for the L'Aquila mainshock.

Station name	Latitude (degree)	Longitude (Degree)	Elevation (m)
AQU	42.3540001	13.4049997	710
CAMP	42.5357819	13.4090004	1283
OFFI	42.9350014	13.6857004	320
RM01	42.2767067	13.3355703	*Unknown*
RM04	42.1884613	13.4514599	*Unknown*
RM09	42.4355011	13.1864901	*Unknown*
T0101	42.3307648	13.3026333	850
T0102	42.3967171	13.3139172	707
T0103	42.3618507	13.4244833	849
T0106	42.3069000	13.3837004	1205

Table 5.2: Characteristics of used stations.

Looking at the comparison between real and synthetic aSTFs (figure 5.5) we note the good accordance between the signal durations. Moreover, we are able to reconstruct the complex features of the real data as in the case of the stations AQU, T0102 and T0103. Finally, the new fault plane configuration allows us to also recover additional energy at the RM09 station.

To compute the relative error associated with the final slip and velocity rupture

maps we used the method proposed by Emolo & Zollo (2005). The uncertainties associated with the source kinematic parameters (slip and velocity rupture) are estimated through a perturbation analysis performed at any single control-point around the final best model p_{best}, selecting one parameter at a time and fixing all the remaining one at the best fit values. The misfit is then evaluated for each perturbed parameter so it is possible to construct the probability density function (pdf):

5.27

$$\mathrm{pdf}(p) = Ce^{\left[-\frac{E^2(p)}{2\sigma_0^2}\right]}$$

where C is a normalization constant (see equations 8 in Emolo & Zollo 2005).
The equation 5.27 represents the marginal probability distribution function for each parameter around its best value in the considered range [-10% p_{best}; +10% p_{best}], and it allows estimating the uncertainties on the rupture model parameters. The parameter σ_0^2 in the previous equations is the unknown variance of the misfit function, and it accounts for errors both in the modeling and data. The value of the σ_0^2 parameter is assumed according with the best fit model variance.
The relative uncertainties on slip and rupture velocity are shown in figure 5.7. This result shows that the relative errors, both for slip and for rupture velocity, are around 30 %. The two maximum slip patch shows in figure 5.6 (panel a) correspond with the minimum errors in figure 5.7 (panel a). Moreover the relative errors for the velocity rupture highlight how the rupture front deceleration (figure 5.6, panel b) corresponds with the minimum errors (figure 5.7, panel b).

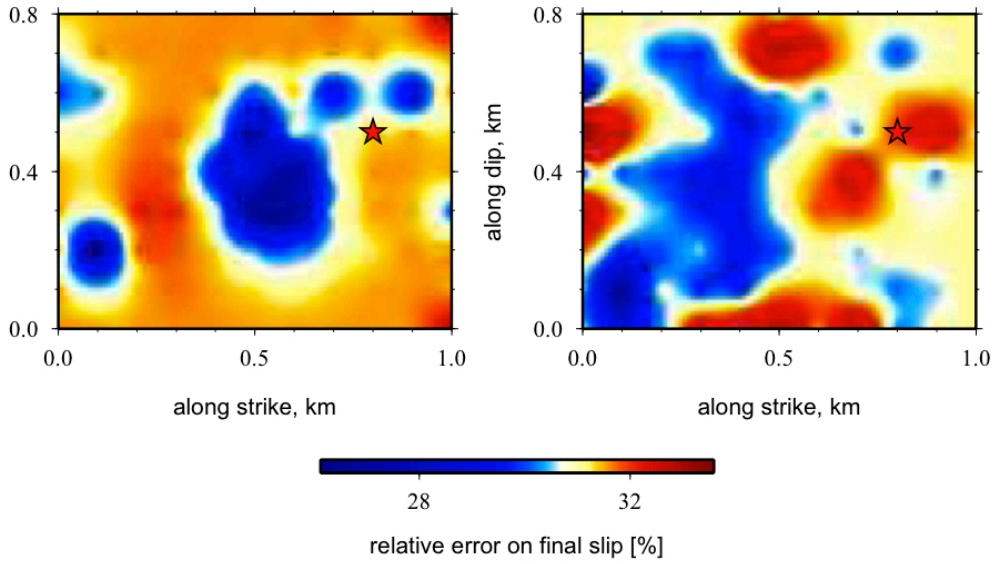

Figura 5.7: Relative error distributions for the final slip (left) and rupture velocity (right) associated with the models shown in the figure 5. In figures the red star indicates the rupture nucleation point.

5.5.2 Resolution test

Different synthetic analyses have been performed to test and validate the inversion procedure and the obtained results, using different source-receivers geometry and rupture models. The general strategy adopted for these tests consisted in

- assigning realistic slip and velocity distributions on a given fault plane;
- computing the synthetic aSTFs at different stations, and adding some random noise;
- performing the inversion procedure and comparing the retrieved models with the initial ones.

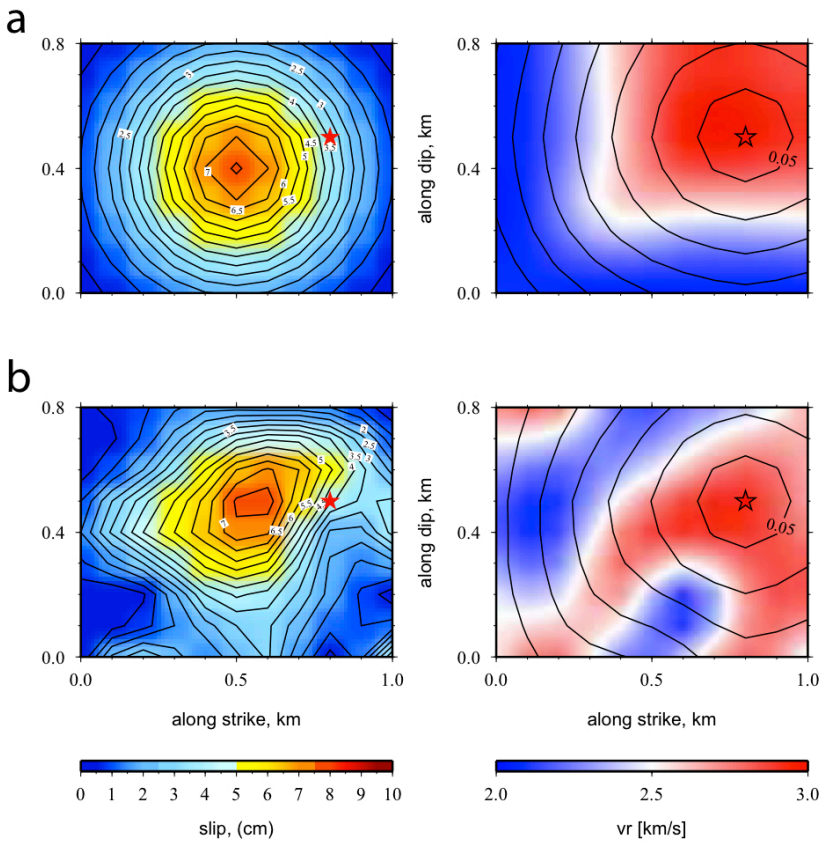

Figura 5.8: **Synthetic test. Comparison between the "true" rupture model (panel a) and that inferred from the inversion (panel b). The left and right sides of each panel represent the slip and velocity rupture distribution, respectively. The red star indicates the position of the rupture nucleation point on the fault plane.**

Among the several test performed, we present here the results for the modeling of a M_w4.0 events, associated with a 1 x 0.8 km^2 fault plane (strike=135^o, dip=35^o), prescribing a distribution for the slip having a Gaussian shape with a maximum value of 7.5 cm and an average value of 2.6 cm. The rupture velocity distribution is characterized by an initial acceleration in correspondence of the hypocentre location, followed by a deceleration toward the left side of the fault and has an average value of about 2.5 km/s. The starting rupture model is reported in the panel a of figure 5.8. For this synthetic test we considered the same source-stations

geometry shown in figure 1 and so this study represents a resolution test for the application of the inversion technique to real data, presented above. We performed the inversion of synthetic records in the frequency range 0.2-10 Hz.

We perform an inversion considering both the cases of constant and variable rupture velocity. The results of this study are reported in figures 5.8 (panel b) and 5.9. As for the real case, also for this synthetic test the Akaike criterion indicates the variable rupture velocity model is preferred.

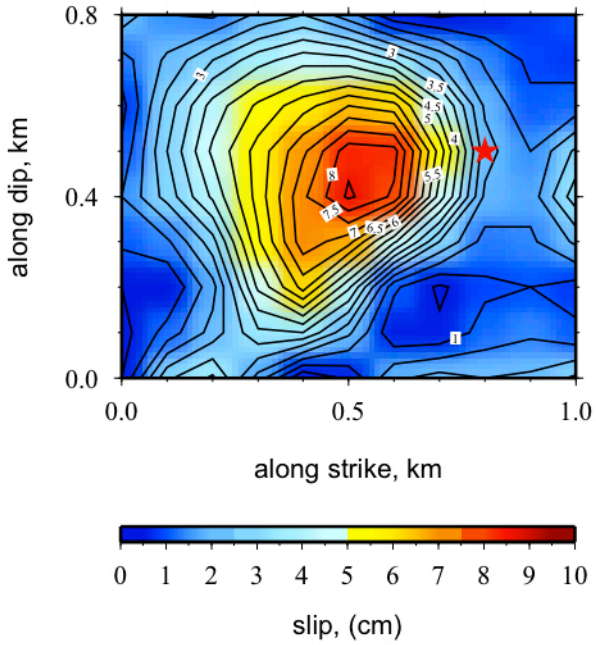

Figura 5.9: Synthetic test. Slip model from the inversion of the synthetic aSTFs, corresponding to the model shown in figure 5.8 (panel a), considering a constant velocity rupture model. The red star indicates the position of the rupture nucleation point on the fault plane.

The retrieved final slip and rupture velocity models show similar shape and features of the initial model, but with a more scattered pattern and are characterized by an average slip and rupture velocity of 2.6 cm and 2.5 Km/s, respectively. Finally,

Figure 5.10 shows the difference between the initial and retrieved slip and rupture velocity maps. Both the constant and variable velocity rupture models show that in both cases the area with the greatest error is localized near bottom of the fault (figure 5.10 panel a and c). Furthermore the constant velocity rupture model overestimated the maximum slip.

Overall, the results from the synthetic tests suggest that, despite the small fault dimension and the uneven azimuthal station coverage, we expect a good parameter resolution on the fault plane, and in particular, we are able to discriminate between uniform and variable slip/rupture velocity distributions.

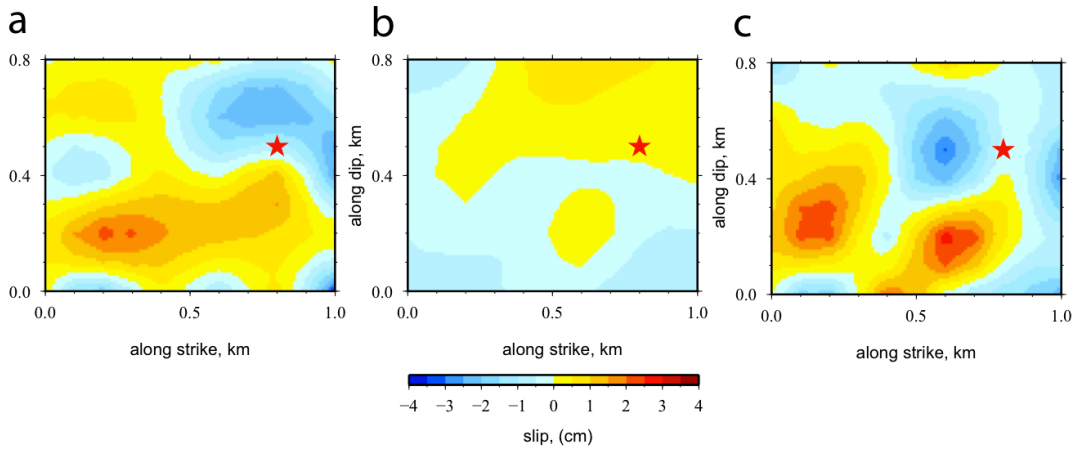

Figura 5.10: Residual distributions. The panels a and b show the difference between the synthetic (figure 5.8, panel a) and inferred (figure 5.8, panel b) slip and velocity rupture models, respectively. The panel c instead is the difference between the synthetic (figure 5.8, panel a) and inferred slip model (figure 5.9).

5.6 Conclusions

In this study we have developed a method for the inversion of the apparent Source-Time Functions aimed at inferring the kinematic rupture model (i.e., slip and rupture velocity distributions) for a seismic event. In our method, the model parameter space is explored by searching for the maximum of a fitness function,

obtained from a misfit function defined as the L_2-norm of difference between real and synthetic data, through the using of the Genetic Algorithm (Golberg 1989; Charbonneau 1995).

The main advantages of inverting aSTFs are related to the possibility to avoid the explicit calculation of the Green functions needed for solving the forward problem related to the simulation of the synthetic data. Reliable Green functions computation is crucial for any seismogram inversion/simulation technique and they strongly depend on the accuracy of the velocity structure, in addition to the numerical approximations associated with adopted method. Moreover, site amplification effects are naturally accounted and removed by the EGF deconvolution. These phenomena, depending on the local geological characteristics at the receivers, may strongly influence the seismic signals and then bias the data inversion. Finally, the use of aSTFs can allow performing the data inversion in a much wider frequency range compared with usually adopted inversion approaches.

The main disadvantage of this method is, however, at the same time associated with the calculation of reliable aSTFs for a given seismic event that is, for instance related to the availability of seismograms to be used as Empirical Green Function for the seismic event of interest.

In this paper we presented the application of the proposed inversion method to both a synthetic and a real data-sets. In particular, we studied a Mw 4 aftershock of the 2009 L'Aquila (central Italy) seismic sequence, for which, due to the availability of different EGFs, it was possible to determine the aSTFs at the different stations. For this event the inversion results show a rupture model associated with a fault plane of 1x0.8 km^2 and characterized by a total seismic moment of about 0.9 10^{15} Nm, corresponding to a moment magnitude of 3.9.

Our study shows the feasibility to image the complexity of an earthquake rupture process at a kilometric size, rupture scale. The slip model consists of two main patches (maximum amplitude of about 17 cm) localized NW of the hypocentre. The

Akaike test suggests, both for the real and synthetic analysis, that a variable rupture velocity model has to be preferred with respect to a constant rupture velocity propagation. We found an average rupture velocity of about 2.5 km/s, with an initial acceleration of the rupture front toward the SW direction, followed by a deceleration of the same near the left side of the fault plane. The rupture has nucleated in a low slip-high rupture velocity area propagated almost unilaterally toward the southwest direction. The parameter uncertainty analysis shows that the zones on the fault plane characterized by large slip and rupture velocity are well resolved as being characterized by low errors (around 25%).

The encouraging results obtained by this new approach lead us future applications of the method to larger magnitude events, provided that the conditions related to the calculation of reliable aSTFs are verified.

6 In Summary …

The purpose of this PhD thesis was to investigate the source kinematic characteristics of an earthquake through the inversion of data that recorded the event. To this end, different data-sets obtained through varies acquisition methods, as seismic stations (dynamic wave filed) and satellite techniques (static deformation field) are today available. In particular the joint use of all these data, rather than just one type could provide details on the estimation of source characteristic at different wavelength scale.

During my PhD, starting from the original formulations proposed by Bertrand *et al*., 2000 and Emolo & Zollo 2005, I developed inversion methods and applied then at different earthquakes. In particular large efforts have been devoted to the study of the model resolution and to the estimation of the model parameter errors.

To study the source kinematic characteristics of the Christchurch earthquake we performed a joint inversion of strong-motion, GPS and InSAR data using a non-linear inversion method. Considering the complexity highlighted by superficial deformation data, we adopted a fault model consisting of two partially overlapping segments, with dimensions 15x11 and 7x7 km^2, having different faulting styles. This two-fault model allows to better reconstruct the complex shape of the superficial deformation data. The total seismic moment resulting from the joint inversion is $3.0x10^{25}$ dyne.cm (Mw = 6.2) with an average rupture velocity of 2.0 km/s. The main slip patch (maximum slip of about 4.2 m) occurred 3km NE of the hypocenter, on the first fault plane that was characterized with by a dominant strike-slip movement. The second fault plane, characterized by a dominant reverse faulting, activated about 3-4 sec later than the rupture on the first fault plane, and

the maximum slip on it was about 2 m. The first and second plane accounted for 80% and 20% of the total seismic moment, respectively. The global Source Time Function shows a total duration of about 7 s. The slip distribution is mainly concentrated between 2 and 5.5 km in depth. The lack of slip near the surface is perfectly consistent with both the absence of observed surface rupture, and with the shape highlighted by the InSAR coseismic deformation data. Errors associated with the kinematic model have been estimated of around 20-30 %.

The 2009 Aquila sequence was characterized by an intense aftershocks sequence that lasted several months. In this study we applied an inversion method that assumes as data the apparent Source Time Functions (aSTFs), to a Mw 4.0 aftershock of the Aquila sequence . The estimation of aSTFs was obtained using the deconvolution method proposed by Vallée *et al*., 2004. The inversion results show a heterogeneous slip distribution, characterized by two main slip patches located NW of the hypocenter, and a variable rupture velocity distribution (mean value of 2.5 km/s), showing a rupture front acceleration in between the two high slip zones. Errors of about 20% characterize the final estimated parameters.

7 References

Aarts, E. & Korst, J., 1989. *Simulated Annealing and Boltzmann Machines: a stochastic approach to combinatorial optimization and neural computing*. *Wiley.*

Abercrombie, R. E., Webb, T. H., Robinson, R., McGinty, P. J., Mori, J. J. & Beavan, R. J., 2000. The enigma of the Arthur's Pass, New Zealand, earthquake: 1. Reconciling a variety of data for an unusual earthquake sequence, *J. Geophys. Res*., 105, 16,119–16,138.

Akaike, H. 1974. A new look at the statistical model identification, *IEEE Trans. Autom. Control* 6, 716–723.

Aki, K. & Richards, P. G., 1980. *Quantitative Seismology, Theory and Methods* (2 volumes), pp.923, W. H. Freeman, San Francisco.

Aki, K., & Richards, P. G., 2002. *Quantitative seismology,* 2nd edn, Vol., pp. ,University Science Books Sausalito, California.

Ameri, G., Gallovič, F., Pacor, F. & Emolo, A., 2009. Uncertainties in strong ground-motion prediction with finite-fault synthetic seismograms: an application to the 1984 M 5.7 Gubbio,Central Italy, earthquake, *Bull. Seism. Soc. Am.*, 99, 647–663.

Ammon, C. J., A. A. Velasco, and T. Lay (1993), Rapid estimation of rupture directivity: application to the 1992 Landers (M_S=7.4) and Cape Mendocino (M_S=7.2), California earthquakes, *Geophys. Res.Lett.* 20**,** 97–100.

Arnadottir, T., Beavan, J. & Pearson, C., 1995. Deformation associated with the 18 June 1994 Arthur's Pass earthquake, New Zealand, *N. Z. J. Geol. Geophys*., 38, 553–558.

Atzori, S., Tolomei, C., Antonioli, A., Merryman Boncori, J. P., Bannister, S., Trasatti, E., Pasquali, P. & Salvi, S., 2012. The 2012-2011 canterbury, new Zealand, seismic sequence: Multiple source analysis from InSAR data and modeling, *Journal Geophys. Res.*, Vol. 117, B08305.

Bannister, S., Fry, B., Reyners, M., Ristau, J. & Zhang, H., 2011. Fine-scale relocation of aftershocks of the 22 february mw 6.2 christchurch earthquake using double-difference tomography, *Seism. Res. Lett.*, *82*, 839–845.

Barnhart, W. D., Willis, M. J., Lohman, R. B. & Melkonian, A. K., 2011. InSAR and Optical Constraints on Fault Slip during the 2010-2011 new Zealand earthquake sequence, *Seism. Res. Lett.*, *82*, 815–823.

Beavan, J., Tregoning, P., Bevis, M., Kato, T. & Meertens, C., 2002. Motion and rigidity of the Pacific plate and implications for plate boundary deformation. *J. Geophys. Res.,* 107, 2261-2276.

Beavan, J., Samsonov, S., Motagh, M., Wallace, L., Ellis, S. & Palmer, N., 2010. The Mw 7.1 Darfield (Canterbury) Earthquake: Geodetic observations and preliminary source model, *Bull. New Zeal. Soc. Earthquake Eng.*, *43*, 228–235.

Beavan, J., Fielding, E., Motagh, M., Samsonov, S. & Donnelly, N., 2011. Fault

location and slip distribution of the 22 february 2011 mw 6.2 christchurch, new zealand, earthquake from geodetic data, *Seism. Res. Lett.*, *82*, 789–799.

Beavan, J., Motagh, M., Fielding, E. J., Donelly, N., Collett, D. (2012): Fault slip models of the 2010- 2011 Canterbury, New Zealand, earthquakes from geodetic data and observations of postseismic ground deformation. *New Zealand Journal of Geology and Geophysics*, 55, 3.

Ben-Menhaem A. (1961). Radiation of seismic surface waves from finite moving sources. Bull. Seism. Soc. Am. 51, 401-453.

Beroza, G. C. & Spudich, P., 1988. Linearized inversion for fault rupture behavior: Application to the 1984 Morgan Hill, California, earthquake, *J. Geophys. Res*., 93, 6275–6296.

Bertero, M. (1989), Linear inverse and ill-posed problems, in *Advances in Electronics and Electron Physics*, Vol. 75, P. W. Hawkes (Editor), Academic, New York, 1–120.

Bertero, M., P. Boccacci, and F. Maggio (1995), Regularization methods in image restoration: an application to HST images, *Int. J. Imaging Systems Tech.* 6**,** 376–386.

Bertero, M., D. Bindi, P. Boccacci, M. Cattaneo, C. Eva, and V. Lanza (1997), Application of the projected Landweber method to the estimation of the source time function in seismology, *Inverse Problems* 13**,** 465–486.

Boschetti, F., Dentith, M. C., & List, R. D., 1996. Inversion of seismic refraction data using genetic algorithms, *Geophysics*, 61, 1715–1727.

Bouchon, M., 1979. Discrete wavenumber representation of elastic wave field in three space dimension, *J. Geophys. Res.*, 84**,** 3609–3614.

Bouchon, M., 1981. A simple method to calculate Green's functions for elastic layered media. *Bull. Seism. Soc. Am.,* 71, 959–971.

Bouchon, M., 2003. A review of the discrete wavenumber method, *Pure Appl. Geophys.*, 160, 445–465.

Bradley, A. B., & Cubrinovski, M., 2011. Near-source Stron Ground Motions Observed in the 22 February 2011 Christchurch Earthquake. *Seism. Res. Lett.*, 82, 853–865.

Cavanaugh, J. E., 1997. Unifying the derivation for the Akaike and corrected Akaike Information Criteria, *Stat. Probabil. Lett.*, 33, 201–208.

Charbonneau, P., 1995. Genetic algorithms in astronomy and astrophysics, *Astrophys. J.*, 101, 309–334.

Chiarabba C., et al. 2009. The 2009 L'Aquila (central Italy) M_w 6.3 earthquake: main shock and aftershocks, *Geophys. Res. Lett.*, 36, L18308.

Cirella, A., Piatanesi, A., Cocco, M., Tinti, E., Scognamiglio, L., Michelini, A., Lomax, A., & Boschi, E., 2009. Rupture history of the 2009 L'Aquila (Italy) eartquake from non-linear joint inversion of strong motion and GPS data, *Geophys.*

Res. Lett., 36, L19304.

Courboulex, F., M. A. Santoyo, J. F. Pacheco, and S. K. Singh (1997a), The 14 September 1995 (*M* 7.3) Copala, Mexico, earthquake: a source study using teleseismic, regional, and local data, *Bull. Seism. Soc. Am.* 87**,** 999–1010.

Delouis, B., Lundgren, P., Salichon, J. & Giardini, D., 2000. Joint inversion of InSAR and teleseismic data for the slip history of the 1999 Izmit (Turkey) earthquake. *Geophys. Res. Lett.*, 27, 3389–3392.

Delouis, B., Giardini, D., Lundgren, P. & Salichon, J., 2002. Joint inversion of InSAR, teleseismic and strong motion data for the spatial and temporal distribution of earthquake slip: Application to the 1999 Izmit mainshock. *Bull. Seism. Soc. Am.*, 92, 278–299.

DeMets, C., Gordon, R. G., Argus, D. F. & Stein, S., 1994. Effect of recent revisions to the geomagnetic time scale on estimates of current plate motion. *Geophys. Res. Lett.* 21, 2,191–2,194.

Elliott, J. R., Nissen, E. K., England, P. C., Jackson, J. A., Lamb, S., Li, Z., Oehlers M., & Parsons, B., 2012. Slip in the 2010-2011 Canterbury earthquakes, New Zealand. *Journal Geophys. Res.*, Vol. 117, B03401.

Emolo, A., 2001. *Modelli di frattura dei terremoti crostali di media e forte magnitudo dall'inversione non lineare di registrazioni a corto-periodo*, Ph.D. Thesis, Universita` "Federico II" di Napoli, Italy.

Emolo, A. & Zollo, A., 2005. Kinematic Source Parameters for the 1989 Loma

Prieta earthquake from the Nonlinear Inversion of Accelerograms. *Bull. Seism. Soc. Am.*, Vol. 95, 981–994.

Emolo A., Cultrera G., Franceschina G., Pacor F., Convertito V., Cocco M. & Zollo A., 2008. Ground motion scenarios for the 1997 Colfiorito, central Italy, earthquake. *Ann. Geophys*., 51, 509-525.

Engdahl, E. & Villaseor, A., 2002. Global seismicity: 1900-1999. *In International Handbook of Earthquake and Engineering Seismology*, *International Geophysics*, pp. 665–690, ed. by P. C. J. William H.K. Lee, H. Kanamori and C. Kisslinger, Academic Press.

Farra, V., & Madariaga, R., 1987. Seismic waveform modelling in heterogeneous media by ray perturbation theory, *J. Geophys. Res.*, 92, 2697–2712.

Farra, V., Bernard, P., & Madariaga, R., 1986. Fast near source evaluation of strong motion for complex source models, *in Earthquake Source Mechanics*, pp. 121–130, ed. Das, S., Boatwright, J. & Scholz, C. H., Geophysical Monograph 37.

Forsyth, P. J., Barrell, D. J. A. & Jongens, R., 2008. Geology of the Christchurch area, *1:250,000 Geological Map 16*, Institue of Geological and Nuclear Sciences, GNS Science, Lower Hutt, New Zealand.

Fry, B., & Gerstenberger, M., 2011. Large apparent stresses from the Canterbury earthquakes of 2010 and 2011. *Seism. Res. Lett.,* 82, 833–838.

Fukuyama, E., and K. Irikura (1986), Rupture process of the 1983 Japan Sea

(Akita-Oki) earthquake using a waveform inversion method, *Bull. Seism. Soc. Am.* 76**,** 1623–1640.

Gledhill, K., Robinson, R., Webb, T., Abercrombie, R., Beavan, J., Cousins, J. & Eberhart-Phillips, D., 2000. The Mw 6.2 Cass, New Zealand, earthquake of 24 November 1995: Reverse faulting in a strike-slip region, *N. Z. J. Geol. Geophys.*, 43, 255–269.

Gledhill, K., Ristau, J., Reyners, M., Fry, B. & Holden, C., 2011. The Darfield (Canterbury, New Zealand) Mw 7.1 Earthquake of September 2010: A Preliminary Seismological Report, *Seism. Res. Lett.*, *82*, 378–386.

Goldberg, D. E., 1989. *Genetic Algorithms in Search, Optimization and Machine Learning*, Addison-Wesley, New York.

Hartzell, S. H. 1978. Earthquake aftershocks as Green's function, *Geophys. Res. Lett.*, 5, 1–4.

Hartzell, S. & Liu, P., 1995, Determination of Earthquake Source Paramenters Using a Hybrid Global Search Algorithm, *Bull. Seism. Soc. Am.*, 85, 516 – 524.

Holden, C., 2011. Kinematic source model of the 22 February 2011 *Mw* 6.2 Christchurch earthquake using strong motion data. *Seism. Res. Lett.,* 82, 783–788.

Ihmlé, P. F. (1996), Frequency-dependent relocation of the 1992 Nicaragua slow earthquake: an empirical Green's function approach, *Geophys. J. Int.* 127**,** 75–85.

Jin, S. & Beydoun, W., 2000. 2D multi-scale non-linear velocity inversion, *Geophys. Prospect.*, 48, 163–180.

Kaiser, A., Holden, C., Beavan, J., Beetham, D., Benites, R., Celentano, A., Collett, D., *et al.* 2011. The February 2011 C hristchurch e arthquake: A preliminary report. Submitted to *New Zealand Journal of Geology and Geophysics*.

Kirkpatrick, S. C., Gelatt, D. & Vecchi M. P., 1983. Optimization by simulated annealing, *Science*, 220, 671-680. 1983.

Koyama J. (1997). *The complex faulting process of earthquakes*. Kluwer Academic, Dordrecht. 194 pp.

Liu, P., Custodio, S. & Archuleta, R. J. 2006, Kinematic inversion of the 2004 M 6.0 Parkfield earthquake including an approximation to site effects, *Bull. Seism. Soc. Am.*, 96, 143-158.

Lomax A., Virieux. J., Volant, P. & Berge, C., 2000. Probabilistic earthquake location in 3D and layered models: introduction of a Metropolis-Gibbs method and comparison with linear locations. *In Advances in Seismic Event Location*, pp. 101-134, ed. Thurber, C.H., Rabinowitz, N., Kluwer, Amsterdam.

Lucca, E., Festa, G., & Emolo, A., 2012. Kinematic conversion of strong motion data using a gaussiana parameterization for the slip: application to the 2008 Iwate-Miyagi, Japan, earthquake. *Bull. Seism. Soc. Am.*, In Press.

Lutter, W. J., Nowack, R. L. & Braile, L. W., 1990. Seismic imaging of upper crustal structure using travel times from the PASSCAL Ouachita experiment, *J.*

Geophys. Res., 95, 4621–4631.

Madariaga R., 1983. Earthquake source theory. A review. In H. Kanamori and E. Boschi (eds). *Earthquake obsertaions, theory and interpretation*. North-Holland, Amsterdam. Pp.1-44.

Maercklin, N., Zollo, A., Orefice, A., Festa, G. & Emolo, A., 2011. The effectiveness of a distant accelerometer array to compute seismic source parameters: the April 2009 L'Aquila earthquake case history, *Bull. Seism. Soc. Am.*, 101, 354-365.

Menke W. (1989). *Geophysical data analysis: discrete inverse theory* . Academic Press, San Diego. 285 pp.

Metropolis, N., Rosenbluth, M. N., Rosenbluth, A. W. , Teller, A. H. & Teller, E. 1977. Equation of state calculations by fast computing machines, *J. Chem. Phys.*, 21, 1087-1092.

Mori, J., and A. Frankel (1990), Source parameters for small events associated with the 1986 North Palm Springs, California, earthquake determined using empirical Green functions, *Bull. Seism. Soc. Am.* 80**,** 278–295.

Mueller, C. S. (1985), Source pulse enhancement by deconvolution of an empirical Green's function, *Geophys. Res. Lett.* 12**,** 33–36.

Nabelek, J., 1984. Determination of earthquake fault parameters from inversion of bodywaves, Ph.D. thesis, pp. 361, MIT, Cambridge, Mass.

Nelder, J. A. & Mead, R. 1965. *Computer J.*, 7,308.

Orefice, A. & Zollo, A. 2010, European Seismological Commission Abstracts, ES5/P31/ID134, 32nd ESC GA Montpellier, France

Palermo, A., Le Heux, M., Bruneau, M., Anagnostopoulou, M., Wotherspoon, L. & Hogan, L., 2010. Preliminary findings on performance of bridges in the 2010 Darfield earthquake, *Bull. New Zeal. Soc. Earthquake Eng.*, *43*, 412–420.

Piatanesi, A., Cirella, A., Spudich, P. & Cocco, M., 2007. A global search inversion for earthquake kinematic rupture history: Application to the 2000 western Tottori, Japan earthquake*, J. Geophys. Res.*, 112, B07314.

Podvin, P. & Lecomte, I., 1991. Finite difference computation of travel times in very contrasted velocity models: a massively parallel approach and its associated tools, *Geophys. J. Int.*, 105, 793–804.

Press W.H., S.A. Teukolsky, W.T. Vetterling and B.P. Flannery (1997). *Numerical recipes in Fortran 77*. Cambridge University Press, Cambridge. 973 pp.

Reasemberg P. & Oppenheimer, D., 1985. FPFIT, FPPLOT and FPPAGE: Fortran computer programs for calculating and displaying earthquake fault-plane solutions, *US Dep. Inter. Geol. Surv*., Open File Rep. 85 739, pp. 109.

Reyners, M. E. & Cowan, H., 1993. The transition from subduction to continental collision: Crustal structure in the north Canterbury region, New Zealand. *Geophys. J. Int.,* 115 (3), 1,124–1,136.

Salichon, J., Delouis, B., Lundgren, P., Giardini, D., Costantini, M. & Rosen, P., 2003. Joint Inversion of broadband teleseismic and interferometric synthetic aperture radar (InSAR) data for the slip history of the Mw=7.7, Nazca ridge (Peru) earthquake of 12 November 1996. *Journal Geophys. Res.*, 108, NO. B2, 2085.

Sambridge, M. & Drijkoningen, G., 1992. Genetic algorithms in seismic waveform inversion, *Geophys. J. Int.*, 109, 323–342.

Sambridge, M. & Mosegaard K. 2002. Monte Crlo Methods In geophysical Onverse problems. *Reviews of Geophisics*, 1009, doi:10.1029/2000RG000089.

Savage, J. C., 1980. Dislocations in seismology, *in Dislocations in Solids*, ed. by F. R. N. Navarro, North-Holland, New York.

Sibson, R., Ghisetti, F. & Ristau, J., 2011, Stress Control of an Evolving Strike-Slip Fault Sustem during the 2010-2011 Canterbury, New Zealand, Earthquake sequence. *Seismol. Res. Lett*., 82, 824-832.

Sibson, R. H., Ghisetti, F. C. & Crookbain, R. A., 2012. Andersonian wrench faulting in a regional stress field during the 2012-2011 Canterbury, New Zealand, earthquake sequence, *Geological Society, London, Special Publications 2012*, 367, 7-18.

Sutherland, R., Berryman, K. & Norris, R., 2006. Quaternary slip rate and geomorphology of the Alpine fault: Implications for kinematics and seismic hazard in southwest New Zealand. *Bull. Geol Soc Am*, 118, 464–474.

Timm, C., Hoernle, K., Bogaard, P., Bindeman, I. & Weaver, S., 2009. Geochemical evolution of intraplate volcanism at Banks Peninsula, New Zealand:

Interaction between asthenospheric and lithospheric melts. *J. Petrol.*, 50 (6), 989–1,023.

Vallée, M., 2004. Stabilizing the Empirical Green Function Analysis: Development of the Projected Landweber Method. *Bull. Seism. Soc. Am.*, 94, 394-409.

Velasco, A. A., C. J. Ammon, and T. Lay (1994), Empirical Green function deconvolution of broadband surface waves: rupture directivity of the 1992 Landers, California (M_W=7.3), *Bull. Seism. Soc. Am.* 84**,** 735–750.

Wallace, L., Beavan, J., McCaffrey, R., Berryman, K. R. & Denys, P., 2007. Balancing the plate motion budget in the South Island, New Zealand, using GPS, geological and seismological data. *Geophys. J. Int.* 168 (1); doi:10.1111/j.1365-246X.2006.03183.x.

Zhan, Z., Jin, B., Wei, S. & Graves, W., 2011. Coulom Stress Change Sensitivity due to Variability in Mainshock source Models and receiving Fault Parameters: A Case study of the 2010-2011 Christchurch, New Zealand Earthquake. *Seismol. Res. Lett*., 82, 800-814.